



**HAL**  
open science

# Confined growth of carbon nanotubes and silicon nanowires in lateral porous alumina templates

Gowtham Manoharan

► **To cite this version:**

Gowtham Manoharan. Confined growth of carbon nanotubes and silicon nanowires in lateral porous alumina templates. Chemical Sciences. Ecole Polytechnique X, 2009. English. NNT: . pastel-00005283

**HAL Id: pastel-00005283**

**<https://pastel.hal.science/pastel-00005283>**

Submitted on 4 Sep 2009

**HAL** is a multi-disciplinary open access archive for the deposit and dissemination of scientific research documents, whether they are published or not. The documents may come from teaching and research institutions in France or abroad, or from public or private research centers.

L'archive ouverte pluridisciplinaire **HAL**, est destinée au dépôt et à la diffusion de documents scientifiques de niveau recherche, publiés ou non, émanant des établissements d'enseignement et de recherche français ou étrangers, des laboratoires publics ou privés.



THÈSE

Présentée pour obtenir le grade de  
DOCTEUR DE L'ÉCOLE POLYTECHNIQUE

Spécialité: Physique

Gowtham MANOHARAN

**Confined growth of carbon nanotubes and silicon nanowires in  
lateral porous alumina templates**

Croissance confinée de nanotubes de carbone et nanofils de silicium  
dans des membranes latérales d'alumine poreuse

Soutenue le 26/01/2009 devant le jury constitué de:

- A. LOISEAU      **Rapporteur**  
B. MILNE        **Rapporteur**  
J - P. BOURGOIN **President, Examineur**  
P. LEGAGNEUX **Examineur**  
M. CHATELET    **Directeur de Thèse**  
D. PRIBAT       **Co-Directeur**

LABORATOIRE DE PHYSIQUE DES INTERFACES ET COUCHES MINCES, CNRS UMR 7647  
ÉCOLE POLYTECHNIQUE



## ACKNOWLEDGEMENTS

- I would like to first thank **Didier PRIBAT** for his guidance and support during the PhD. He provided me with the intellectual freedom of work on several stimulating research projects. His acuteness of understanding experimental results inspires me.

- I thank **Marc CHÂTELET**, the director of my PhD, who advised me on regular basis and took care of the advancement of the PhD.

- Special thanks to **Costel-Sorin COJOCARU**, for his valuable help, his regular advice was essential for me to improve and to achieve the results. His know-how made me save time and he encouraged me to progress steadily.

- I am grateful to my thesis jury members, especially to the two reporters **Bill MILNE** and **Annick LOISEAU**, for their valuable suggestions and for reviewing my dissertation.

- I am indebted to my colleagues **Laurent EUDE**, **Bernd MARQUARDT**, **Anh Quoc LEQUANG**, **Hee-jin JEONG**, **Arnaud-Julien GUILLEY**, **Laurent BARATON**, **Anirban DHAR**, **Amael CAILLARD** for their valuable helps through these three years.

- I thank **Garry ROSE KITCHNER** and **Éléonor CARISTAN** for installing the instruments and helping me to solve technical problems during the course of my work.

- I thank **Laurence CORBEL** and **Chantal GENESTE**, for the administrative help and the good environment they made in the laboratory to continue the work without any delay.

- Special acknowledgment to **Pierre LEGAGNEUX** (Thales research and technology) and **Pavel BULKIN** (LPICM) and **Travis WADE** (LSI) for the various help and discussions

-I thank **Véronique MATHET**, **David BOUVILLE**, **Sylvain DAVID**, **Gwénaëlle JULIÉ**, **José PALOMO**, **Cédric VILLEBASSE**, **Abdelhanin AASSIME** from IEF-CTU in university Paris 11, for their valuable help in training and by discussion for the technological process involved in this work.

- I thank **Stephane XAVIER**, **Shailendra BANSROPUN**, **Shaïma Enouz VÉDRENNE**, **Jean-Luc MAURICE**, **Christian COLLET** from the Thales research and technology for their help in using some techniques and characterization during this work.

-I thank all the members of the Laboratory **LPICM** as well as the members of the **NANOCARB** team in Thales research and technology for the direct and indirect help these three years

-Last but not the least I thank my **parents** and my better half **Manohari** for their moral support and encouragement.



# TABLE OF CONTENTS

Acknowledgements.....	1
1: Introduction.....	11
1.1: Background.....	11
1.2: Carbon Nanotubes.....	13
Physical properties.....	15
1.2.1: Synthesis.....	18
1.2.2: Progress and applications.....	19
1.3: Silicon nanowire.....	19
1.3.1: Growth of NWs.....	20
1.3.2: Progress and applications.....	21
1.4: Organization of CNTs and NWs.....	21
1.4.1: CNTs.....	21
1.4.2: NWs.....	26
1.5: Device.....	29
1.6: Conclusion.....	30
2: Porous Anodic Alumina templates.....	35
2.1: Anodization.....	35
2.1.1. Electrochemistry Of Anodic Alumina.....	38
2.1.2. Potential and current transients.....	38
2.1.3. The mechanism of stress generation during the growth of Porous anodic alumina oxide films.....	39
2.1.4. Pore Formation and growth mechanisms.....	43
2.1.5. General principle.....	46
2.1.6. Pore ordering mechanisms.....	48
2.1.7. Model for polycrystallinity.....	49
2.1.8. Effect of the electrochemical conditions on the physical and chemical properties.....	51
2.1.9. Trend in porous anodic alumina structures.....	52
2.2. Experiments.....	53
2.2.1. Results and discussion.....	55
2.3 .Conclusion.....	57
3: Lateral porous anodic alumina templates.....	61

3.1. Introduction.....	61
3.2. Experimental details.....	62
3.3. Results and discussion .....	64
3.3.1. Modified electropolishing:.....	64
3.3.2: Pore diameter control:.....	66
3.3.3: Pore Depth .....	71
3.4. Spatially constrained anodization .....	74
3.4.1. Mechanism of the lateral pore growth .....	77
3.4.2. Pore density Control .....	79
3.5. Conclusion: .....	81
4: CNT and SiNW GROWTH inside the lateral porous alumina templates.....	85
4.1: Introduction.....	85
4.2: Catalyst for the CNT growth.....	87
4.2.1: CATALYST particle size .....	87
4.2.2: Chemical composition of the catalyst.....	88
4.3: CATALYSTS for SiNW growth .....	89
4.4: PAA templates for nanomaterial fabrication .....	90
4.5: Growth of CNT and SiNW inside PAA template.....	93
4.5.1: Mechanism of CNT & NW growth inside PAA template .....	93
4.6: CNT/SiNW growth inside lateral PAA template.....	96
4.6.1: Growth technique.....	96
4.6.2: SiNW .....	98
4.6.3: CNT .....	102
4.6.1. HRTEM characterization .....	106
4.7: Conclusion .....	108
5: Conclusion and outlook .....	111
Out look .....	112
<b>Annex I: Technological steps for THE LATERAL CNT/ SiNW-FET FABRICATION.....</b>	<b>117</b>
1. Thermal oxide wafer .....	117
2. Aluminum deposition.....	118
3.Photolithography –I .....	118
4.Encapsulation.....	120

5. Photolithography –II .....	121
6. Reactive ion etching .....	122
7. Electrochemical process .....	123
Electrodeposition .....	123
8. CNT growth .....	124
9. Annealing (future work) .....	124
10. S/D and Gate electrode deposition (future work) .....	124
Conclusion .....	125
Annex II: Alternate technology adaptation .....	129
1. Dielectrophoresis of protein .....	129
Experiments .....	130
List of Publications .....	133
References .....	135



# **Chapter 1: Introduction**



# 1: INTRODUCTION

## 1.1: BACKGROUND

*Necessity is the mother of invention<sup>1</sup>*

The main player of the technological revolution is the electronics industry and it is just the direct output of the people necessity. In this modern life people use 250 electronic gadgets in their daily life<sup>2</sup>. Integrated circuits (ICs) are the heart of these electronics devices. The birth of the IC let people use electronic devices with reduced size and with increased speed. The basic components found in these ICs are active semiconductor devices and passive components. Among these, transistors are found to be important building blocks. The number of transistors in an IC is directly proportional to the performance of the chip. Day by day with the people needs, industry showed the pace of improvement in its electronic products. Most of these trends have resulted principally from the industry ability to exponentially decrease the minimum feature sizes used to fabricate ICs. And the most frequently cited trend is in integration level, which is usually expressed as Moore's law<sup>3</sup> (ie) the number of components per chip doubles roughly every 24 months. The most significant trend is the decreasing cost-per-function, which has led to significant improvements in the economic productivity and overall quality of life through proliferation of computers, communications and other industrial consumer electronics<sup>4</sup>.

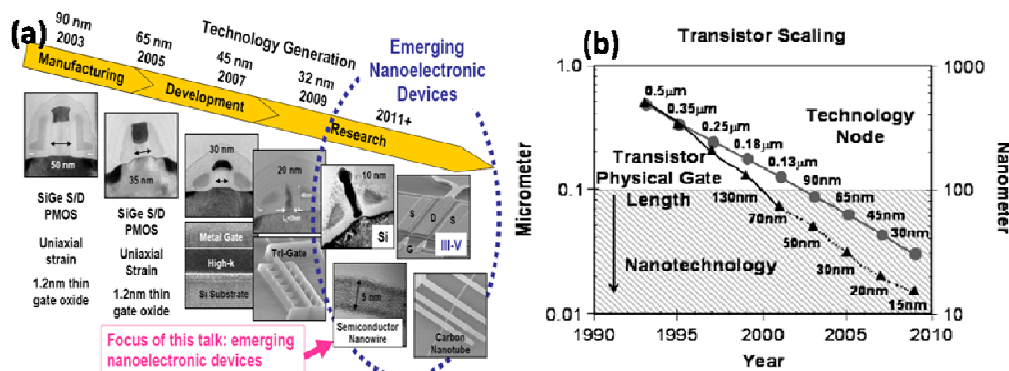


**Figure 1-1:** scaling of transistor size (physical gate length) with technology node to sustain Moore's Law. Nodes with feature size less than 100nm can be referred to as nanotechnology. By 2011, the gate length is expected to be at or below 10nm. Transistor scaling will be enabled by integration of emerging nanotechnology options on to the Si platform. (Robert Chau – intel)

The sustaining of Moore's law requires transistor scaling, as illustrated in the Figure 1-1. The physical gate length ( $L_g$ ) of Si transistors used in the current 90-nm generation node is ~50nm. It is projected that the size of the transistors will reach ~10 nm in 2011. Through technology innovations, such as strained –

Si channels<sup>5,6</sup>, metal-gate/high- $\kappa$  stacks<sup>7</sup> and the nonplanar fully depleted Tri-gate complementary metal oxide semiconductor (CMOS) transistor architecture<sup>8</sup>, Moore's Law will continue at least through early next decade. By combining silicon innovations with other novel nanotechnologies on the same silicon platform, we expect Moore's Law to extend well into the next decade. Recently, there has been tremendous progress made and excitement generated in the research of nanotechnology for future nanoelectronics applications. Among the various nano objects Carbon nanotubes (CNTs) and Silicon nanowires (SiNW) are the best candidates for the nanoelectronics application. To gauge the progress of nanotechnology research for high performance and low power logic applications, it is important that these new devices such as carbon nanotube field effect transistors (CNT-FET)<sup>9,10,11</sup> and Silicon nanowires FETs (SiNW-FETs)<sup>12,13,14</sup> be benchmarked against the best Si MOSFET data using a set of appropriate device metrics<sup>15</sup>. The benchmarking results show that while these novel devices hold promise and opportunities for future logic transistor applications, their performance and electrostatics require further improvement and their scalability still needs to be demonstrated. For example, one key area to focus on in CNTs and NWs is to replace the metal source-drain junctions with conventional P-N junctions in order to eliminate ambipolar conduction, improve sub threshold slope, and further enhance the effective channel mobility.

**Table 1-1: comparison of different type of transistor characteristics**

Type of transistors	CNTFET	Si NW FET	Si MOSFET
Gate length (nm)	260	50	15
Gate oxide Thickness (nm)	15	1.5	1.4
$I_{ON}$ ( $\mu\text{A}/\mu\text{m}$ )	2100	2000-5600	265
$I_{OFF}$ (nA/ $\mu\text{m}$ )	150	4-45	~ 500
Subthreshold slope (mV/dec)	130	60	~100
Transconductance ( $\mu\text{S}/\mu\text{m}$ )	2321	2700-7500	975

Table 1-1 provides a comparison of the transistor characteristics of CNTs and SiNWs with a standard Si MOSFET. In case of the bulk Silicon, the process is well optimized for many decades. But for these new

nano objects there are no standard processes until now to integrate with the CMOS technology. In the present work we try to address the various ways to organize these CNTs and SiNWs, which are available in the literature. We have also introduced a novel way to organize them, by combining various known techniques available in the industry.

We propose a technological solution to organize CNTs and SiNWs in the CMOS scale for the future nanoelectronics devices.

### 1.2: CARBON NANOTUBES

Carbon has four electrons in its outer valence shell; the ground state configuration is  $2s^2 2p^2$ . Diamond and graphite are considered as the two natural crystalline forms of pure carbon. In diamond, carbon atoms exhibit  $sp^3$  hybridization, in which four bonds are directed toward the corners of a regular tetrahedron. The resulting three-dimensional network (diamond) is extremely rigid, which is one reason for its hardness. The bond length between  $sp^3$  carbons (e.g diamond) is 1.56 Å. In graphite,  $sp^2$  hybridization occurs, in which each atom is connected evenly to three carbons ( $120^\circ$ ) in the  $xy$  plane, and a weak  $\pi$  bond is present in the  $z$  axis. The C-C  $sp^2$  bond length is 1.42 Å. The  $sp^2$  set forms the hexagonal (honey comb) lattice typical of a sheet of graphite. The  $p_z$  orbital is responsible for a weak bond, a Van der Waals bond. The spacing between the carbon layers is 3.35 Å. The free electrons in the  $p_z$  orbital move within this cloud and are no longer local to a single carbon atom (delocalized). This phenomenon explains why graphite can conduct electricity. Diamond, on the contrary, behaves as an insulator because all electrons are localized in the bonds within the  $sp^3$  framework.

CNTs are considered as a new form of pure carbon and they can be visualized as rolled hexagonal carbon networks that are capped by pentagonal carbon rings. There are two types of carbon tubes: single-walled (SWCNTs) and multi-walled (MWCNTs).

The first mention of the possibility of forming carbon filaments from the thermal decomposition of gaseous hydrocarbon (methane) was reported in 1889<sup>16</sup> i.e., more than a century ago in a patent that proposed the use of such filaments in the light bulbs, that had been presented by Edison at the Paris Universal Exposition the same year. Other early reports consist of two papers presented in the French Academy of Sciences<sup>17,18</sup>. However, such papers can hardly be considered as the first evidence for the growth of CNTs since it was not possible to have enough resolution to view them with optical microscopes. With the subsequent invention of the transmission electron microscope (TEM), the first

commercial versions of which were produced by Siemens in 1939, significant progress was made in the fifties regarding the morphology and inner texture of carbon filaments. The first TEM evidence for the tubular nature of some nano-sized carbon filaments is mentioned in 1952<sup>19</sup>, in the Journal of Physical Chemistry of Russia<sup>20</sup>.

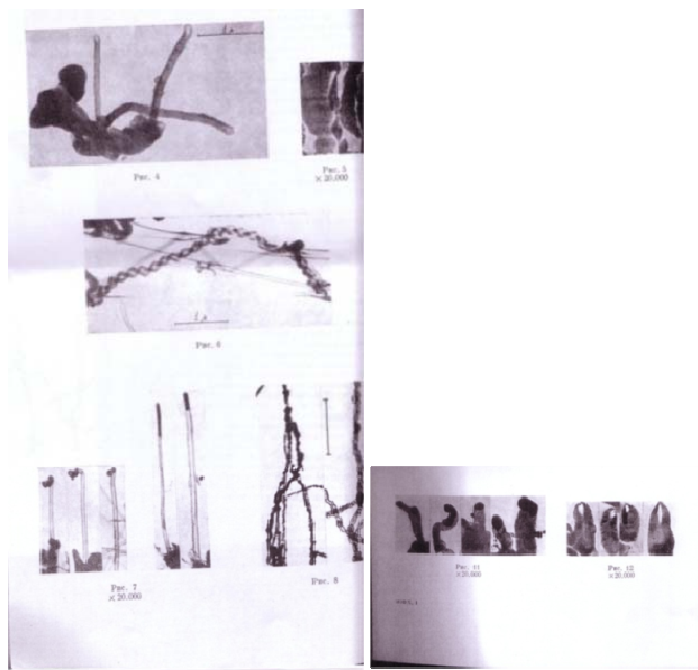


**Figure 1-2:** Examples of first TEM images of carbon nanotubes published in 1952

The first series of high-resolution transmission electron microscopy (HRTEM) images of CNTs were obtained by Endo in the mid-1970s<sup>21</sup>. Endo wanted to analyze the internal structure of carbon fibers produced by pyrolysis of benzene and ferrocene at 1000°C, and elucidate their growth mechanism in order to control the bulk production of fibers. Because Endo needed these specimens for HRTEM studies, he varied the experimental production conditions so that thin fibers (<10nm) were produced. He observed that tubular graphite of nanometer scale could be produced using this thermolytic process, and imaged the first ever-observed SWCNTs and MWCNTs. Unfortunately; this report did not cause a great impact because researchers were more interested in micron-sized carbon fibers, at that time.

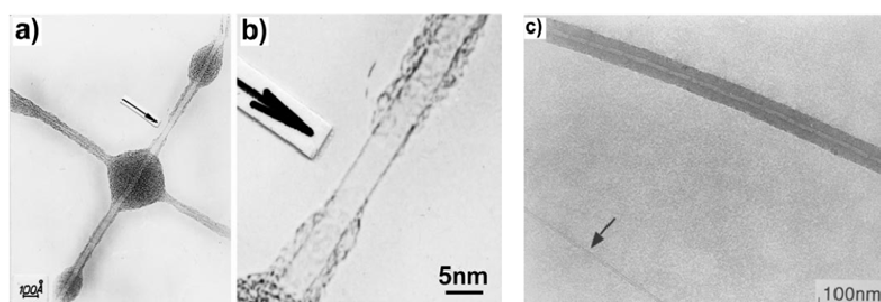


**Figure 1-3:** (a) HRTEM image of two crossing SWNTs coated with amorphous carbon, produced using catalytic processes ; (b) Higher magnification of (a) showing that the structure consist of an individual graphene cylinder in projection. The diameter of the tube is  $\sim 4$  nm. This may be the first image of a SWNT ever taken; (c) HRTEM image showing a MWNT upper region together with a SWNT indicated by an arrow (image obtained in 1975 by M. Endo)

Fifteen years later, Iijima, using HRTEM and electron diffraction, reported the existence of helical carbon microtubules (now called nanotubes) consisting of nested graphene tubules<sup>22</sup>. This material was generated in an arc-discharge fullerene reactor. These concentric tubules exhibited interlayer spacings of  $\sim 3.4$  Å, a value slightly greater than that of graphite planes (3.35 Å). Iijima associated this spacing difference to a combination of graphene sheet curvature and weaker Van der Waals forces acting between the successive cylinders.

### PHYSICAL PROPERTIES

It is possible to construct a  $sp^2$ -hybridized carbon tubule theoretically by rolling up a hexagonal graphene sheet and thus lead to non-chiral or chiral arrangements. In the non-chiral geometries, the honeycomb lattices, located at the top and bottom of the tube, are always parallel to the tube axis (these configurations are known as armchair and zig-zag). In the armchair structure, two C–C bonds on opposite sides of each hexagon are perpendicular to the tube axis, whereas in the zig-zag arrangement, these bonds are parallel to the tube axis (Figure 1-4a, b). All other conformations in which the C–C bonds lie at an angle to the tube axis are known as chiral or helical structures (Figure 1-4c).

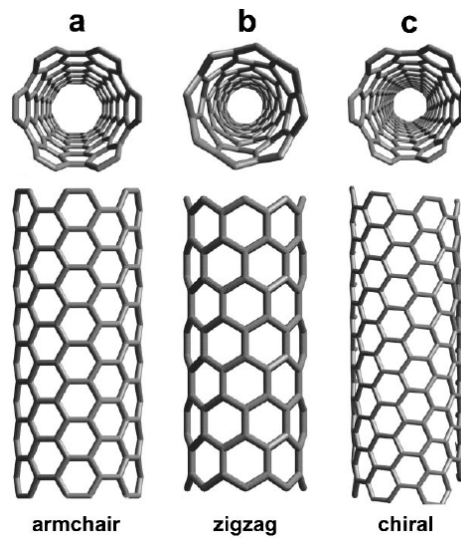


**Figure 1-4:** Molecular models of SWNTs exhibiting different chiralities: (a) armchair configuration, (b) zig-zag arrangement, and (c) chiral conformation

A SWNT can be described as a single layer of a graphite crystal rolled up into a seamless cylinder, one atom thick, usually with a small number (perhaps 10–40) of carbon atoms along the circumference and a long length (microns) along the cylinder axis. A CNT is specified by the chiral vector  $\mathbf{C}_h$ ,

$$\mathbf{C}_h = n\mathbf{a}_1 + m\mathbf{a}_2 \equiv (n, m)$$

which is often described by the pair of indices  $(n, m)$  that denote the number of unit vectors  $n\mathbf{a}_1$  and  $m\mathbf{a}_2$  in the hexagonal honeycomb lattice contained in the vector  $\mathbf{C}_h$ . As shown in Figure 1-5, the chiral vector  $\mathbf{C}_h$  makes an angle  $\theta$ , the chiral angle, with the so-called zigzag or  $\mathbf{a}_1$  direction. The vector  $\mathbf{C}_h$  connects two crystallographically equivalent sites  $O$  and  $A$  on a two-dimensional graphene sheet where a carbon atom is located at each vertex of the honeycomb structure. The axis of the zigzag nanotube corresponds to  $\theta = 0^\circ$ , whereas the so-called armchair nanotube axis corresponds to  $\theta = 30^\circ$  and the nanotube axis for so-called chiral nanotubes corresponds to  $0 < \theta < 30^\circ$ . The seamless cylinder joint of the nanotube is made by joining the line  $AB'$  to the parallel line  $OB$  in Figure 1-5.

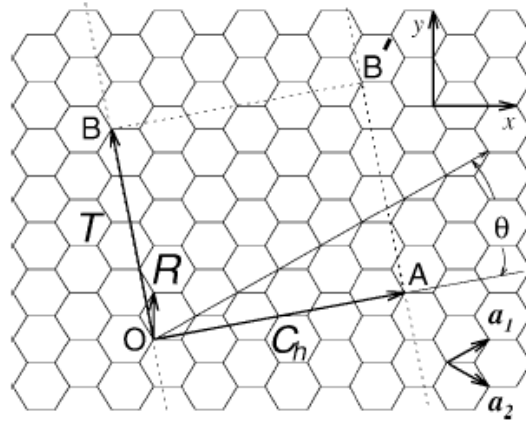


**Figure 1-5:** The unrolled honeycomb lattice of a nanotube. When we connect sites  $O$  and  $A$ , and sites  $B$  and  $B'$ , a nanotube can be constructed. The vectors  $OA$  and  $OB$  define the chiral vector  $C_h$  and the translational vector  $T$  of the nanotube, respectively. The rectangle  $OAB'B$  defines the unit cell for the nanotube. The figure is constructed for an  $(n,m) = (4,2)$  nanotube

The nanotube diameter  $d_t$  can be written in terms of the integers  $(n,m)$  as

$$d = C_h / \pi = a \sqrt{m^2 + mn + n^2} / \pi$$

where  $a = 1.42 \times \sqrt{3} \text{ \AA}$  corresponds to the lattice constant in the graphite sheet.  $C_h$  is the length of the chiral vector  $C_h$ , and the chiral angle  $\theta$  is given by

$$\theta = \tan^{-1} [\sqrt{3}m / (m + 2n)]$$

Thus, a nanotube can be specified by either its  $(n,m)$  indices or equivalently by  $d$  and  $\theta$ . Next, the unit cell is defined by  $OBB'A$  of the one-dimensional nanotube in terms of the unit cell of the two-dimensional honeycomb lattice defined by the vectors  $\mathbf{a}_1$  and  $\mathbf{a}_2$  (Figure 1-5).

Theoretical studies on the electronic properties of carbon tubules indicate that all armchair tubules are metallic, as well as zigzag cylinders exhibiting values of  $n, m$  multiples of three<sup>23,24</sup>

It is amazing that SWNTs can be either metallic or semiconducting depending on the choice of  $(n, m)$ ; although there is no difference in the chemical bonding between the carbon atoms within the tubules and no doping or impurities are present. The unique electronic properties of CNTs are caused by the quantum confinement of electrons normal to the nanotube axis.

### 1.2.1: SYNTHESIS

CNTs can be produced using a wide variety of process such as arc-discharge, pyrolysis of hydrocarbons over metal particles, laser vaporization of graphite targets.

**Table 1-2: Different synthesis methods for CNTs**

<b>Method</b>	<b>Arc-discharge</b>	<b>Laser-ablation</b>	<b>CVD</b>
<b>Pioneer</b>	Iijima (1991)	Guo et al. (1995)	Yacaman et al. (1993)
<b>How</b>	CNT growth on graphite electrodes during direct current arc-discharge evaporation of carbon in presence of an inert gas	Vaporization of a mixture of carbon (graphite) and transition metals located on a target to form CNTs	Acetylene decomposition over graphite-supported iron particles at 700°C
<b>Yields</b>	<75 %	<75 %	>75%
<b>SWCNT or MWCNT</b>	Both	Only SWCNTs	Both
<b>Advantage</b>	Simple, inexpensive	Relatively high purity CNTs, room temperature synthesis option with continuous laser	Simple, inexpensive, low temperature, high purity and high yields, aligned growth is possible, fluidized bed technique for large-scale
<b>Disadvantage</b>	Purification of crude product is required, method cannot be scaled up, must have high temperature	Crude product purification required, not economically advantageous method for production	CNTs usually are MWCNTs, parameters must closely be watched to obtain SWCNTs

All the above methods have advantages and disadvantages, but the chemical vapour deposition (CVD) method of synthesizing CNTs has the greatest potential of all the methods discussed. Because CNTs grown by CVD have high yield, high purity, well aligned and even large scale synthesis is possible. By using the CVD method, different nanotubes (SWCNTs or MWCNTs) can be produced on different substrates. It has been found that the substrate/CNT interface interactions govern the alignment and type of CNT produced.

### 1.2.2: PROGRESS AND APPLICATIONS

In the early 1990s, two research groups calculated the electronic properties of individual SWCNTs for the first time<sup>25, 26</sup>. They predicted that SWCNTs might be metallic or semiconducting, depending upon their chirality (the way the hexagons are arranged along the tubule axis) and diameter. By the end of that decade, these particular predictions were confirmed experimentally<sup>27, 28</sup>. Other experimental groups conducted transport measurements on nanotube sample<sup>29</sup>, individual multilayered tubes<sup>30</sup> and ropes of single-walled tubules<sup>31</sup>. These reports revealed that the conducting properties of the tubes are extremely sensitive to the degree of graphitization, chirality, and diameter. Subsequently, Young's Moduli measurements demonstrate that multilayered CNTs are mechanically much stronger than conventional carbon fibers and are extraordinarily flexible when subjected to large strain.

An exponential growth of nanotube research has led to the development of various emerging technologies. Some examples of applications include the use of nanotubes as (a) FETs<sup>40</sup>; (b) intratube p-n junctions<sup>32,33</sup>; (c) Inverters<sup>34,35,36</sup>; (d) gas storage<sup>37</sup>; (e) STM probes<sup>38</sup> and field emission sources<sup>39</sup> (f) microwave devices<sup>40</sup>; (g) high-power electrochemical capacitors<sup>41</sup>; (h) electronic nanoswitches<sup>42</sup>; (i) chemical sensors<sup>43</sup>; (j) magnetic data storage devices (e.g., Fe filled nanotubes)<sup>44</sup>; (k) nanocomposites<sup>45</sup>; (l) the production of nano rods (e.g.; TiC, NbC, Fe<sub>3</sub>C, SiC and BC<sub>x</sub>) using CNTs as reacting templates<sup>46</sup>. However, in order to employ CNTs on a commercial basis, it is necessary to control their growth, length, diameter and crystallinity at accessible costs.

### 1.3: SILICON NANOWIRE

Another class of 1d nanostructures that has received considerable attention other than CNT is the SiNW. In contrast to CNTs whose electronic properties are largely determined by the chirality of the tubes, NWs offer several unique advantages. First, NW devices can be assembled in a rational and predictable manner because the size and electronic properties of the NWs can be precisely controlled during synthesis. Moreover, reliable methods exist for their parallel assembly<sup>47</sup>. The growth direction and side surfaces of nanowires can be precisely controlled during synthesis to produce the desired properties. Second it is possible to combine distinct NW building blocks in ways which are not possible in conventional electronics and to achieve new function and correspondingly could lead to unexpected devices. Finally, the structure of NWs can be used for integrating materials of different chemical composition and crystal structure into an entity that exhibits multi-functionality. Therefore, NWs open up a new paradigm in nanotechnology well beyond that possible with a single-composition building block.

### 1.3.1: GROWTH OF NWS

Semiconductor NWs are generally synthesized by employing metal nanocluster as catalyst via vapour-liquid-solid (VLS) process<sup>48</sup> (Figure 1-6). This mechanism was first proposed for the growth of single crystal silicon whiskers, 100 nm to hundreds of microns in diameter (Wagner and Ellis, 1964). The proposed growth mechanism involves the absorption of source material from the gas phase into a liquid droplet of catalyst. Upon super-saturation of the liquid alloy, a nucleation event generates a solid precipitate of the source material. This seed serves as a preferred site for further deposition of material at the interface of the liquid droplet, promoting the elongation of the seed into a nanowire or a whisker, and suppressing further nucleation events on the same catalyst. Since the liquid droplet catalyzes the incorporation of material from the gas source to the growing crystal, the deposit grows anisotropically as a whisker whose diameter is dictated by the diameter of the liquid alloy droplet. The nanowires thus obtained are of high purity, except for the end containing the solidified catalyst as an alloy particle. However recently, High-Angle Annular Dark-Field Scanning Transmission Electron Microscopy (HAADF-STEM) studies revealed that Au atoms in SiNW<sup>49</sup>.

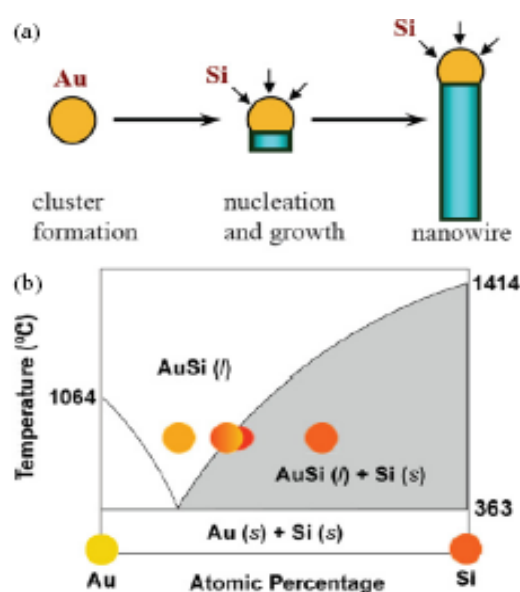


**Figure 1-6:** Schematic of VLS growth of Si nanowires (SiNWs). (a) A liquid alloy droplet AuSi is first formed above the eutectic temperature (363°C) of Au and Si. The continuous feeding of Si in the vapour phase into the liquid alloy causes oversaturation of the liquid alloy, resulting in nucleation and directional nanowire growth. (b) Binary phase diagram for Au and Si illustrating the thermodynamics of VLS growth

The gaseous semiconductor reactants can be generated through decomposition of precursors in a CVD process or through momentum and energy transfer methods such as pulsed laser ablation<sup>50</sup> or molecular beam epitaxy (MBE)<sup>51</sup> from solid targets. So far, CVD has been the most popular technique. In CVD-VLS growth, the metal nanocluster serves as a catalyst at which site the gaseous precursor decompose, providing the gaseous semiconductor reactants. In the case of SiNW growth (Figure 1-6), silane (SiH<sub>4</sub>) and gold (Au) nano particles are normally used as the precursor and catalyst, respectively. Besides group IV materials, compound III-V and II-VI NWs have also been produced with the VLS method, in which pseudo binary phase diagrams for the catalyst and compound semiconductor of interest are employed. In the compound semiconductors case, metal-organic chemical vapour deposition (MOCVD)<sup>52</sup> or pulsed laser ablation<sup>53</sup> are typically used to provide the reactants.

### 1.3.2: PROGRESS AND APPLICATIONS

SiNWs and their heterostructures have been actively studied for various applications such as high-performance electronic devices<sup>54,55,56</sup>, biochemical sensors<sup>57,58</sup>, and optical devices<sup>59,60,61,62</sup>. Although various methods have been reported for the fabrication of SiNW-based devices, most of the previous methods can generate only devices by unconventional method, which has been holding back their industrial applications.

## 1.4: ORGANIZATION OF CNTs AND NWS

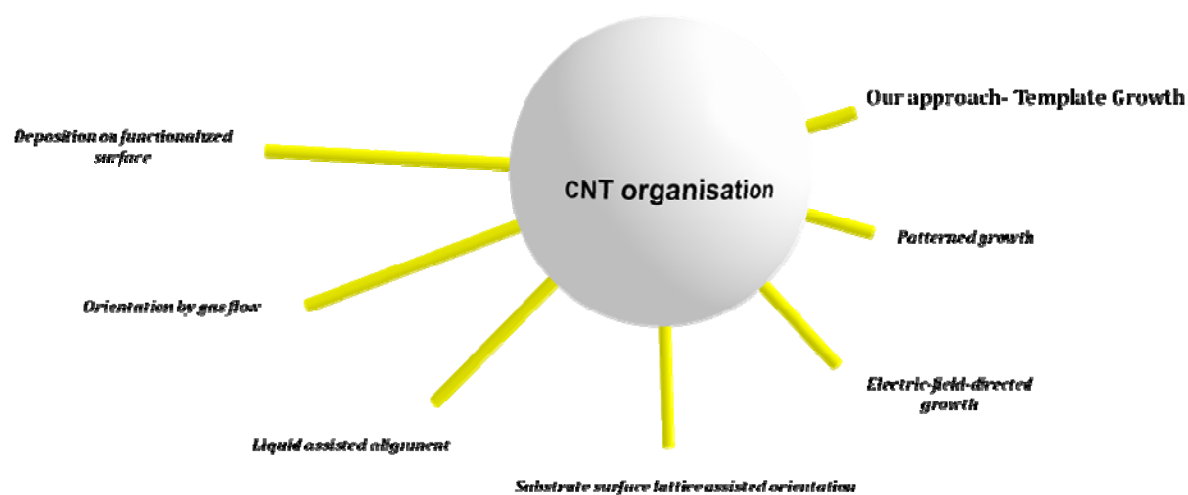
Recently, there has been a large amount of interest in new functional devices based on CNTs and various types of NWs. A lack of large-scale integration techniques has, however, been a major obstacle to the integration of those new devices into practical applications.

Previous methods for device integration include some methods relying on external forces to align NTs or NWs, and it is an extremely time-consuming task to integrate millions of NTs and NW-based devices with arbitrary orientations. Reactive linker molecules have also been used for the directed assembly of NTs and NWs, but it is known that the reactive chemical groups used for NT and NW adhesion could alter the electrical properties of the NTs and NWs in an unexpected manner. Here in the following section we discussed the different techniques to organize CNTs and NWs; available in the literature.

### 1.4.1: CNTs

Different techniques available in the literature are given in the chart 1, where the length of the yellow line represents the magnitude of difficulty in process as well as the degree of compatibility with the industry.

Chart: 1 CNT organization methods



#### 1.4.1a: Patterned growth

---

Kroto and co-workers<sup>63</sup> reported, CNT growth on a silica substrate prepatterned with a cobalt catalyst by laser etching. In this context, Dai and co-workers<sup>64</sup> have demonstrated the ability to grow SWNT wires between controlled surface sites by catalyst patterning, leading to a variety of interconnecting SWNT architectures, which includes a suspended SWNT<sup>65</sup> power line and a square of suspended SWNT bridges. In a closely related to the work, Ajayan and coworkers<sup>66</sup> attempted to synthesize MWNTs on the surface of magnesium oxide cubes in order to enhance the possibility of creating networks over which nanotubes can be distributed.

#### 1.4.1b: Controlled deposition of carbon nanotubes on a patterned substrate

---

The Roth group introduced a approach of patterning the nanotubes on the amino-silanized electrodes; first they succeeded in growing MWCNTs<sup>67</sup> and later SWCNTs<sup>68</sup>. They describe the controlled deposition of individual nanotubes onto a silicon wafer. The approach takes advantage of chemical modifications on the surfaces of SiO<sub>2</sub> and the electrodes.

In July 2008, a joint group between Stanford University and Samsung reported<sup>69</sup> a novel method to self sort and align nanotube networks in a single step process. By using spin-assisted alignment, the density of the SWNTs is tuned by different surfaces that effectively vary the degree of interaction with surface functionalities in the device channel. This leads to a self-sorted SWNT network in which nanotube chirality separation and simultaneous control of density and alignment occur in one step during device fabrication. Micro-Raman experiments corroborate device results as a function of surface chemistry, indicating enrichment of the specific SWNT electronic type absorbed onto the modified dielectric.

Even though the technique they used was very simple, it is not compatible with industrial processes and also reproducibility of this method is questionable.

### *1.4.1c: Electric-field-directed growth of aligned single-walled carbon nanotubes*

---

Joselevich and Lieber<sup>70</sup> have demonstrated a new approach to the vectorial growth of SWNT arrays by patterning the catalyst nanoparticles and applying a local electric field parallel to the substrate. The Dai group<sup>71</sup> also demonstrated electric-field-directed growth of SWCNTs by CVD. The field-alignment effect originates from the high polarizability of SWCNTs. Large induced dipole moments lead to large aligning torques and forces on the nanotube, and prevents randomization of nanotube orientation by thermal fluctuations and gas flows. The results opened up possibilities in directed growth of ordered molecular-wire architectures and networks on surfaces. To fully utilize the electric-field alignment effect, it is important to keep SWNTs from Van der Waals interactions with nearby surfaces during growth.

### *1.4.1d: CNT growth by gas flow*

---

The Smalley group<sup>72</sup> proposed a "kite-mechanism" with the catalyst nanoparticle having a long nanotube tail floating in the gas flow. The kite-mechanism contains several important stages. The most important stage is the initial stage of the growth. In "fast-heating" CVD, the samples were heated to the reaction temperature (900°C for most cases) over a very short period. As the result of fast heating, the solid sample and the surrounding gas were heated at different speeds and had different temperatures during the heating. A convection flow was formed due to the temperature difference; this could lift some of the nanotubes up with the catalysts on their tips. The nanotubes grew up, leaving the surface region where the flow velocity of the feeding gas was slow. Then the horizontal laminar flow of the feeding gas above the substrate surface carried the nanotubes while they were growing and aligned the nanotubes along the direction of gas flow. During growth, the active ends of the nanotubes were always floating while the

sections close to the original sites where the catalyst was deposited might form Van der Waals contacts with the substrate. The nanotubes kept growing until they lay down onto the surface or until termination of the carbon source.

### *1.4.1e: CNT alignment by liquid based process*

---

Snow *et al*<sup>73</sup> proposed a simple route to large-scale ordered arrays of liquid-deposited CNTs. They prepared solutions of varying SWNT concentrations in a 1% sodium dodecyl sulfate (SDS) solution. The substrates were Si substrates with a 250-nm thick thermal oxide and were functionalized in order to produce an amine-terminated surface. These functionalized substrates were inverted and grazed against the surface of the SWNT solution such that a layer of solution remained on the surface. While still coated with this solution, the substrates were blown dry in a stream of N<sub>2</sub>. This resulted in an optically homogeneous thin film of SDS + SWNTs. The substrates were then rinsed with deionized H<sub>2</sub>O and dried again. This process was repeated to yield the desired resistance. AFM imaging of samples prepared in this manner showed that the deposited SWNTs were principally aligned in the N<sub>2</sub> stream flow direction

Zhou and co-workers<sup>74</sup> have demonstrated the preparation of ordered/micropatterned carbon nanotubes through the self-assembly of preformed CNTs on glass, and certain other substrates, by vertically immersing the substrate into an aqueous solution of acid-oxidized short SWNTs.

Dai *et al*<sup>75</sup> developed a Langmuir-Blodgett (LB) method achieving monolayer of aligned SWNTs with dense packing, central to which is a non-covalent polymer functionalization by poly *m*-phenylenevinylene-*co*-2, 5-dioctoxy-*p*-phenylenevinylene (PmPV) imparting high solubility and stability of SWNTs in an organic solvent: 1, 2-dichloroethane (DCE). Pressure cycling or "annealing" during LB film compression reduces hysteresis and facilitates a high-degree alignment and packing of SWNTs.

### *1.4.1f: Lattice-Oriented Growth of Single-Walled Carbon Nanotubes*

---

By making use of the substrate surface lattice orientation, SWCNT growth was attempted. First it was done on Si (111) and (100) surfaces<sup>76</sup>, the densities of CNTs in this technique is not high. Later by other groups, SWCNTs have been catalytically grown by CVD on a-plane, r-plane, m-plane, and c-plane sapphire<sup>77, 78</sup>.

Recently the Rogers group<sup>79</sup> obtained a high density of SWCNTs with this technique and they fabricated thin film transistor out of it. They obtained SWNTs with average diameters of ~1 nm, lengths of up to

300 mm, and densities (D) approaching  $\sim 10$  SWNTs  $\mu\text{m}^{-1}$ . But still these values are far from the integrated circuit device package density.

The CNTs grown by any of the above mentioned fabrication processes gives either metallic or semiconducting properties. Both large MWNTs with many concentric carbon shells, and bundles or “ropes” of aligned SWNTs, are complex composite conductors that incorporate many weakly coupled nanotubes, each having a different electronic structure. The seminal paper<sup>80</sup> on selective electrical breakdown of metallic SWNTs is popularly referred to as constructive destruction. In this approach, a gate bias is applied to deplete semiconducting SWNTs in thin-film FET geometry. Large currents are then passed through the conductive metallic SWNTs until they are electrically destroyed. Incidentally, a variation of this approach also allows individual shells of MWNTs to be removed electrically (shown in Figure 1-7).

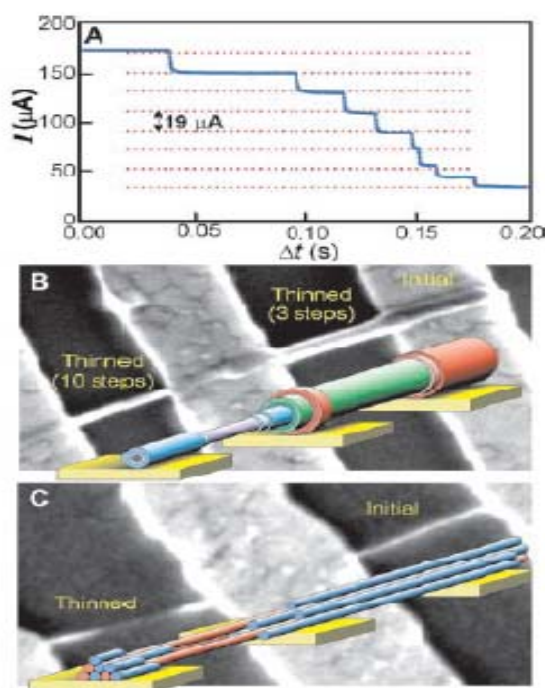


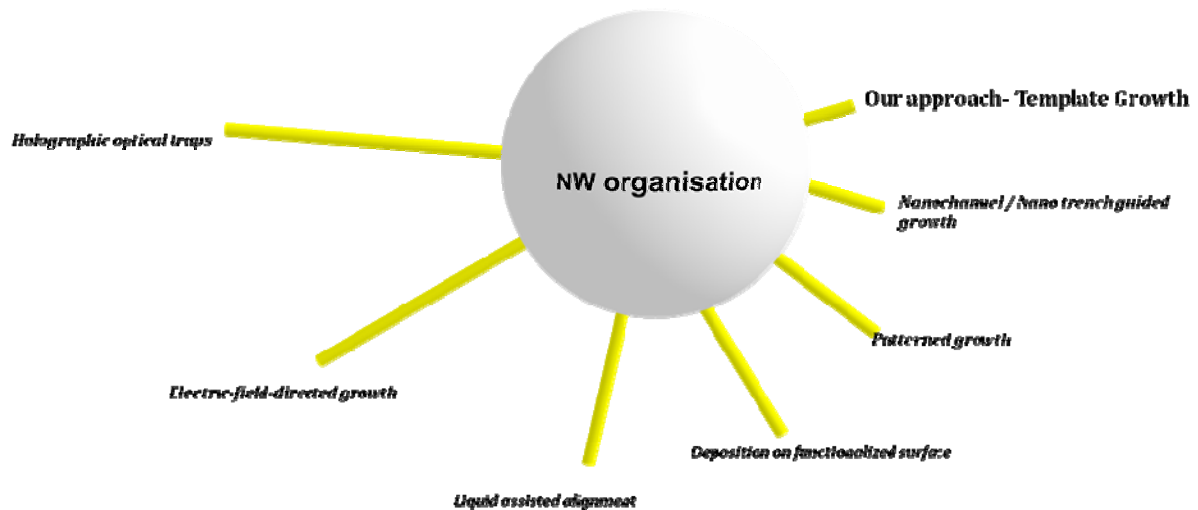
**Figure 1-7:** (A) the partial electrical breakdown of a MWNT at constant voltage stress proceeds in a series of discrete steps corresponding to the loss of individual carbon shells from the MWNT. Equally spaced dotted lines emphasize the surprisingly regular spacing. (B) Images of partially broken MWNTs show clear thinning, with a decrease in radius equal to the intershell spacing (0.34 nm) times the number of completed breakdown steps. The two segments of this sample were independently thinned by 3 and 10 shells, as depicted by the color overlays. (C) Similar thinning, as observed in SWNT ropes

In this approach collateral damages to adjacent SWNTs have been found during the destructive process. In addition, as selective destruction is typically an irreversible process, the eliminated SWNTs cannot be harvested for other applications. In order to avoid the destruction of SWCNTs, the tubes should be separated.

## 1.4.2: NWS

Different techniques available in the literature are given in the chart 2, where the length of the yellow line represents the magnitude of difficulty in process as well as degree compatibility with the industry.

Chart: 2: NW organization methods



### 1.4.2a: Electrical field-directed assembly

---

Applied electrical fields (E-fields) can be used effectively to attract and align NWs due to their highly anisotropic structures and large polarizabilities<sup>81,82</sup>. Although the E-field approach is simple to carry out, it does have two main disadvantages. The first is its dependence on conventional lithographic processes to pattern the electrodes. Another main disadvantage is that of fringing electric fields at submicron lengths.

### 1.4.2b: Fluidic flow-directed assembly technique

---

Due to limitations in the E-field process, another powerful assembly approach has been developed which is based on flow of fluids. This approach offers higher flexibility than that of E-field assembly, and it can

also be used for virtually any elongated nanostructures like CNTs and DNA molecules. In the fluidic flow-directed assembly method, NWs alignment is achieved by passing a suspension of NWs through a microfluidic channel, for example, formed between a poly dimethylsiloxane (PDMS) mould<sup>83,84</sup> and a flat substrate.

Virtually all NWs can be aligned along the flow direction at an adequate flow rate, leaving an array of parallel NWs assembled on the substrate surface within the microfluidic channel. The alignment can be readily extended to over hundreds of micrometers and is limited only by the size of the fluidic channel being used. It allows for the directed assembly of geometrically complex structures by simply controlling the angles between flow directions in sequential assembly steps. However, controlled assembly of NWs with the fluidic flow method at larger scales (> centimeter) is less practical and remains to be demonstrated.

For hierarchically organizing NW building blocks *en masse* into integrated arrays tiled over large areas, an alternative solution-based approach was developed by the Lieber group<sup>85</sup>, Yang group<sup>86</sup> and followed by others<sup>87</sup>. This approach exploits the Langmuir-Blodgett technique to uniaxially compress a NW-surfactant monolayer on an aqueous sub phase, thereby producing aligned NWs with controlled spacing. The compressed layer is then transferred in a single step to a planar substrate to yield parallel NWs covering the entire substrate surface. Similar to flow alignment, this sequence of steps can be repeated one or more times to produce crossed and more complex NW structures, where the NWs can be the same or different in sequential layers. The aligned NW structures exhibit features similar to a nematic liquid crystal phase, including fluctuations in the average alignment direction and poor end-to-end registry. These non-uniform features are distinct from the precise structures familiar to conventional top-down fabrication and also the NW density is found to be small in this method.

### *1.4.2c: Holographic optical traps*

---

Controlled assembly using electric fields or flowing fluids present a major advancement over random assembly. However, it is not possible to orientate SiNWs freely in any desired direction using the former approaches. Three dimensional structures offer possible interesting properties that lead to better functional behaviors. The Holographic optical traps approach provides the functionality of parallel assembly and manipulation of SiNWs. In this approach, SiNWs are suspended in a solution. This solution is exposed to a series of laser beam blasts that produce optical traps. The traps guide the relative movement and rotation of the SiNWs into a holographic image created by computer<sup>88</sup>.

In the above mentioned techniques, the NWs are formed on a substrate, sorted for size & length, and then positioned & aligned using some combination of different techniques like fluids and electric fields and subsequently fabricated into NW devices, such as transistors. Besides the multiplicity of cumbersome handling steps, the difficulty of obtaining acceptable inter device packing for practical applications is another disadvantage of grow-and-place approaches.

In order to solve this problem, it is better to adopt a “grow in place” approach. Two previous attempts to circumvent all these grow-and-place steps are found in the “patterned growth” and “growth-in-trenches” methods.

### *1.4.2d: Patterned growth*

---

The patterned growth technique was taken from the carbon nanotube growth-positioning approach. It has been first used for Ge nanowires<sup>89</sup> in a patterned fashion and was used for CVD growth to produce GeNWs (p-type or n-type) from patterned catalyst sites.

However, the patterned growth method does not give control over the number, direction, or inter-wire spacing of the nanowires produced

The growth-in-trenches<sup>90</sup> approach offers a novel way to grow SiNWs (nanobridges) between two vertical silicon surfaces. In principle, the resulting NWs can be used in place. However, the process cannot control the number nor spacing of the SiNWs produced. In addition, the technique requires Si wafer substrates for creating the initial vertical Si growth surfaces.

Fonash<sup>91</sup> introduced a nanochannel-guided grow-in-place approach. In this approach, SiNWs are grown so that they are extruded from, or confined within, a permanent nanochannel-template. The nanowire grow-in-place fabrication approach offers the potential for mass and environmentally friendly manufacturing. But this approach gives one NW for every channel; with this number it is very difficult to get the required densities on the CMOS scale. And also this process needs e-beam lithography.

### *1.4.2e: Top down approach*

---

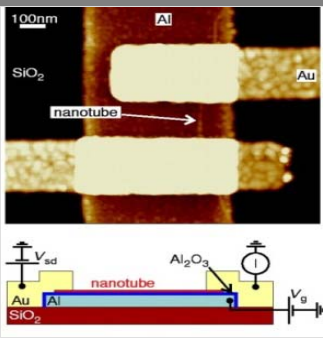
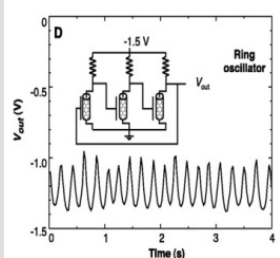
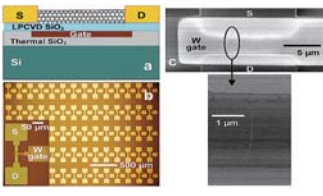
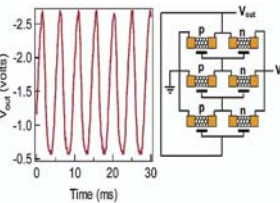
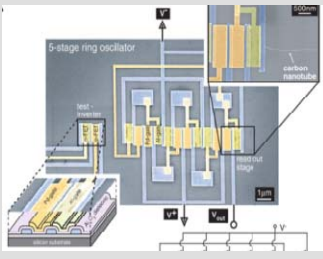
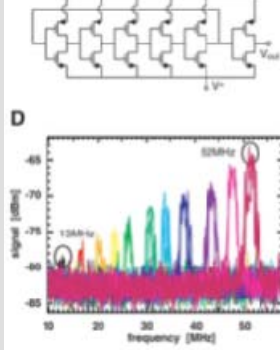
SiNWs were also fabricated by using several “top down” approaches based on electron beam lithography<sup>92</sup>, reactive-ion etching<sup>93,94</sup> or wet chemical etching process<sup>95</sup> applied to define SiNWs on silicon-on-insulator substrates. Similarly nanoimprint lithography<sup>96</sup> has been applied to fabricate arrays of

SiNWs. These approaches are found to be more compatible with industries, but still every step in this process has its known limitations, especially on the required density of the nano objects.

### 1.5: DEVICE

By using one or more above mentioned organization methods, electronics devices were fabricated by using NTs and NW<sup>97,98</sup>.

**Table 1-3: CNT and NW devices reported in the literature**

	Year	Device structure	Ring oscillator	Method
CNT	2001		 <p>5Hz</p>	Liquid suspension + AFM manipulation
	2002		 <p>220Hz</p>	Patterned growth
	2006			Dispersion / contact

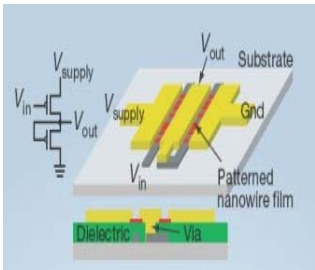
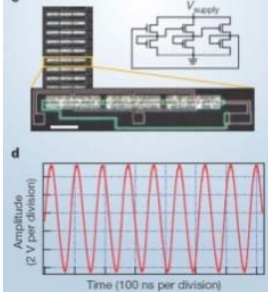
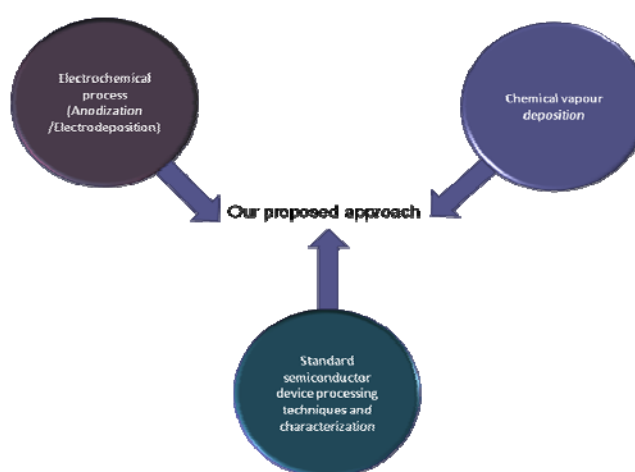
		52MHz		
SiNW	2005			Dispersion/ contact

Table 1-3 lists the logic devices made with CNTs<sup>99,11,100</sup> and NWs<sup>101</sup> so far, by different techniques. But these results are obtained by using single or few nano objects. Realization of devices in the CMOS scale is still very far to reach, with these results. So it is important to develop a technological solution to organize these nano objects in very high density, in a way to have a control on individual tubes or wires. In order to do this in the near future, it is better to find a way by using standard process rather than developing new process which is not compatible with industry standards.

## 1.6: CONCLUSION

In this work we are proposing a novel way, to organize the CNTs and SiNWs with the required densities by using templates. Ordered nanochannel – array materials have attracted increasing attention in recent years due to their utilization as templates for nanosize structures<sup>102,103</sup>. One approach to the fabrication of these structures has been to use a naturally occurring structure as a host for the fabrication. This approach is promising especially for the preparation of large-area, nanometer-sized structures with high aspect ratios which are difficult to form by a conventional lithographic process. Porous Anodic Alumina (PAA), which is prepared by the anodic oxidation of aluminum in an acidic electrolyte is one of the typical self-organized fine structures with a nanohole array, which has been studied in detail in various electrolytes over the last five decades<sup>104,105</sup>. Self-organized pore growth, leading to a densely packed hexagonal pore structure of anodic porous nanochannel has been reported for certain sets of parameters<sup>106</sup>. It is known that the alignment and distribution of nanotubes and nanowires are important in electronic device applications. Highly vertically aligned carbon nanotubes are generally fabricated on mesoporous substrates by chemical vapour deposition using PAA as templates<sup>107,108</sup>, which contains nanochannel with

diameter ranging from several nanometers to a few hundred nanometers. Si nanowires with well-controlled diameters ranging from 100 to 340 nm are also grown in alumina nanoporous membranes<sup>109</sup>. In the usual situation, the pore array and hence the array of template-grown nano objects are perpendicular to the surface of the substrate, which complicates (from a topographic point of view) the organization of electrical contacts, as far as three terminal devices are concerned. In the integrated circuit fabrication process, planar type configuration is preferred in order to have a high degree of integration. The need for lateral PAA structures is found to be an important step to realize planar type devices with the CNTs and SiNWs.



**Figure 1-8:** General outline of our approach

We are proposing a method, which is a combination of three different well established methods (i.e) Electrochemistry, Standard semiconductors fabrication techniques like Photolithography, PECVD, RIE ...etc, and CVD growth (Figure 1-8). So it is an interdisciplinary approach, with the combination of electrochemistry, engineering and physics.



## **Chapter 2: Porous Anodic Alumina templates**



---

## 2: POROUS ANODIC ALUMINA TEMPLATES

*This chapter mainly deals with the general anodization approach to obtain porous anodic alumina structures. Starting from the history of anodization, then the mechanisms of the porous anodic alumina growth and finally our results are shown and compared with the best results available in the literature. Overall this chapter indicates on the advantage of the porous anodic alumina system for the growth of nanostructure.*

### 2.1: ANODIZATION

All metals, except gold, are unstable at room temperature in contact with oxygen at atmospheric partial pressure, and thermodynamically should tend to form an oxide. In water many metals, such as aluminum, titanium and tantalum, displace hydrogen with the production of an oxide or a salt. These reactions often fail to occur at any appreciable rate. The usual reason for the lack of reaction is that a thin but complete film of insoluble or slowly soluble oxide is formed. This separates the reactants and further reaction can only occur by diffusion or migration (field-assisted movement) of metal or oxygen ions through the native oxide film. These processes are usually slow. Such transport does occur, thickens the film and therefore reduces the rate of reaction because of a decreased concentration gradient or electrostatic field.

Usually, an oxide coated metal is made on the anode of an electrolytic cell (with a solution that does not dissolve the oxide), the applied current sets up an electrostatic field in the oxide (or increases the field already present) and produces continued growth of the oxide film by causing metal or oxygen ions to be pulled through the film. Due to this reason this kind of films are called anodic films.

Among these various anodic films, generally aluminum has received significant attention due to its diverse applications. The first aluminum anodization dates back to 1880, the term anodization is an electrochemical passivation process, which grows oxide layer on the metal film. Initially, chromic acid was used for anodization and this process was called the Bengough-Stuart<sup>110</sup> process. Soon after this first sulfuric acid anodizing process was patented by Gower and O'Brien in 1927<sup>111</sup>. Sulfuric acid became the most commonly used anodizing electrolyte. The first industrial scale anodization process was started by Alcoa in Pennsylvania (USA) in 1930<sup>112</sup>. The highly reactive nature of aluminium metal is normally masked by the protective oxide film which is readily formed in moist air and renders the metal kinetically stable. This oxide layer on the aluminum film grown electrochemically is thin, dense and with a uniform thickness. The growth conditions and the thickness of this oxide layer can be varied. This has leads to

intensive studies of aluminum anodization to obtain protective and decorative coating. The morphology can be altered by selection of electrolyte and anodization conditions. Thus, the film growth at higher current in near neutral electrolytes at ambient temperatures gives relatively compact with higher thickness; such films are called barrier films. But in acid electrolytes or in some specific alkaline electrolytes, the compact barrier type anodic films have been no longer developed. This is due to the change in potential of an anode caused by current flow. The development of high resolution microscopy also gives way to understand these films, which reveals relatively porous structures. Careful observations of these porous alumina films have been done by Keller *et al*<sup>104</sup>. In particular, they have proposed structural features of this PAA using a hexagonal model in 1953<sup>113</sup>. Sullivan and Wood<sup>114</sup> have studied the detailed mechanisms of the formation of the porous anodic films. With the development of transmission microscopy Thompson and Wood have studied this porous alumina films<sup>115,116</sup>. In 1995 Masuda *et al* discovered a two step process of anodization which gives high degree of order in the pore arrangement with very high aspect ratio<sup>106</sup>. It was the starting point of a lot of investigation on these porous anodic films and it has opened many possible applications, especially nano devices applications<sup>117</sup>.

The PAA template allows one to manipulate the nanowire arrays and to incorporate them into a variety of potential designs of nano-devices. Figure 2-1 illustrates some of the possible fabrication steps proposed by J. M. Xu<sup>118</sup>.

Following anodization (Step I. 1) and optional pore widening (Step I.2), metal, semiconductor (SC) electrodeposition (Steps II.1-3) produces the array of nano-wires. The composition of the wires can be modulated at this stage along its length, resulting in the formation of p-n junction or heterojunctions (II.3). The next step (III.1) is the partial etching of the AAO template to expose the nano-wire tips for further processing. Steps III-2a-5a, 2b-3b, and 2c-4 illustrate several processing strategies at this stage:

- 1) Nano-wire array with contacts to one (tip emitters III.4a, or both ends III.5a)
- 2) Nano-wire array sandwiched between two insulating tunneling junctions (III.3b)
- 3) Array of the metal/SC nano-heterojunctions (III.4c)

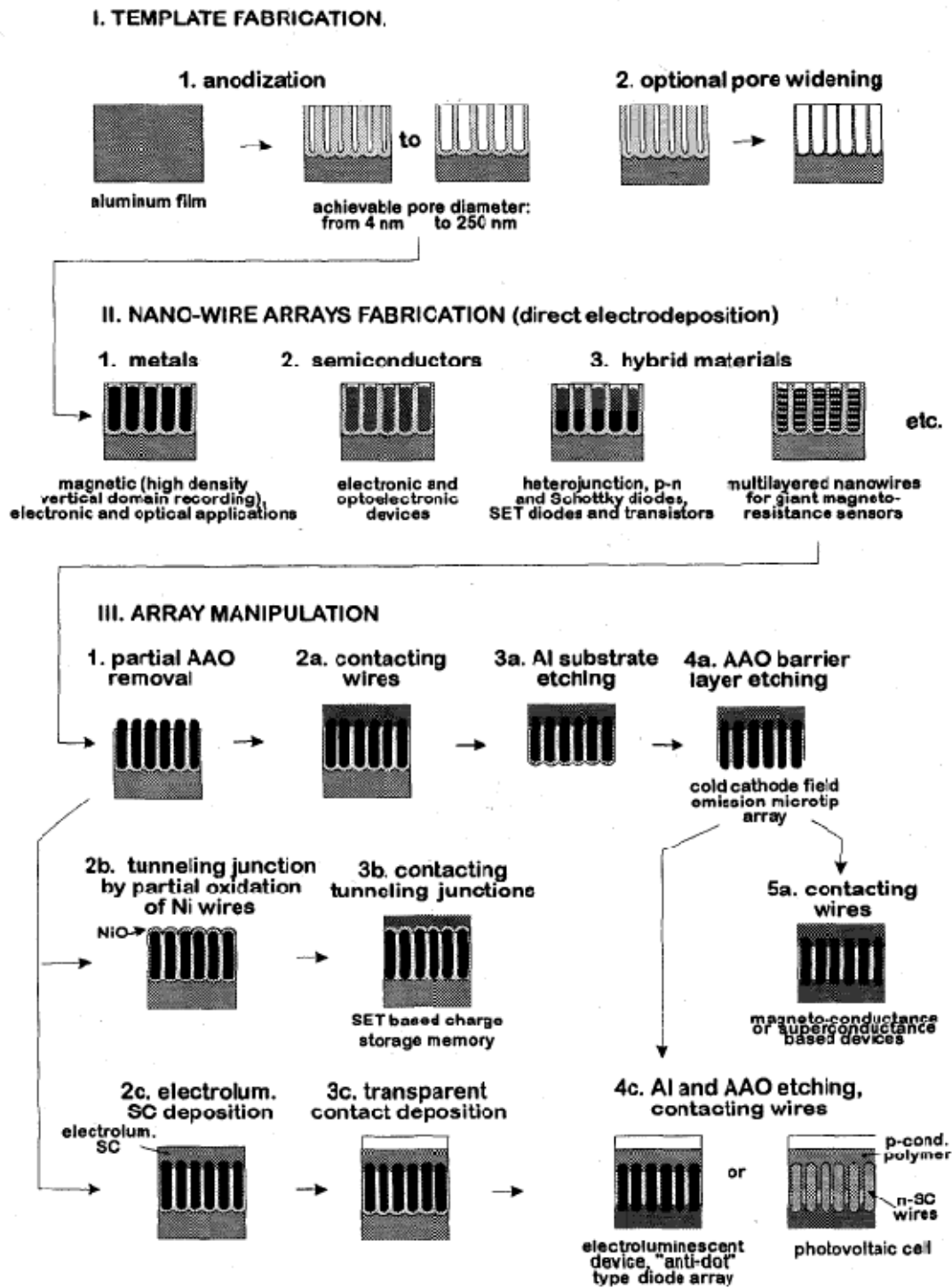
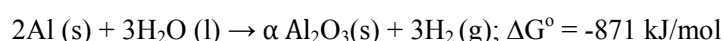


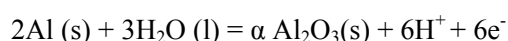
**Figure 2-1:** Processing steps in the fabrication of nanowire arrays and device prototypes using porous alumina template.

### 2.1.1. ELECTROCHEMISTRY OF ANODIC ALUMINA

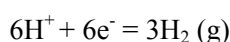
The spontaneous reaction leading to the formation of aluminum oxide in air can be ascribed to the large negative Gibb's free energy changes:



If aluminum is electrochemically anodized, an oxide grows at the anode electrode



and hydrogen evolves at the cathode:



Assuming there are no complex anions, the Nernst equation gives the equilibrium potential E:

$$E = E_o - \left( \frac{RT}{zF} \right) \ln \left( \frac{|\text{red}|}{|\text{ox}|} \right)$$

Where R is the universal gas constant, T is the absolute temperature in Kelvin, z is the charge number of the electrode reaction, and F is the Faraday constant (96.500 C mol<sup>-1</sup>). For aluminum the electrode potential E at the anode can be written at 25°C as:

$$E = E_o - (0.0591\text{V}/z) \log_{10} \left( \frac{|\text{red}|}{|\text{ox}|} \right)$$

$$E = -1.550 - 0.0591 \text{ pH}$$

This explains that the reaction at the anode electrode (Al) thermodynamically depends on the pH value.

### 2.1.2. POTENTIAL AND CURRENT TRANSIENTS

Both types of aluminum oxide, barrier-type and porous-type, can be anodized at constant potential or constant current monitored over time. The shapes of the current-time and potential-time transient curves are well established<sup>119</sup> and can provide insight into the growth mechanism and kinetics. Tajima *et al*<sup>120</sup> have classified the voltage – time and current- time transients into five different types depending on the physical phenomena that occur during oxide growth.

1. Barrier-type films: At constant current, the voltage is increasing linearly with time due to a linear growth rate of the oxide at constant field until the potential for breakdown is reached. At constant voltage, the current decreases exponentially with the time, to low leakage current values at long times.
2. Porous-type films: At constant current, the voltage increases linearly with time up to a critical value corresponding to the transition from barrier to porous- type films. Then voltage decreases slightly in order to reach a steady value, whose characteristics depend on the pH of the solution and the applied current density. At constant voltage, the current is decreases rapidly for a short period of time due to a sharp increase of barrier layer thickness. After a critical time which is associated with pore formation, the current is increases up to a steady value after a long time.
3. Pitting: At constant current, the voltage is increases up to a maximum value and then is decreases gradually over time to low currents. At constant voltage, the current decreases sharply during a short time down to a minimum and then increases slowly over time.
4. Electropolishing: At constant current in strong acids, the voltage fluctuates periodically or remains constant at low values.
5. Crystallographic chemical etching: In very strong acids where chemical etching of the oxide is occurring, any formed oxide is etched chemically by the electrolyte almost instantaneously and the voltage remains at very low values.

The growth of disordered pore domains has been studied in detail on the last few decades and a unique relationship between anodization voltage  $U$  and interpore distance “ $D_{it}$ ” was found<sup>121</sup> .

$$D_{it} \propto \alpha U$$

where  $\alpha$  is typically between 1.2 and 1.4 nm/V<sup>104</sup>.

### **2.1.3. THE MECHANISM OF STRESS GENERATION DURING THE GROWTH OF POROUS ANODIC ALUMINA OXIDE FILMS**

Various processes that occur during anodic oxidation of aluminum create stresses in both aluminum oxide and in the underlying aluminum substrate. Stress in the oxide can lead to cracks or delamination and affect the functional properties of alumina. They have been studied since the 1960s<sup>122,123,124,125,126</sup> . Stress

in thin films are mainly due to volume change, thermal mismatch, vacancy incorporation/annihilation, grain growth, lattice mismatch and other growth related stress generating mechanisms.

In films formed by anodic oxidation, the thermal mismatch stress is generally insignificant as the oxidation occurs at room temperature. Lattice mismatch between the oxide and the metal substrate has been attributed to stresses in the crystalline oxide films grown at high temperatures. In the case of anodic oxides, the oxide is generally amorphous and hence the mismatch stress has generally not been considered in the past. For the same reason, grain growth during anodization has also not been reported. Below we discuss the most common mechanisms for stress generation considered in the literature during anodic oxidation of aluminum.

- *Stress due to the volume change (Pilling –Bedworth Ratio(PBR) )*

The most often cited source of stress in growing oxides is due to the volume change that occurs when a metal is converted in to its oxide. Pilling and Bedworth first presented this as a ratio of the molar volume of the oxide to the molar volume of the metal.

For aluminum PBR can be expressed as

$$PBR = (M_{Al_2O_3}/2\rho_{Al_2O_3}) / (M_{Al}/\rho_{Al})$$

Where  $M_{Al_2O_3}$  and  $M_{Al}$  are the molecular weights of alumina and aluminum respectively, and the  $\rho_{Al_2O_3}$  and  $2\rho_{Al}$  are the densities of the aluminum oxide and aluminum respectively.

If  $PBR > 1$ , compressive stress can arise and if  $PBR < 1$ , tensile stress can arise in the oxide. PBR values between 1.3 and 2 have been reported depending on the density of the alumina<sup>127,128</sup>.

- *Stress due to vacancy incorporation/annihilation*

Anodic oxidation of aluminum occurs by movement of ions through the formed oxide. If anions move to the metal-oxide interface and react to form oxide, then the oxide is constrained by the substrate in the plane of the film to expand and hence can lead to compressive stress. However, if the cations move to the outer surface and react to form oxide, the oxide may be stress-free. Metal cation and oxygen anion transport numbers are dependent on the current density and this may give rise to changes in stress with current density.

Moon and Pyun<sup>126</sup> explained the observation of compressive and tensile stresses at low and higher current densities by annihilation and generation of point defects (Figure 2-2). According to their theory, the annihilation of aluminum vacancies in the oxide will lead to a compressive stress and the formation of oxide vacancies will lead to a tensile stress in the oxide.

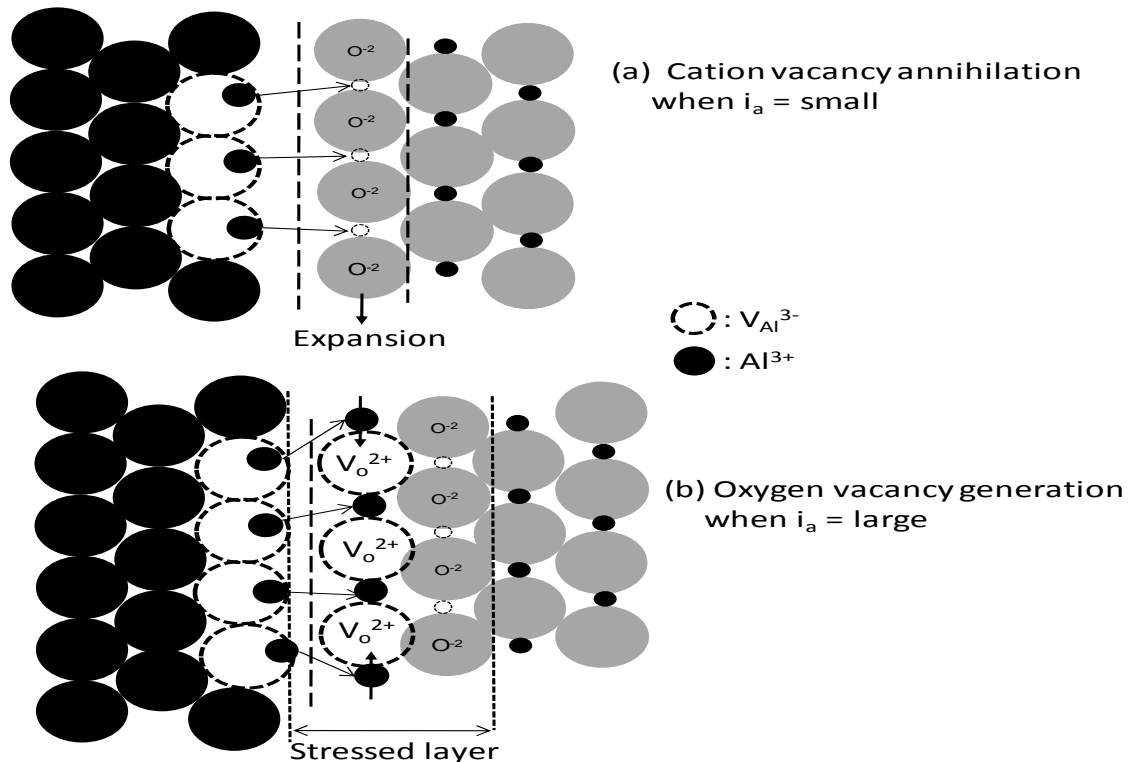
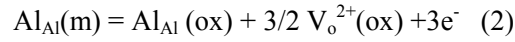
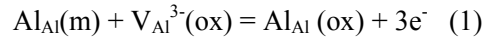


**Figure 2-2:** Schematic representation of two possibilities for ionization of metals at the aluminum/oxide film interface: (a) Annihilation of aluminum vacancies  $V_{Al}^{3-}(ox)$ ; (b) generation of oxygen vacancies  $V_O^{2+}(ox)$ ,  $i_a =$  applied anodic current density

It seems reasonable to assume that the molar volume of aluminum metal remains constant during the anodic oxidation and the free space formed by ionization of aluminum metal does not contribute to the change in molar volume of the oxide film. Therefore, when studying the stress generation mechanism during the growth of anodic oxide films, it is enough to consider only the molar volume change of the stressed oxide layer at the aluminum/oxide film interface.

The molar volume of the stressed oxide layer will be determined by the change in the concentration of vacancies within the stressed oxide layer which depends on the following two electrochemical reactions occurring at the aluminum/oxide interface according to the point defect model.



where  $\text{Al}_{\text{Al}}(\text{ox})$  is the aluminum atom in metal,  $\text{e}$  is the electron and  $\text{V}_{\text{o}}^{2+}(\text{ox})$  represent the positively charged oxygen vacancy in the oxide film.

Two different processes for ionization of aluminum metal at the aluminum/oxide film interface are schematically envisaged in Figure 2-2. The aluminum ions formed at the aluminum/oxide interface will enter their vacant sites in the oxide film (eqn 1), thus resulting in the annihilation of  $\text{V}_{\text{Al}}^{3-}(\text{ox})$  or they will adsorb on the oxide layer (eqn 2), thus causing the formation of  $\text{V}_{\text{o}}^{2+}(\text{ox})$ . It is clear that the annihilation of  $\text{V}_{\text{Al}}^{3-}(\text{ox})$  (eqn1) increases the molar volume of the stressed oxide layer, resulting in a compressive deflection, while the formation of the  $\text{V}_{\text{o}}^{2+}(\text{ox})$  decreases the molar volume of the stressed oxide layer, thereby producing a tensile deflection.

- *Stress due to the applied electric field (electrostriction)*

A metal-oxide-solution can be treated as a capacitor with the oxide dielectric. In a capacitor, the charges that are at the two ends exert a normal and attractive force. However, alumina is a rigid material and hence the electrostrictive force creates a compressive stress on the aluminum oxide normal to its surface. The magnitude of this stress is proportional to the dielectric constant ' $\epsilon$ ' and the square of the electric field strength ' $E$ ' and is given by

$$\sigma = (\epsilon / 8\pi) E^2$$

This compressive stress is often experimentally observed to be reversible (Nielsch *et al*<sup>127</sup>) i.e. the oxide relaxes when the electric field is removed and becomes compressive when the electric field is turned on.

- *Stress due to anionic impurities and composition variations*

Vermilyea *et al*<sup>122</sup> reported a tensile stress due to the presence of a hydrated oxide and proposed that it depends on the degree of physical trapping of water and on the extent of dehydration that occurs concurrently by migration of protons. Variations in composition of oxide and impurities in the original metal can also lead to stresses in oxides.

### 2.1.4. PORE FORMATION AND GROWTH MECHANISMS

The applications of porous alumina as a template for a variety of nanomaterials growth have spurred interest in understanding the formation and ordering of porous alumina over the past 10 years. Though the fabrication of porous alumina with well-controlled pore size, spacing and ordering is relatively a new topic of research, the porous alumina formation has been studied extensively in the past 50 years. While the control of the pore size, shape and ordering has been made possible from the work initiated by Masuda and co workers<sup>106,129,130</sup>, much of the understanding about the morphology, ion transport and the initial stages of pore formation is owed to Thompson, Wood and their co-workers who performed a variety of marker studies along with transmission and scanning electron microscopy analysis, beginning in the early 1970s<sup>131,132,133,116</sup>.

The time evolution of the porous alumina formation is captured in the TEM images shown by Sullivan and Wood<sup>114</sup>. At very short times, no pores are seen and a roughness similar to that of the initial electro polished aluminum surface is seen. Black dots appear over time, representing regions of locally thicker oxide film whose apparent density increases with time. The small nuclei then merge slowly leaving areas of locally thin oxide which over time results in pore formation. Cross section TEM images showed that the scallops in the aluminum surface formed simultaneously with the formation of the pores. Both the diameter of the pores and the spherical scalloped regions increase in size resulting in tear-drop shaped pores. The scallop size increases with time until they merge with other scalloped regions, thus resulting in porous alumina with uniform pore size at a steady state.

The theory of ‘field-assisted dissolution’ was first proposed by Hoar and Mott in 1959<sup>134</sup>. Sullivan and Wood later presented in detail a physical mechanism along with experiments showing the effect of field-assisted dissolution on the pore size, spacing and other porous-film properties. This paper is considered a classic work in the research area of porous alumina and has formed the basis for the current understanding of the porous alumina formation. They also measured the barrier layer thickness, pore size & spacing and established a direct relationship between the applied voltage and all of the above mentioned parameters. From all of the experimental observation, they proposed that the field-assisted dissolution involves stretching and breaking of the aluminum-oxygen bonds under the applied field. They argued that the electric field which is concentrated at the bottom of the pore weakened the aluminum-oxygen bonds and lowered the effective activation energy for dissolution which then led to field-assisted and thermally-enhanced dissolution at the bottom of the pore. They observed that anodization using relatively less-

aggressive electrolytes led to a thicker barrier layer, and increased pore size and spacing due to reduced field-assisted dissolution compared to more aggressive electrolytes. Finally they also concluded that the barrier-layer thickness, determined by the balance of oxide formation and field-assisted dissolution, also determined the cell and pore size by a simple geometric mechanism. However, they acknowledged that until it is possible to measure the field-assisted dissolution rate on a planar surface or estimate the field at the pore base by measuring the pore geometry as a function of field, it is not possible to quantify the field-assisted dissolution model.

Shimuzu *et al*<sup>133</sup> considered the pore initiation process as a transition from a barrier-type film to a porous-type film due to cracking of film under tensile stress as a result of PBR values less than 1. For films grown in neutral solutions at 100% ionic current efficiency for oxide formation, they calculated a rate of voltage rise of 2.3 V/Sec at 5mA/cm<sup>2</sup> from Faraday's law. They observed a decreasing slope in the voltage-time response with decreasing current and pH. The amount of aluminum ions in solution also increases with decreasing current density and pH, indicating a decrease in current efficiency. The PBR decreases from 1.7 at 100% current efficiency to lower values at lower current efficiency. Shimuzu *et al* argued that when the current efficiency drop below a critical value, the PBR values decreases to less than 1 (0.91 in the case of phosphoric acid) and proposed that the stress in the oxide contributed to local cracking of the film above pre-existing metal ridges (from electropolishing) on the metal surface. They also suggested that the cracked regions are repaired by the oxidation processes; however this leads to non-uniform film growth. The locally thinner regions then become preferred regions for pore development. However they did not confirm the presence of stress by experimental measurements and did not explain the mechanism for formation of pores with a characteristic spacing dependent on the applied voltage/current, pH and temperature.

Parkhutik and Shershulsky<sup>135</sup> proposed a theoretical model taking into account oxide growth at the metal/oxide and oxide/electrolyte interfaces as well as the field enhanced dissolution at the pore base. Their model started with porous alumina growing at the steady state and solved the Poisson equation, neglecting the space charge as well as transport of ions in the electrolyte. However, the model does not discuss how the system gets to the well-developed pore separation and size. The assumption of hemispherical pore base is also not valid. They also did not discuss if their analysis can consider the ordering dynamics of porous alumina. Surface tension effects on the interface electrochemical reactions are also neglected. Nevertheless, the model is able to predict the linear dependence of the pore spacing on the applied potential observed in experiments.

Thamida and Chang<sup>136</sup> performed a linear stability analysis of an initially flat oxide with both the metal/oxide and oxide/solution interfaces moving at the same speed. They concluded that the oxide is unstable to small perturbations as the curvature causes focusing of the electric field at the troughs and defocusing at the crests. Their mathematical model contained a second order source term related to field-enhanced dissolution and a fourth order dissipation term related to the lateral drainage of field strength due to diffusion of transverse potential gradient. They predict the inter pore spacing or diameter of the each cell ( $d_{\text{cell}}$ ) to be proportional to the applied voltage  $U$  and pH by

$$d_{\text{cell}} / U = [2.96 / (2.31 - 1.19\text{pH})] \text{ (nm/V)}$$

They also predicted for  $\text{pH} > 1.77$ , pores do not form due to a thick barrier layer. While at high pH, a transition from a porous to a barrier layer has been reported by others as well. The pH values for barrier-type growth observed experimentally are much higher than their predicted value of 1.77. Furthermore they performed a non-linear theoretical analysis and compared pore morphologies. They modified the model proposed by Parkhutik and Shershulsky<sup>135</sup> to incorporate the actual shape of the pores experimentally seen and predicted the pore diameter and porosity dependence on the applied voltage and pH. However, their model could not predict the ordering of pores and they proposed that long range effects like space charge or anions in the oxide are the cause of such self-organization of the pores, as they tend to arrest pore growth and allow lateral adjustment.

Though the model proposed by Thamida and Chang<sup>136</sup> as well as Sullivan and Wood relies heavily on the concept of field-enhanced dissolution at the bottom of the pore, there is a subtle difference in their physical basis of field-enhanced dissolution. According to Sullivan and Wood<sup>114</sup>, field-enhanced dissolution is caused by bond stretching at the pore base, while Thamida and Chang<sup>136</sup> presented a pure geometric argument for increased field at the pore bottom. However, we questioned both these models presenting a simple schematic of an undulated surface during any electro dissolution process. Still the detailed mechanism of the porous anodic structures is not clear.

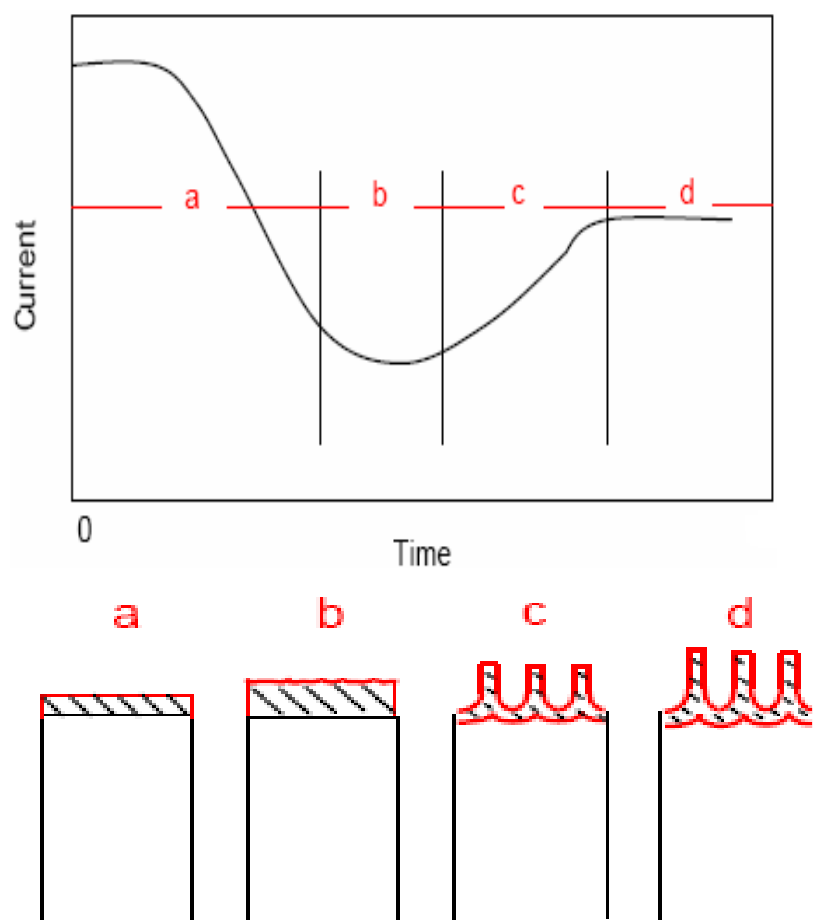


**Figure 2-3:** Schematic diagram of the kinetics of porous oxide growth on aluminium in (a) potentiostatic regime (b) The stages of porous structure development are also shown

### 2.1.5. GENERAL PRINCIPLE

According to the existing point of view reviewed by many, porous oxide growth includes the following effects.

- (1) Application of anodic potential to an aluminum sample immersed in acidic ( $\text{pH} < 6$ ) or alkaline ( $\text{pH} > 10$ ) baths causes porous oxide growth with either ordered cellular or fibrous structure. Aluminum anodization in the intermediate range of pH values is also assisted by porous oxide formation but with a rate as slow as dense non porous oxides.
- (2) Porous oxide growth includes several stages that are easily detectable by monitoring the dependence of voltage (or current) on time<sup>137</sup> or that can be directly observed by high-resolution electron microscopy<sup>105</sup> these stages are schematically presented in Figure 2-3. Immediately after

switching-on the anodic bias a barrier oxide layer starts to grow (Stage a). Relatively fine featured pathways are then revealed in the outer regions of the barrier oxide prior to any true pore formation (stage b). Further anodizing results in the propagation of individual paths through the barrier oxide with their heads becoming enlarged (stage c). Finally, a steady-state pore structure is formed by closely packed cylindrical cells, each containing a pore at the centre and separated from the aluminum metal by a layer of scalloped hemispherical barrier oxide (stage IV). Geometrical parameters of the pores are related to the anodization variables (electrolyte concentration, regime of anodization etc).

- (3) Elementary processes involved in porous structure formation (Figure 2-4), as well as characteristic geometrical features of the pores, are presented in Figure 2-3. The oxide grows at its external boundary as a result of the outward migration of aluminum ions (mainly by a place-exchange mechanism) and their reaction with oxygen-containing electrolyte species. This boundary is also dissolved as a result of field-stimulated interaction of electrolyte species with the oxide surface. At the same time the oxide/aluminum interface is shifted inward in the samples due to interaction of moving oxygen species with aluminum. As a result, the electric field imposed on the Al-Al<sub>2</sub>O<sub>3</sub>-electrolyte system plays an important role in porous oxide growth.
- (4) The electric field distribution in the scalloped barrier oxide at the pore bases is inhomogeneous both laterally and inward in the oxide. Its depth dependence arises, first of all, from the non-planarity of the barrier oxide layer and also from the space charge accumulated in the oxide during its growth. This charge is shown to reach maximum value at the moment of the paths appearance in the barrier oxide and is caused by an incorporation of anionic impurities into the outer oxide layer. The maximum electric field coupled with the space charge is about  $4-6 \times 10^8 \text{ Vm}^{-1}$  at the oxide surface and falls rapidly towards the inner oxide boundary<sup>138</sup>. Compared with the external electric field necessary to maintain the anodic oxide growth (about  $2 \times 10^9 \text{ Vm}^{-1}$ ) the space charge field may be neglected during the anodization process, but afterwards, when the anodization is terminated and external field is switched off, this electric field starts to play an important role in electrical properties of oxides.

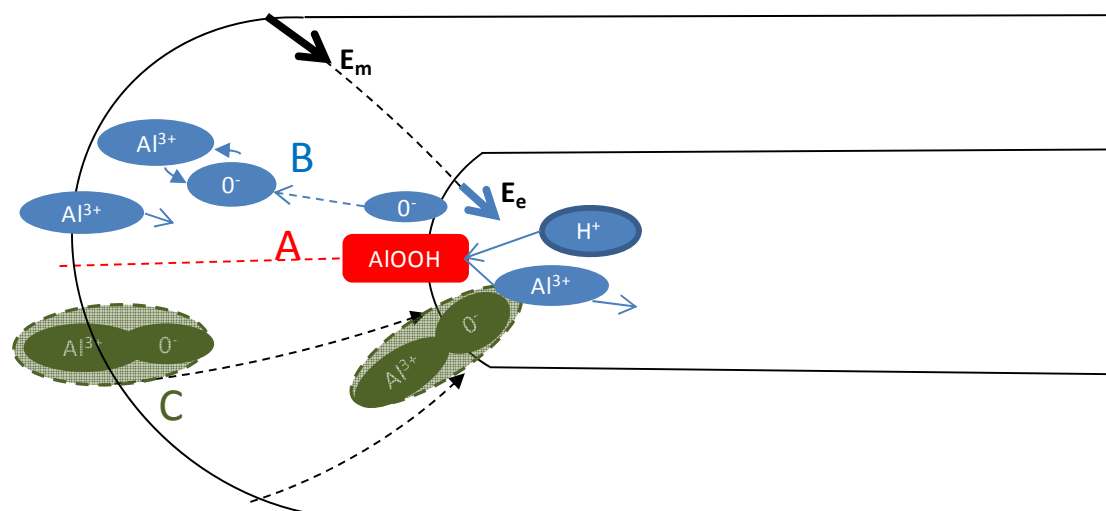


**Figure 2-4:** The elementary processes involved in porous oxide growth: A: oxide dissolution by the proton-assisted electric field enhanced mechanism, B: movement of oxygen anions and aluminium cations through the barrier oxide by the field-stimulated mechanism, C: oxide growth at both internal and external oxide interfaces as a result of ionic species movement. The dotted lines represent the electric field vector

### 2.1.6. PORE ORDERING MECHANISMS

Anodic porous alumina forms as a self-assembled hexagonally packed porous structure over a certain range of applied potentials and electrolyte concentrations. Though Masuda *et al* and others have shown remarkable control over the self-ordering of porous alumina to obtain highly ordered pore arrays, the mechanism for the ordering process is less understood and only very few methodical experiments on pore ordering have been reported<sup>139,127,140</sup>.

Jessensky *et al*<sup>139</sup> measured experimentally the volume expansion of the aluminum during anodic oxidation of aluminum and the current efficiency in oxalic and sulfuric acid solutions as a function of applied voltage. They concluded that the optimal conditions of voltage and pH for the self-ordering of pores occur at moderate volume expansions. They further proposed that the resulting mechanical stress at the metal-oxide interface causes repulsive forces between the neighboring pores which promote the self-ordering of pores. Li *et al*<sup>128</sup> performed anodization in phosphoric, oxalic and sulfuric acid solutions under appropriate conditions of self-ordering and reported a volume expansion of approximately 1.4 for all of the self-ordered regimes. Based on the volume expansion and the porosity, they calculated the stress in alumina to be 4 Gpa (compressive). However, they pointed out that experimental values of the stress in

barrier-type films reported by Bradhurst and Leach<sup>141</sup> do not match the calculated values. Furthermore, their explanation for the cracks observed at high voltages near breakdown based on high compressive stress is questionable as compressive stresses generally lead to buckling of films.

Niensch *et al*<sup>127</sup> measured the porosity under conditions of ordering and found that porosity was equal to ~10% for various self-ordering voltages and concentrations which corresponds to a volume expansion of about 1.2. They explained their results based on the theory proposed by Jessenky *et al*.

The model proposed by Jessenky *et al*<sup>139</sup> raises several serious questions. First, the simple argument based on the PBR or volume expansion has been shown in many experimental systems to be invalid. The measured stresses are in fact tensile with most of the stress present in the aluminum beneath the oxide. This is clearly in contradiction with the proposed model by Jessenky *et al*<sup>139</sup> based on pore repulsion due to compressive stresses.

Recently, Ono and co workers<sup>140</sup> performed anodization in various electrolytes and reported the porosity as a function of applied voltage. They observed that the porosity value approaches 10% at high voltages close to the breakdown potential. Self-ordering was also observed under these conditions and suggested that the high current density or high electric field strength is the key controlling factor for self ordering. However, it is unclear whether the porosity value of 10% is the lowest value observed before breakdown as in oxalic acid solutions, breakdown does not occur even up to 80V while self-ordering is observed at 40V.

### 2.1.7. MODEL FOR POLYCRYSTALLINITY

Lim *et al*<sup>142</sup> have put forward a simple model describing the pore growth based on the Voronoi diagram. They start their simulation with a random distribution of etch sites, having a minimum distance of “a”. Then pores grow laterally until they touch each other and Lim and co-worker have obtained a good agreement between this model and the disordered ANOPORE membranes<sup>143</sup>.

In 1995, Randon *et al*<sup>144</sup> discussed the possibility that pores may not grow exclusively randomly. This was based on observations of Kondo *et al* from 1988<sup>145</sup>, where they obtained rather regular pores arrangements. Randon *et al*<sup>144</sup> discuss the possibility that the initial etch sites are much more dispersed leading to fewer pore initiations. They assume that once a pore starts to grow, other pores arrange themselves hexagonally around the initial one forming hexagonal symmetry. Even before the Masuda *et al* first reported self-ordered structures. Mathematically, their Voronoi model is based on the ratio R of surface coverage of initial etch sites to the total surface area:

$$R = N (a^2 \sqrt{3}/2) / \text{total area}$$

If R is equal to one, one has the densest package of initial etch sites N, thus a completely disordered, i.e., amorphous porous alumina film and one obtains the results of Lim *et al.* If R is approaching zero, one obtains a single crystal. In the intermediate range polycrystallites are obtained.

There are two problems with the rather intuitively looking model of Randon *et al.*<sup>144</sup> Experimentally hexagonal arrangements are not obtained instantaneously but the size of the crystallite increases with time<sup>146</sup>. Initially, the pores are randomly ordered and it takes typically one or two days of anodization in order to obtain polycrystallites with diameters of few microns<sup>147</sup>. Second, there is no physical reason in their model, why the pores should arrange themselves hexagonally. For example during macroporous silicon growth in resistive p-type silicon, the mean interpore distance is determined by twice the width of the space charge region<sup>148</sup>. However, even for very long etching times, there is no hexagonal ordering, even though it would be the densest package. The conclusion of this experimental observation and the comparison to macro porous silicon is that a moderate repulsive force between the pores exists which favors energetically the densest package of pores. The most prominent force is mechanical stress based on the ratio of the volume expansion of alumina to aluminum<sup>140</sup>. By variation of the voltage for a given electrolyte concentration, the volume expansion ratio can be changed from 0.8 to 1.7 (O. Jessensky *et al.*<sup>139</sup>). Neither of the values below or equal to one nor for values higher than 1.4 they observe polycrystalline growth. For values lower or equal to one there is no repulsive or even an attractive force, leading to amorphous growth<sup>128</sup>. For values higher than 1.4, the mechanical stress causes a large amount of lattice defects limiting the poly-crystallite size. For one electrolyte concentration, there exists one optimum voltage where one obtains ordered pore growth, i.e., has a volume expansion factor in the range of 1.2 and 1.4.

This means that the lattice constant, i.e., the short-range order is determined by the anodization voltage and the medium range order is determined by the chemical composition of the electrolyte. If the steady-state pore diameter would be the same for all voltages and electrolytes and the composition of the alumina in the pore walls would also be the same for all the electrolytes, then one would expect only one condition for ordered pore growth. However there are different optima for different electrolytes and even for the same electrolyte, the optima changes with the concentration. This shows that either the steady-state pore diameter is different for different etching conditions or the walls are not of the same material for different electrolytes. Indeed, it is well known in literature that both phenomena occur. According to literature, the

pore diameter depends mainly on the kind of the acid and its pH<sup>149</sup>. The smallest pores are observed for sulfuric acid<sup>150</sup>. The pore diameter is increased for oxalic acid and is largest for phosphoric acid reported by the famous paper of Sullivan and Wood<sup>114</sup>.

This means that for the same anodization potential, the pores in sulfuric acid are much smaller than in oxalic acid. In order to obtain the same porosity, the lattice constant has to be smaller. For phosphoric acid, the lattice constant should be larger for optimum growth since the diameter for the same anodization potential as in oxalic acid is larger. For example, the initial porosity of porous alumina made in oxalic acid is typically around 5-6 % considering an initial pore diameter of 25nm with a lattice constant of 100nm. For sulfuric acid, with an optimum lattice constant of 50nm, this porosity corresponds to an initial pore diameter of about 12nm, shown by Li *et al.*<sup>107</sup> In chromic acid, where up to now no ordered pore growth has been observed, the lattice constant is expected to be similar to that of the oxalic acid since the pore diameter is similar. The pore wall composition is also not constant for the different electrolytes. Typically, the pore walls consist of two main layers: an inner layer of relatively pure alumina and an outer layer of anion-contaminated alumina. The trend of the ratio of the inner to the outer layer increases from sulfuric acid (0.05), to oxalic acid (about 0.1) to phosphoric acid (about 1) to chromic acid (>1)<sup>151</sup>. Presumably the outer layer will have a slightly lower density due to the anion contamination. Therefore, the trend observed in sulfuric, oxalic and phosphoric acid favors even more a difference in the optimum lattice constant. However, to make a quantitative analysis of the different contribution, better experimental values of the initial pore diameter for the different acids and the density of the inner and out porous alumina have to be determined.

### **2.1.8. EFFECT OF THE ELECTROCHEMICAL CONDITIONS ON THE PHYSICAL AND CHEMICAL PROPERTIES**

A summary of the dependence of various parameters on the applied voltage, current, temperature and pH are listed in the table 2-1. The result listed with question marks in the table denotes previously reported data that are inconsistent or lack of sufficient data to make conclusive arguments.

Table 2-1: Effect of anodization conditions on the physical and chemical properties of the pore structure

	Steady state voltage	Steady state current	Pore size 'd'	Pore spacing 'D <sub>it</sub> '	Barrier thickness 'D <sub>b</sub> '	Pore density N <sub>p</sub> = 1/D <sub>it</sub> <sup>2</sup>
<b>Increasing pH</b>						
At fixed voltage	Fixed	Decreases (strong)	Negligible change	Increases (weak)	Increases (strong)	Decreases (weak)
At fixed current	Increases (strong)	Fixed	Increases	Increases (strong)	Increases (strong)	Decreases (strong)
<b>Increasing temp</b>						
At fixed voltage	Fixed	Increases	Increases ??	Negligible change	Decreases	Negligible change
At fixed current	Decreases	Fixed	Decreases (weak)	Decreases	Decreases	Increases
<b>Increasing voltage</b>						
At fixed pH,T	Fixed	Increases (strong)	Increases	Increases (strong)	Increases (strong)	Increases (strong)
<b>Increasing voltage</b>						
At fixed pH,T	Increases (strong)	Fixed	Increases	Increases (strong)	Increases (strong)	Increases (strong)

### 2.1.9. TREND IN POROUS ANODIC ALUMINA STRUCTURES

It is very important to choose the proper range of conditions with the proper electrolyte, to grow different nano objects in the nanopores. Nanotubes are very small in the range of 0.5nm to 2 nm for SWCNTs and from 5nm to 50nm for the MWCNTs. But in the case of nanowires the diameter is larger, say from 10nm – 200nm. So it is necessary to work in different regimes of the anodization conditions. Here we have compared the general trend for the aluminum anodization with the respective nano-objects. Recently this trend was further extended with different acids, such as malonic acid at 120V having 300nm, tartaric acid at 195V having 500nm and citric acid at 240V having 600nm pore intervals<sup>152</sup>

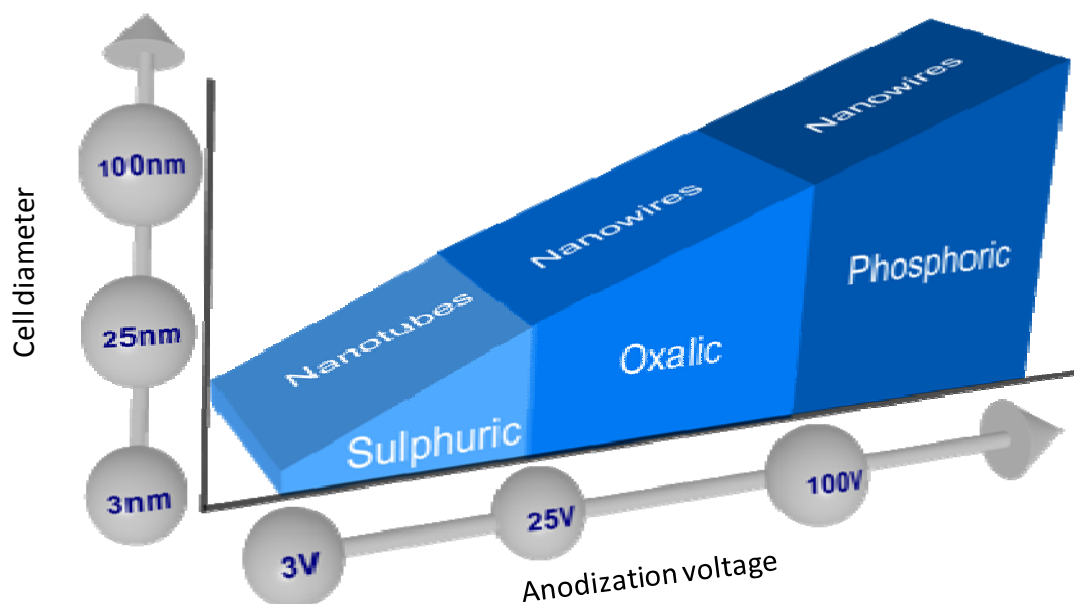
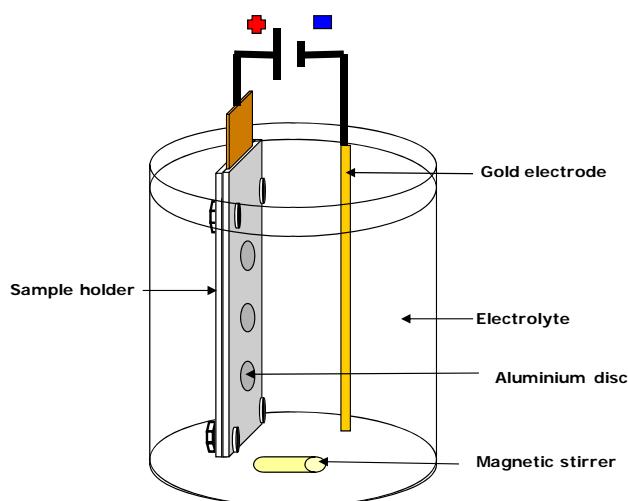


Figure 2-5: Standard trend in Porous anodic alumina structure

## 2.2. EXPERIMENTS

Figure 2-6 shows the setup which we use for electrochemical experiments (anodization). The cell consists of a two-electrode system, e.g., a gold or carbon rod acting as the counter electrode and an Al disc acting as the working electrode. The Al disc is inserted in the sample holder, which is made of Neoflon PCTFE (polychlorotrifluoroethylene). Only 2 cm of the aluminum disc is exposed to the acid through the opening in the sample holder. Even two more discs can be anodized at the same time, by using the other two openings (shown in Figure 2-6). The temperature is maintained by the cooling system (not shown in the Figure 2-6). The cell is put inside a double walled beaker, which is connected to a cooler by using a refrigerated circulating bath. The potentiostat/galvanostat has a working range of either 0-200 V (potentiostatic mode) or 0-100 mA (galvanostatic mode).



**Figure 2-6:** Experimental setup

Pure aluminium sheets (99.999%) of 1mm thickness are degreased in acetone by ultrasonication. After ultrasonication, the specimens were rinsed several times in ethanol for more than 15min, and finally rinsed in deionized water. The specimens were electropolished in a mixture of perchloric acid and ethanol ( $\text{HClO}_4$ :  $\text{C}_2\text{H}_5\text{OH}$ =1: 4 in volumetric ratio) to remove surface irregularities. The specimen was used as an anode while a flat Au sheet or graphite sheet was used as a cathode. The distance between the cathode and the anode was adjusted to be about 5 cm. A constant voltage of 8 V was applied between the cathode and the anode for 60-90 sec and the solution temperature was kept to be room temperature during electropolishing. The electropolishing time was varied with the characteristics of the used Al specimens such as thickness and surface roughness. A constant voltage was applied by a power supply. After electropolishing, the specimen was several times rinsed in deionized water and finally dried in an air stream. Next, the first step anodization was carried out in an acid electrolyte solution; the conditions for anodization such as temperature of electrolyte, anodizing voltage and first anodizing time were varied to find an optimum. Experimental setup was the same as what was used in electropolishing, except that acid was used instead of a perchloric acid-ethanol solution. After the first anodization was completed, PAA layer was removed by immersing the specimen in a mixture of 1.8 wt% chromic acid and 6wt% phosphoric acid at  $65^\circ\text{C}$  for few hours even sometimes over night. Finally, PAA film was obtained by the second anodization under the same condition as the first one. At all steps, the solution was stirred at a constant speed by a magnetic stirring bar. Electropolishing and anodizing were all carried out in a 500mL or 1 L jacketed-beaker, which was designed to keep the temperature of the

contained solution constant. The structure of AAO films was observed with Field Emission Scanning Electron Microscope (FE-SEM, Hitachi s-4800).

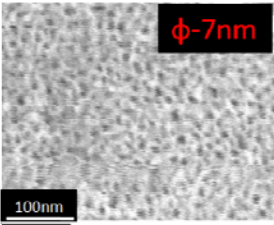
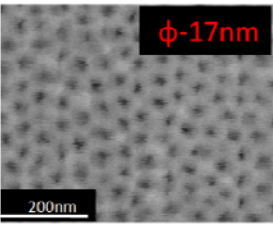
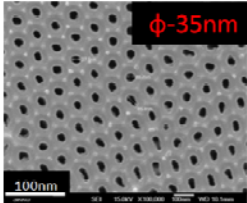
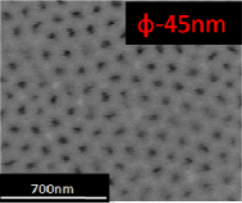
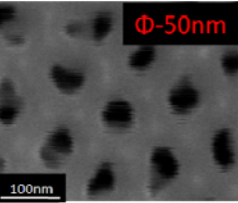
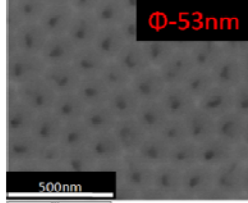
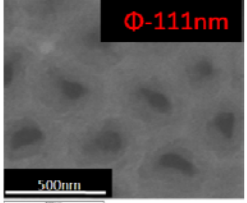
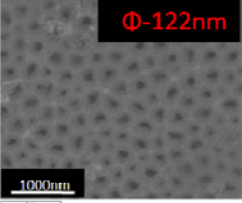
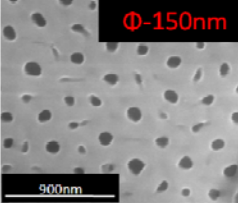
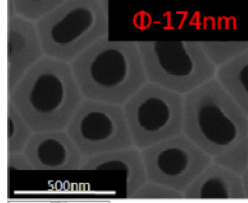
### 2.2.1. RESULTS AND DISCUSSION

Table 2-3 shows the PAA structures with different pore diameter by adjusting the anodization conditions. To study the PAA structures and to control the pore diameter, we started with the vertical templates in the beginning. The main concern is the pore diameter tuning, so we changed the anodization conditions (i.e) applied voltage, different acids, temperature, and pore widening time. For the pore diameters below 20nm, we used sulphuric acid, for the pore diameters ranging from 20nm to 100nm, we used oxalic acid and finally for pore diameter between 100nm to 200nm, we used phosphoric acid. This knowledge of the choosing the acid with respect to the desired pore diameter range is done after analysed the previous reported results (shown in Table 2-1 and Table 2-2).

**Table 2-2 : Summary of previous investigation<sup>153</sup>**

Group	Ordering method	Pretreatment	Electrolyte	Temp. (°C)	Voltage (V)	Pore diameter	Ordered domain size
Al-Mawalawi et al.	No ordering	No	0.23 M Oxalic acid	25	11-20	n.a.	No ordering
Masuda et al.	Long anodization	No	0.3 M Oxalic acid	0	40	67±6	~2-3 μm
	2-step anodization	No	0.3 M Oxalic acid	17	40	50	n.a.
	Long anodization	No	0.3 M phosphoric acid	0	195	n.a.	>5 m
	Indentation	400 °C, 1 hr	0.3 M Oxalic acid	17	40	70	3 mm × 3 mm
			0.3 M Oxalic acid	17	60	100	3 mm × 3 mm
			0.04 M Oxalic acid	3	80	140	3 mm × 3 mm
Li et al.	Long anodization	400 °C, 3 hr	0.3 M sulphuric acid	10	25	30	1-3 μm
			0.3 M Oxalic acid	1	40	70	1-3 μm
			10 wt% Phosphoric acid	3	160	250-300	1-3 μm
	2-step anodization	400 °C, 3 h	0.3 M Oxalic acid	5	40		1-5 μm
	2-step anodization	400 °C, 3 h	H <sub>3</sub> PO <sub>4</sub> : CH <sub>3</sub> O H : H <sub>2</sub> O=1 : 10 : 89	-4	195	200	1-5 μm
	Pre-patterning by lithography	400 °C, 3 h	0.04 M Oxalic acid	5	85	120	
Jessensky et al.	Long anodization	500 °C, 3 h	0.3 M Oxalic acid	1	30-60 best 40	70	~μm size
			20 wt% Sulphuric acid		18-25 best 18.7	40	Smaller than that in oxalic acid
				1			
Zhang et al.	Modified 2-step anodization (3-step)	No	3% Oxalic acid	15	40	n.a.	4 μm
	2-step anodization	No	0.3 M Oxalic acid	15	40	n.a.	0.5-2 μm

Table 2-3: Pore diameter ( $\Phi$ ) control

Acids	Different pore sizes			
Sulphuric acid				
Oxalic acid				
Phosphoric acid				

It was previously reported that the ordered domain size depends on the first anodization time and anodizing voltage (Li *et al*<sup>107</sup>), is generally called as self ordered regime. However, these effects are not so prominent. Although there is some ordering of pores at 40 V at 30°C, they do not have a perfect hexagonal arrangement. At high voltages or high temperature, oxide dissolution rate at the pore bottom may increase because the enhanced electrical field and current density shows large fluctuation. Therefore, local temperature may increase, so that stresses and rates of heat dissipation become non uniform at the pore bottom. Also, because the extent of volume expansion of aluminum oxide during anodization was

larger, the pore arrangement might be disordered (Li et al). At low voltages or low temperature, though anodization is very stable, the pore arrangements became very disordered. Because the repulsive interaction might become smaller, the expansion of volume during oxide formation at the Al/Al<sub>2</sub>O<sub>3</sub> interface is smaller. However, a regular pore array can be obtained if anodization is carried out for a long time.

Figure 2-7 shows the comparison of our results with the Nielsch *et al* results, where the overall trend matches very well.

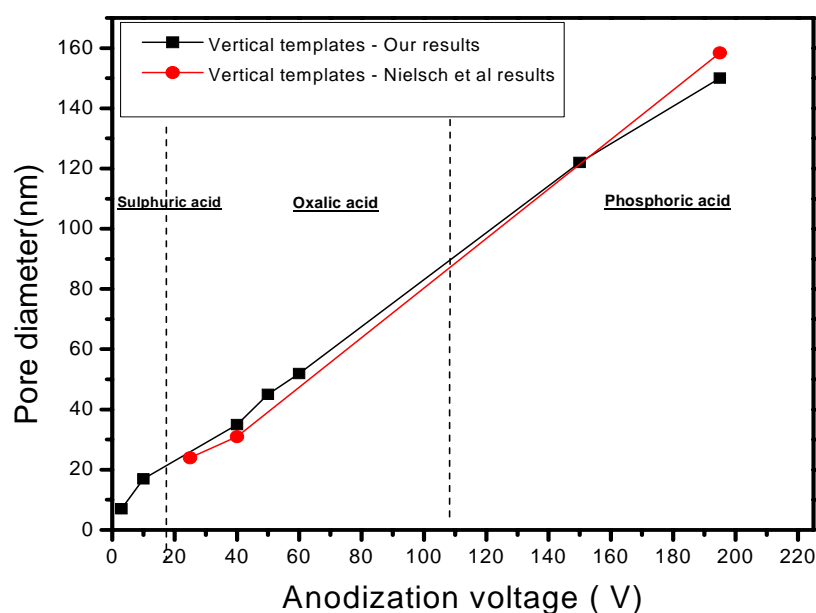


**Figure 2-7:** Pore diameters versus anodization voltage trend for our vertical templates (square) compared with the Nielsch *et al* results (circles)

### 2.3 .CONCLUSION

From the knowledge gained from our results on these vertical PAA templates; we transferred this to the lateral PAA templates. Since our concern is mainly focused on the placement and the pore density control, we worked not only in self ordered regime but also in all non self ordered regimes. Over all we gained complete control of the structural parameters of these PAA structures.



## **3: Lateral Porous Anodic Alumina Templates**



### 3: LATERAL POROUS ANODIC ALUMINA TEMPLATES

*In this chapter, we have shown how the lateral templates have been made with different pore sizes starting from 5nm to 100nm, controlling different pore arrays for the controlling pore density and finally we discussed the mechanism for the pore ordering in spatially constrained anodization. These above mentioned points are very important for controlling the lateral placement and the density of the nano objects of interest.*

#### 3.1. INTRODUCTION

Most of the reported organization methods (as shown in chapter 1) provide NWs or CNTs with linear densities below  $10/\mu\text{m}$ <sup>79,154</sup>, when densities of up to 30 to  $50/\mu\text{m}$  could be reached with NWs exhibiting diameters ranging between 10 to 20 nm. The linear density could even be higher for CNTs, where the diameters of interest for device purposes lie in the nanometre range. Also, most of the above mentioned examples of organization techniques do not solve the problem of end-to-end registration, which is another drawback as far as device packing density is concerned. PAA provides a uniform diameter distribution for CNTs and NWs, as well as a high packing density, up to several  $10^{11}$  pores/cm<sup>2</sup> (and above), depending on the anodization conditions<sup>107</sup>. PAA can also provide a natural 3-dimensional packing if lateral structures are employed.

In 1993 Masuda *et al*<sup>155</sup> attempted the fabrication of lateral alumina templates on glass. In general, the dimensions of the porous structure of the films depend on the formation conditions, i.e., electrolyte composition, applied voltage, and temperature. This new process allows the fabrication of a high-aspect-ratio micro hole array without any lithographic step. For about a decade there was no significant result reported in the literature, regarding the lateral PAA structures. In 2005 our group<sup>156</sup> came up with the solution and has shown lateral PAA using a device compatible approach.

Zhi Chen *et al*<sup>157</sup> reported the fabrication of one dimensional array of nano pores (similar to Masuda *et al*<sup>155</sup>) but this process is not device compatible due to the fact that they fractured the surface along the entire length of the substrate and they use SiO<sub>2</sub> of two micron thickness which is not easy for the device fabrication. Consequently we need to pattern lateral templates on silicon substrates in specific locations using a device compatible fabrication, as has been demonstrated in our previous work. This approach allows reproducibility of device fabrication in planar configurations.

### 3.2. EXPERIMENTAL DETAILS

The idea is to pattern an aluminum layer on a  $\text{SiO}_2$  wafer and cap it with the  $\text{SiO}_2$  on three sides leaving the fourth face exposed. Since adhesion between the capping layer and the aluminum should be strong, to avoid any electrolyte penetration,  $\text{SiO}_2$  is deposited by PECVD at  $300^\circ\text{C}$ . This problem has been addressed by X. Zhao *et al*<sup>158</sup>.

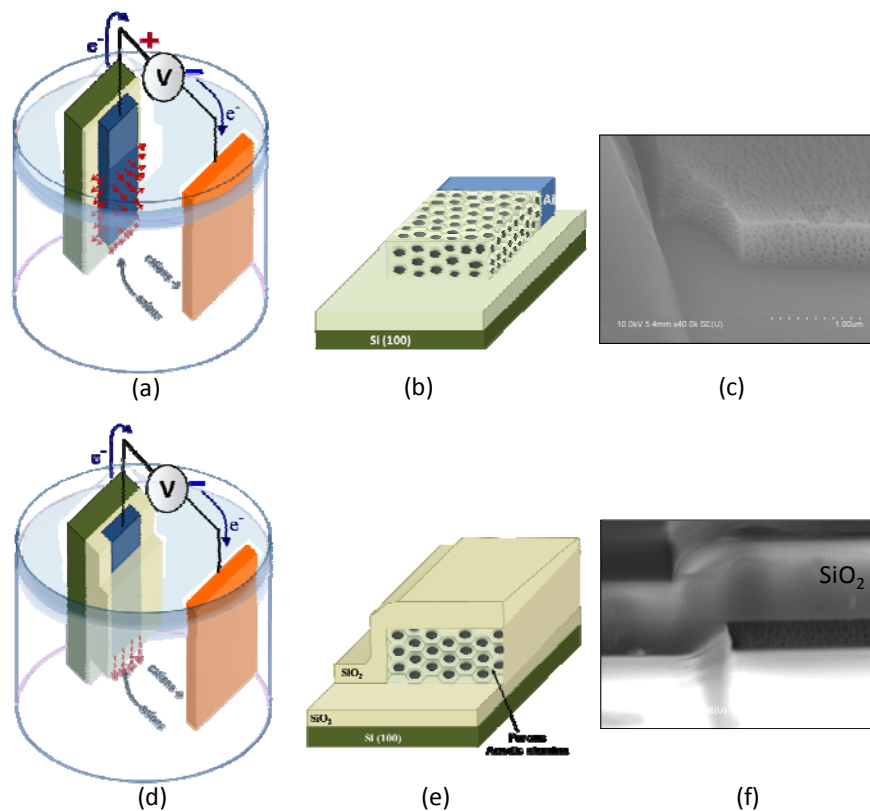


**Figure 3-1:** Anodization cell with uncapped (a) and capped aluminum (d) where red arrows are the electric field lines, pore formation on the uncapped aluminum and capped aluminum shown in (b), (e); (c) and (f) shows the SEM image of the pores formed on the uncapped aluminum and capped aluminum

Figure 3-1 shows the general scheme that we use to synthesize PAA membranes having their pore direction parallel to the surface of the substrate.

For the experiments presented here, we have deposited aluminum thin films by DC magnetron sputtering on silicon wafers covered with 500nm thermal oxide. The Al thickness ranged from 50nm to 2000nm. The Al films were subsequently etched in stripes with different widths, ranging from 1 to  $50\mu\text{m}$  and separated by equal spacing. There are five consecutive stripes of the same width followed by another set

in ascending order (*i.e.* 1, 2, 5, 10, 20, 50  $\mu\text{m}$ ). After Al etching, a 500nm thick insulating layer of  $\text{SiO}_2$  was deposited on the aluminum patterned wafer by rf-plasma enhanced CVD, thus covering the stripes. This  $\text{SiO}_2$  layer was then patterned and reactive ion etched (RIE) using a second mask consisting of two openings, one at the front and one at the back. The opening at the front side is perpendicular to the first network of Al stripes and the opening at the back side provides an electrical contact to the Al thin film for electro polishing and anodic oxidation. This process step left the Al locally exposed on both sides. Prior to performing anodic oxidation, the  $\text{SiO}_2$ -capped Al stripes we have prepared (experimental details of the sample preparation is given in the Annex I) were partially immersed into an electrochemical bath of perchloric acid in ethanol (25 volume %) and they were electro polished for 2 to 10s at 2 to 5 V constant voltage at  $0^\circ\text{C}$  ( $\pm 0.5^\circ\text{C}$ ). The anodic oxidation experiments were carried out with different acidic solutions (say 0.3M sulphuric, 0.3oxalic and 0.1M phosphoric acid) and different voltages, as summarized in Table 3-1. During the anodization the acid bath was continuously magnetically stirred and kept at constant temperature. The anodic voltage was applied between the exposed Al peripheral part (the latter being maintained out of the electrochemical bath) and an Au counter-electrode immersed in the electrochemical bath. Depending on the desired pore diameter different voltage values have been used, varying between 10 and 100 V. All anodic oxidation experiments have been carried out at constant applied voltage while the anodic current could flow freely. To study the ordering quality of the porous structures, a two-step process has been also performed in few cases. The first oxidation is carried out for typically a few minutes, followed by oxide dissolution in a mixture of chromic acid (1.7 wt %) and phosphoric acid (6 wt %) for 5 minutes at  $60^\circ\text{C}$ . A second oxidation is then performed under the same conditions as the first one. After anodization, the lateral pore structure looks like that shown in Figure 3-1 (f). The morphology of the samples after anodic oxidation was investigated with a Hitachi S4800 FEG high-resolution scanning electron microscope (SEM), working at 1 kV. For the thin aluminum samples the capping  $\text{SiO}_2$  was removed, prior to observation, by a standard RIE process ( $\text{CF}_4$  and  $\text{CHF}_3$  1:5 mixture), thus exposing the Al stripes and the porous alumina membrane. To ensure better observation of the lateral pore structure we also used focused ion beam etching (FIB) of the membranes (Zeiss CrossBeam 1560). For the pore diameter calculation from the SEM images we used the “Image J” program (public domain image processing and analysis program developed at the Research Services Branch (RSB) of the National Institutes of Health (NIH), USA). For the rectangular portion of about 1 to 2 rows in the centre of each image we made a plot profile (grey value versus distance along the image). This plot consists of peaks and troughs; the width of the trough portion gives the pore diameter. The pore

diameter value and interpore distance which are shown in the present work are the average values calculated from these plot profiles.

After the entire process the four inch wafer is cut into separate cells. Before anodization a short electro polishing step is performed at a temperature of 0°C and precise control of the etched length is achieved by diluting the solution with ethanol.

### 3.3. RESULTS AND DISCUSSION

#### 3.3.1. MODIFIED ELECTROPOLISHING:

In order to obtain the pores in the lateral direction, it is necessary to use a straight Al face. Masuda *et al*<sup>155</sup> used is a mechanical fracture, which does not give a good result. To obtain well-organized pore arrays, parallel to the surface of the substrate and also parallel each other, we have found that it was necessary to start the anodic oxidation (anodization) with a sharp and straight face for the Al film. Moreover, the Al face also needs to be perpendicular to the substrate and not tapered. All these features are obtained with our modified electro polish step before starting the anodization. Note that the same result could be obtained by a proper RIE processing of the Al thin film. With the above requirements on the geometrical aspect of the starting Al film and the direct consequence of the field-assisted mechanism of pore formation, the pores will be perpendicular to the local equipotential, i.e., the very Al wall in our case<sup>159</sup>. When the Al film is simply chemically etched, a meandering edge is observed, leading to interpenetration of the pore structure after anodization, as shown on Figure 3-2. This situation would obviously be detrimental for device-oriented nanotubes or nanowires organization.

Another way is to etch the aluminum is to use the commercial etchant; which is isotropic and will give the concave structure and also meandering surface, due to the difference in the etching rate between grain and grain boundary.

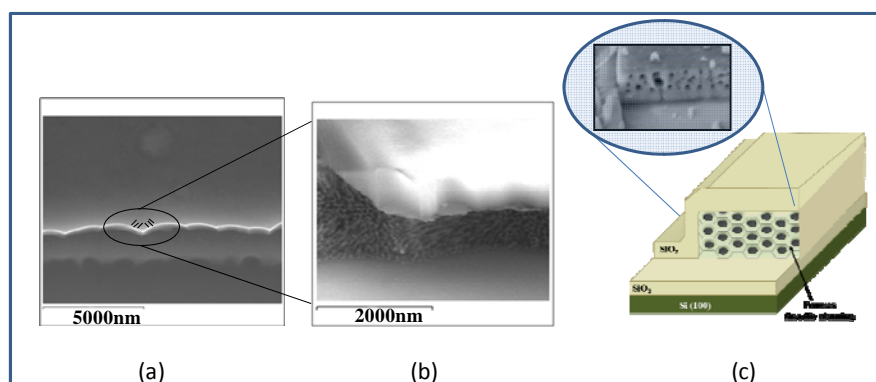


**Figure 3-2:** (a) Aspect of the *chemically etched* Al etch front after removal of the top SiO<sub>2</sub> cap, the lines represent the electric field direction upon anodization. (b) The anodic membrane replicates the meandering etch front of the starting Al film inducing some “mixing” of the pores. (c) Shows the anodic membrane after our modified electro polishing process (see text for details)

In general, electro polishing of aluminum is done on aluminum foils or thick aluminum films to decrease the roughness of the aluminum. Usually it is done by L1 electrolyte, which consists of 1050cc ethyl alcohol, 150cc butyl cellosolve, 93cc perchloric acid and 205cc distilled water. It is done under dc conditions with the Al foil placed at the anode, in contact with the electrolyte. In our case we used only perchloric acid and ethanol.

Anodic dissolution of metal during polishing involves both electrical and chemical phenomena on the surfaces. The ethanol acts as a high-kinematic-viscosity and wetting solvent for the molecules/ions involved in the dissolution. The high viscosity ensures the ion flux to the electrode is not affected by bulk turbulence and eddy currents, which can introduce large-scale non uniformity. According to the bulk kinetics study of Vidal and West<sup>160</sup>, water molecules are the bulk acceptor molecules that provide the necessary ions to react with Al<sup>3+</sup>, the aluminum ion released by the dissolving Al anode. The perchloric acid is to achieve the proper low pH to ensure that Al ionizes into Al<sup>3+</sup> and does not form other ions or oxides in the anodization reaction. The perchloric acid ions act essentially as catalysts on the metal that release the Al<sup>3+</sup> ions. Since perchloric acid is a strong oxidizer, it can often oxidize violently at elevated temperatures. In addition to careful temperature control, the ethanol concentration was increased, to provide good control of the etching rate.

Figure 3-3 gives more details on the pore formation and development in the two cases. The wide arrow denotes the localized electric field with respect to the particular point, which is always perpendicular to the surface. The dotted line shows the direction of the development of the pore. For case (a) the aluminum

face is not straight, so most of the initiated pores merge after some time. But in case (b) the aluminum face is straight and the pores are initiated and developed.

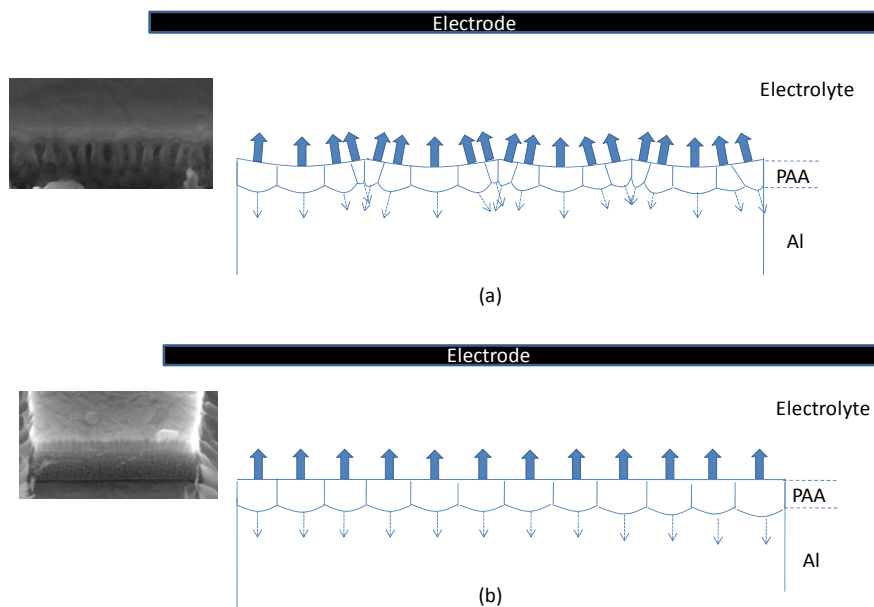


**Figure 3-3:** (a) Pore growth and pore merging (pore curving is also shown before pore merging) in meandering structure (b) Pore growth on straight aluminum

### 3.3.2: PORE DIAMETER CONTROL:

At this point, for our purpose we emphasize that different pore diameters are needed depending on whether CNTs or semiconductor NWs are of concern. In other words, pore diameters in the 3 to 5 nm range are interesting for templating CNTs, whereas for semiconductor NWs, the range of diameters can spread between 10 and 100 nm. Typically, the pore diameter  $\phi$ , and the interpore distance,  $D_{\text{int}}$ , are proportional to the anodization voltage ( $V$ ). In other words,  $\phi = k_1 V$  and  $D_{\text{int}} = k_2 V$ , where  $k_1 \sim 1.29$  nm/V and  $k_2 \sim 2.5$  nm/V<sup>161</sup>. This relationship probably varies depending upon anodizing conditions and also with our thin aluminum stripes (detail explanation found in spatially constrained anodization section). Under appropriate anodic oxidation conditions, very regular self-ordered, honeycomb-like hexagonal arrays with a circular pore at the center of each hexagonal cell can be obtained<sup>162</sup>. This self-ordering regime of pore growth seems to originate from an equilibrium where the mechanical stress at the  $\text{Al}_2\text{O}_3/\text{Al}$  interface (due to volume change upon oxidation) is partially compensated by a  $\sim 10\%$  porosity of the anodic oxide<sup>127</sup>. Generally speaking, the ordering quality of the pores depends on the anodic

voltage and every acid has a specific voltage range where the ordering is found to be high. For example in the case of oxalic acid, an anodic voltage around 40 V seems to be preferable in order to obtain highly ordered structures. The same phenomenon occurs for sulphuric and phosphoric acids, but at around 20V and 160V respectively. On the other hand, the type and the concentration of the electrolyte for a given voltage have to be selected properly in order to obtain pores with given diameters. In other words, the choice of the type of electrolyte is restricted for ordered arrays. Usually, the anodization of aluminum is carried out in sulfuric acid at low voltage ranges (5 V-30 V), oxalic acid is used for medium voltage ranges (30 V-120 V) and phosphoric acid for high voltage ranges (80 V-200 V). These restrictions are due to the conductivity and pH value of the various electrolyte solutions. For example, if aluminum is anodized in sulfuric acid at a high voltage (note that sulfuric acid has a very high conductivity), breakdown of the oxide layer takes place. In addition, the pH-value of the electrolyte determines the diameter of the pores or more precisely the size of the hexagonal cell around one pore. The lower the pH value, the lower the voltage threshold for field-enhanced dissolution at the pore tip. Therefore, since the pore diameter is directly proportional to the anodization voltage, small pore diameters are obtained in the lowest pH value i.e., in the strongest acid (sulfuric acid) and large pore diameters are formed by using phosphoric acid. Interestingly, Nielsch *et al*<sup>127</sup>. have shown that, whatever the pore diameter and inter-pore distance, self-ordering occurred as long as the porosity of the anodic alumina remained around 10%.

**Table 3-1:** Variations of pore diameter versus the anodization voltage in different acid

Sample	Acid	First anodization			Oxide removal (sec)	Second anodization			Pore diameter Ø* (nm)
		T (°C)	V (V)	t (sec)		T (°C)	V (V)	t (sec)	
<b>a</b>	Sulphuric	0	10	300	300	0	10	300	11
<b>b</b>	Oxalic	0	20	300	300	0	20	300	16
<b>c</b>	Oxalic	0	25	300	300	0	25	300	22
<b>d</b>	Oxalic	0	40	300	300	0	40	300	36
<b>e</b>	Oxalic	0	50	3000	0	0	0	0	62
<b>f</b>	Phosphoric	0	100	3000	0	0	0	0	87

\*Ø - errors will be in the range of <5nm and the decimal values are rounded off

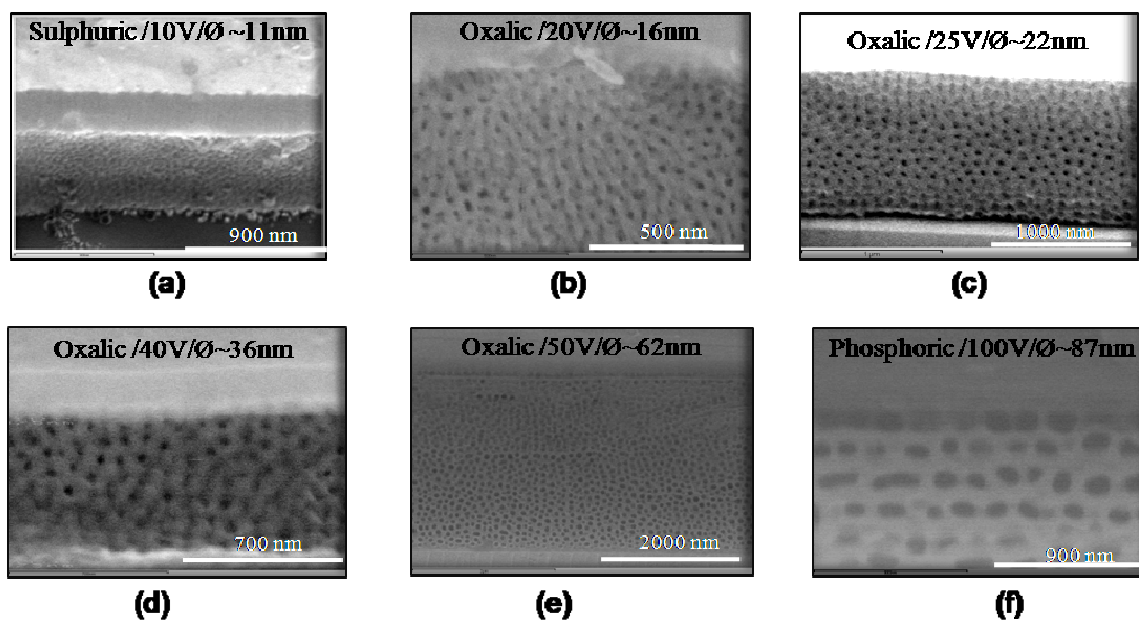


**Figure 3-4:** Scanning electron microscope images of the lateral templates showing different pore diameters obtained by changing the anodization voltage and the acid electrolyte (the top part of each picture gives the type of acid / anodization voltage/approximate pore diameter)

**Table 3-2:** Porosity calculation<sup>a</sup>

Sample	V (Volts)	Ø* (nm)	r=Ø/2 (nm)	D <sub>int</sub> (nm)	P%
<b>a</b>	10	11	5.5	44	6
<b>b</b>	20	16	8	54	8
<b>c</b>	25	22	11	106	4
<b>d</b>	40	36	18	101	11
<b>e</b>	50	62	31	98	36
<b>f</b>	100	87	43.5	198	17

<sup>a</sup> for the samples shown in Figure 3-4 , \* errors will be in the range of < 5nm and the decimal values are rounded off

Table 3-1 and Figure 3-4 shows the variations of the pore diameter with respect to the anodization voltage in different type of electrolytes. Following Nielsch *et al.*<sup>127</sup>, we calculated the porosity of the hexagonal structure using the following equation.

$$P = \frac{2\pi}{\sqrt{3}} \left( \frac{r}{D_{\text{int}}} \right)^2$$

where  $r$  is the radius of the pore and  $D_{\text{int}}$  is the inter-pore distance.

Since  $r/D_{\text{int}}$  is constant in the self ordering regime, we find a porosity around 9% for the 40V oxalic acid sample which is obviously the best organized one (see Figure 3-4). For the other samples the porosity varies significantly from 5% to 40% (shown in Table 3-2), due to the anodization voltages which do not correspond to the self-ordered regime. So whether the anodization is performed in a vertical or lateral way it does not seem to change the 10% porosity rule.

In order to get pores of small diameter (~10nm or below) we started with low anodization voltage. Therefore we used sulfuric acid with a concentration of 0.5M and a bath temperature of 0°C. But the degree of self-organization of the structure is less when compared to the observation of the pore structure made with oxalic acid (Figure 3-4), which is probably due to the higher oxide growth rate and lower Al dissolution rate. As also quoted above, self organization increases when we increase the voltage towards the self ordered regime. This phenomenon is shown in Figure 3-4(b), (c) and (d) for the case corresponding to the anodization in oxalic acid, where the anodization voltage rises from 20V to 40V. Previous studies<sup>163</sup> have shown that ordered pore arrangement occurs in a stable anodic state, i.e., stable voltage and current. During anodization at 100V (in  $\text{H}_3\text{PO}_4$ ) the anodization current is not stable (not shown here) which leads to the disordered pore arrangement. Chemical pore widening is done for the samples shown in Figure 3-4(e) and (f) just after the first anodization instead of the second anodization.

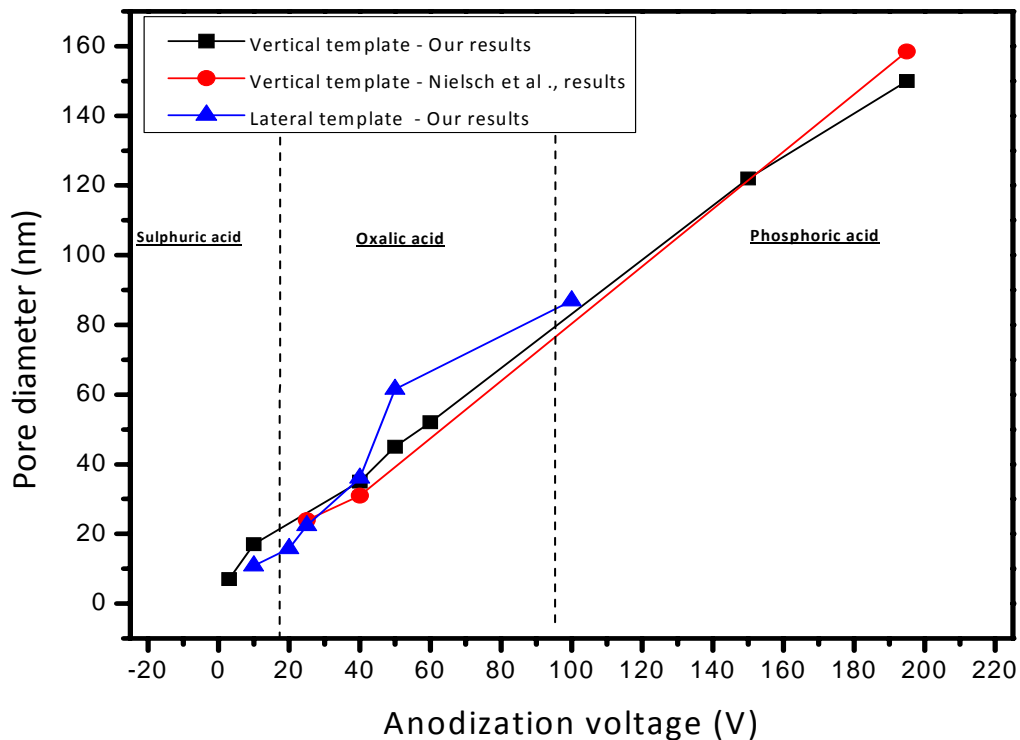


**Figure 3-5:** Pore diameters versus anodization voltage trend for our vertical templates (square), the lateral templates (triangle) compared with the Nielsch *et al*<sup>127</sup> results (circles)

In Figure 3-5 we show the comparison of our vertical and lateral template results. It seems there is no significant difference between them. And also these results are comparable with the general trend. Here we have taken Nielsch *et al*<sup>127</sup> as reference. The sudden jump in the pore diameter for the lateral template (blue triangle) for 50V is due to the chemical pore widening explained before.

For a better observation and to check the ordering across the length of the membrane, we locally etched some of the membranes by using a FIB gun. The schematic diagram of the experiment is shown in Figure 3-6(a) and (b). The sample is etched by sputtering with Ga ions at different places along the length of the membrane and the result is observed using the *in-situ* SEM. The substrates are also etched partially to get the proper window for comfortable observation. During this sputter-etch of the subsequent layers (including the substrate as mentioned) we noticed some re-deposition of the sputtered materials. This is shown in Figure 3-6(c), where only the central part of the picture reveals the pore structure. For the

particular membrane shown here (oxalic acid 25 V), the observed order inside the membrane is comparable to that observed at the front edge.

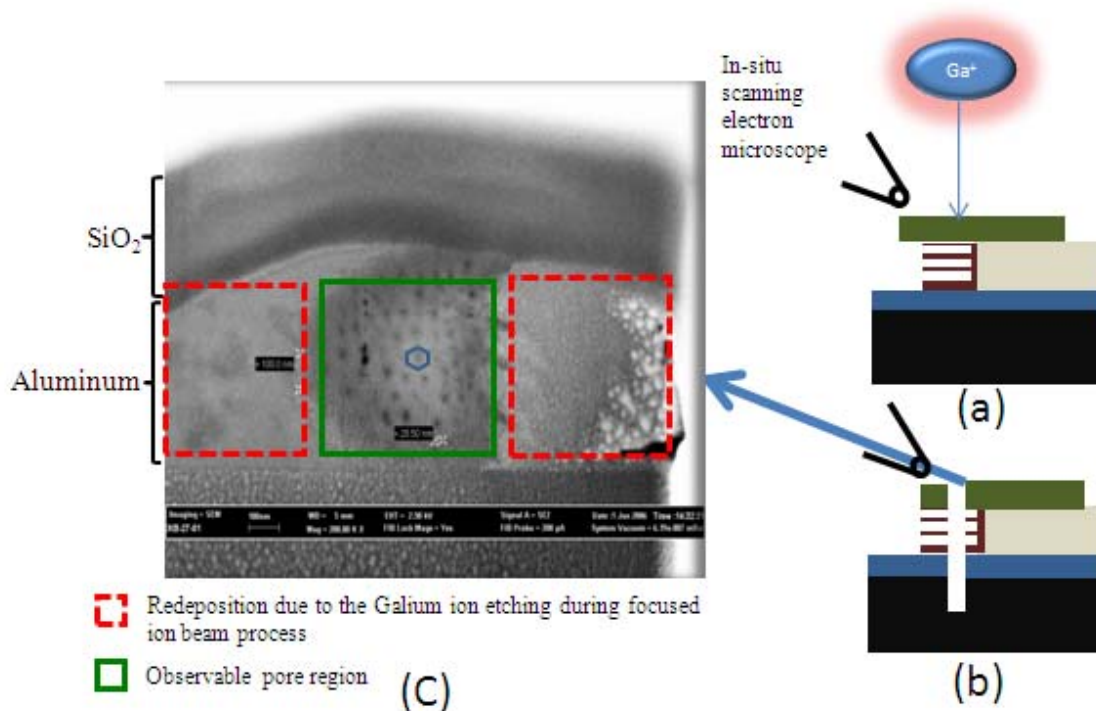


**Figure 3-6:** Schematic of the focused ion beam experiment. (a) Shows the Ga ions etching the membrane and the *in situ* SEM (b) Schematic side view of a membrane after the ion beam etching. Note that the substrate is also etched to some extent in order to get the proper window for view (c) *In situ* SEM image of a membrane after the focused ion beam etching; the well organized pore region is seen clearly in the center part of the picture, whereas re-deposition of ion-sputtered materials blurs the observation on either side

### 3.3.3: PORE DEPTH

We first note that the electric field is the driving force for the pore growth in the alumina films, and the direction of the electric field will significantly influence the nanopore growth direction. Because the ratio of the diameter of cathode to that of the anode (aluminium) is very large in our experimental setup, the electric field observed by the anode is perpendicular to its respective surface. As a consequence, in the nucleation of pores starting randomly (as in the case of vertical template) they propagate perpendicular to their surfaces.

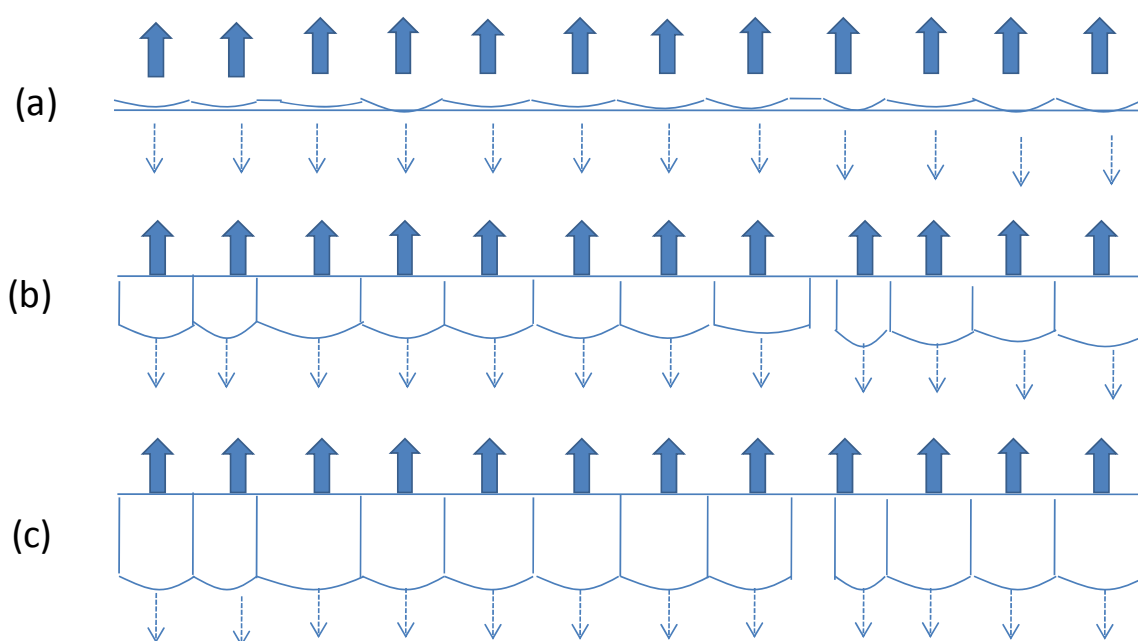


**Figure 3-7:** (a) Pore initiation on the aluminium substrate; (b) and (c) pore growth

The first step of the formation of nanoporous alumina involves the migration of  $\text{Al}^{3+}$  (formed at the metal/metal-oxide interface) and  $\text{O}^{2-}$  (generated at the metal-oxide/solution interface) ions under applied external voltage for the formation of  $\text{Al}_2\text{O}_3$ . The anodic alumina growth on a flat substrate produces straight nanopores because the resistance to the migration of ions ( $\text{Al}^{3+}$ ,  $\text{O}^{2-}$ , and  $\text{OH}^-$ ) is less inside pores that grow along the highest electric field direction (i.e., perpendicular to the surface of the anode, shown as broad arrow in the Figure 3-7). When we increase the anodization time, this electric field drive this pore growth (shown as dotted arrow).

These phenomena are shown in the Figure 3-8 where the capping layer has been removed by RIE and the remaining aluminium at the back was chemically etched by  $\text{HgCl}_2$ . The remaining alumina was left, which gives the rough depth of the pore.

The depth of the pore can be increased by prolonging the anodization time, as the vertical membrane case. But it is very difficult to obtain very short membranes ( $< 100$  nm) in the vertical case, due to its very fast growth rate. But in the lateral case it is found that the growth rate was very slow, due to stress developed by the encapsulation on the four sides of the aluminum restricting the volume expansion and also the area of aluminum exposed to the ions is found to be much less in this case.

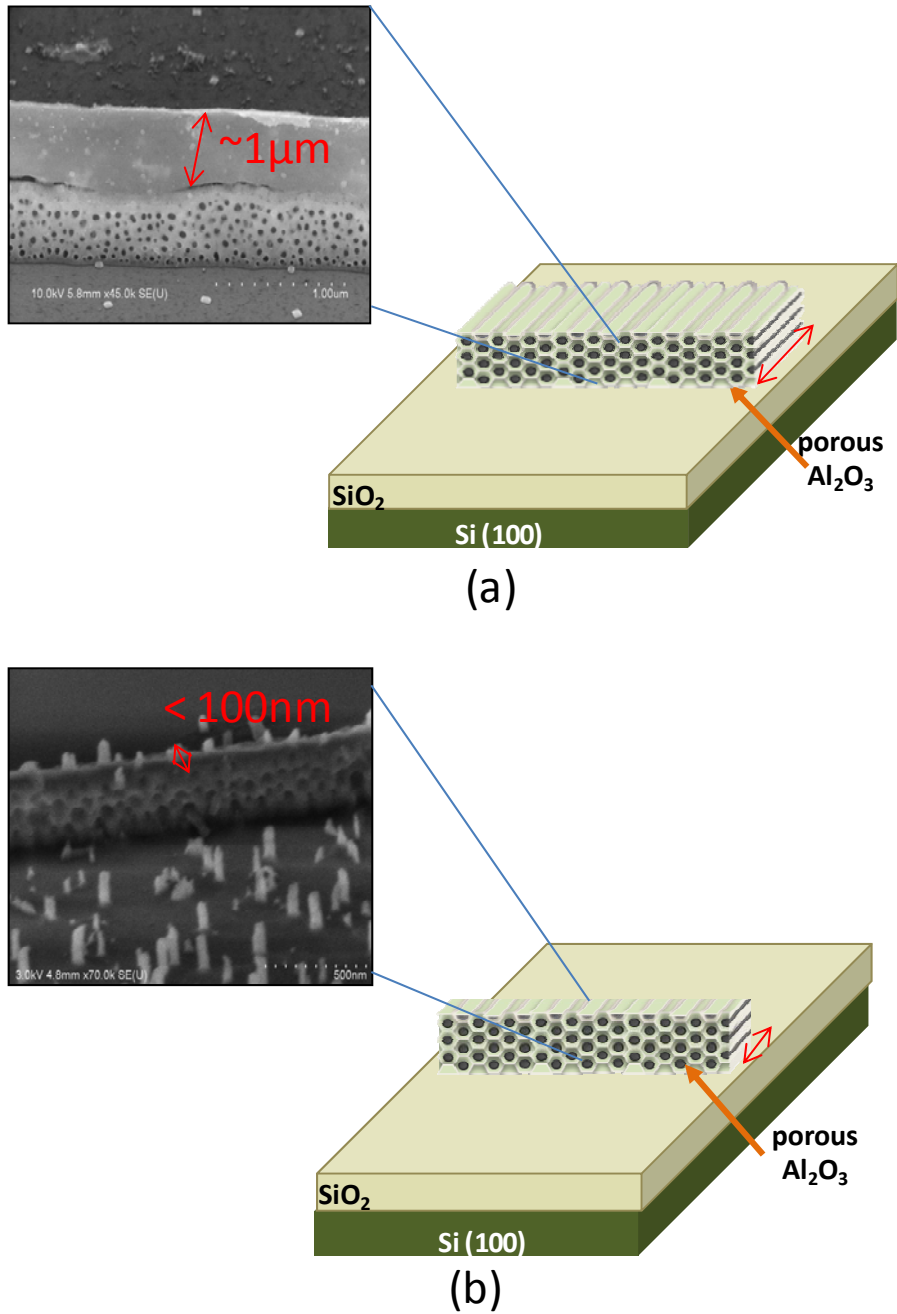


**Figure 3-8:** Pore depth variation with two different membrane length: (a) about 1 micron (b) about 100 nm. SEM pictures on the left hand side corresponding to the right hand side schematic.

### 3.4. SPATIALLY CONSTRAINED ANODIZATION

We have previously mentioned that the pore density can be controlled by the anodization conditions, such as voltage and by changing the nature of acids. By applying a spatial constrained gives another parameter to provide control of the pore density of these PAA templates. It gives excellent control over the number of nano objects grown in these pores.

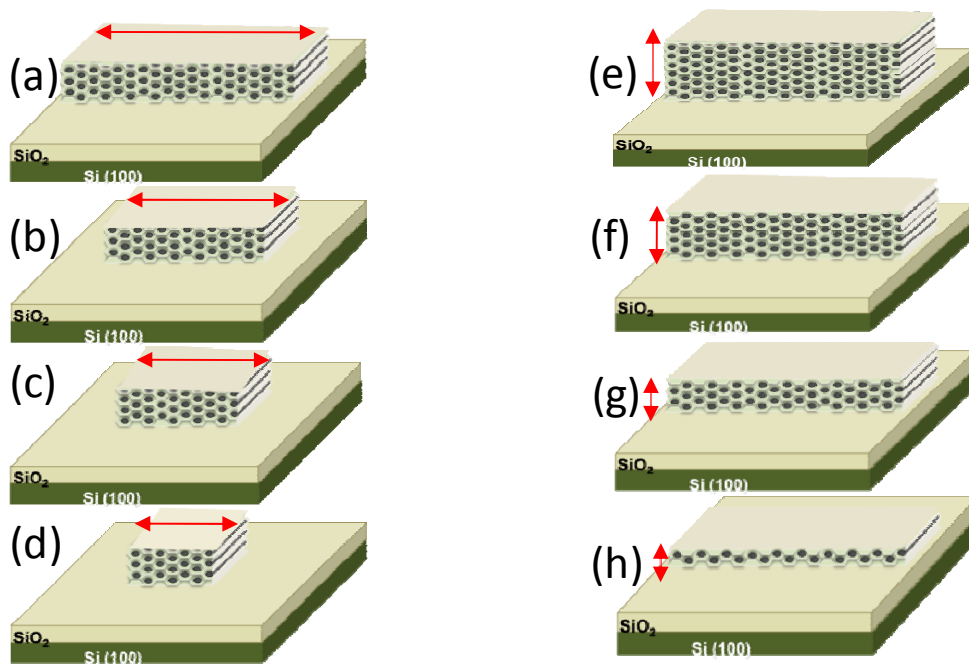
Controlling the pore density was studied by controlling the voltage in different acids such as sulphuric, oxalic and phosphoric acid<sup>128,164</sup>. Nielsch *et al*<sup>127</sup> have shown that different porosity values, such as 9% for 25V in phosphoric acid, 8% for 40V in oxalic acid and 12% for sulphuric acid. They also found that self ordering regimes are only found in these templates for the porosity around 10%.

When the anodization voltage is far from the self ordering regimes, this will lead to cracks and lack of stabilization in the anodization. In order to solve this problem a modified anodizing procedure was used<sup>165,166</sup>. They obtained better control of the pore density by changing the interpore distance precisely. Recently Chen *et al*<sup>167</sup> controlled the pore/cell size very precisely by adding polyethyleneglycol (PEG) as a modulator in the acid. The minimum porosity they reached is about 1.6% which is far less than earlier results in the literature. But they realized this on pure aluminum sheet.

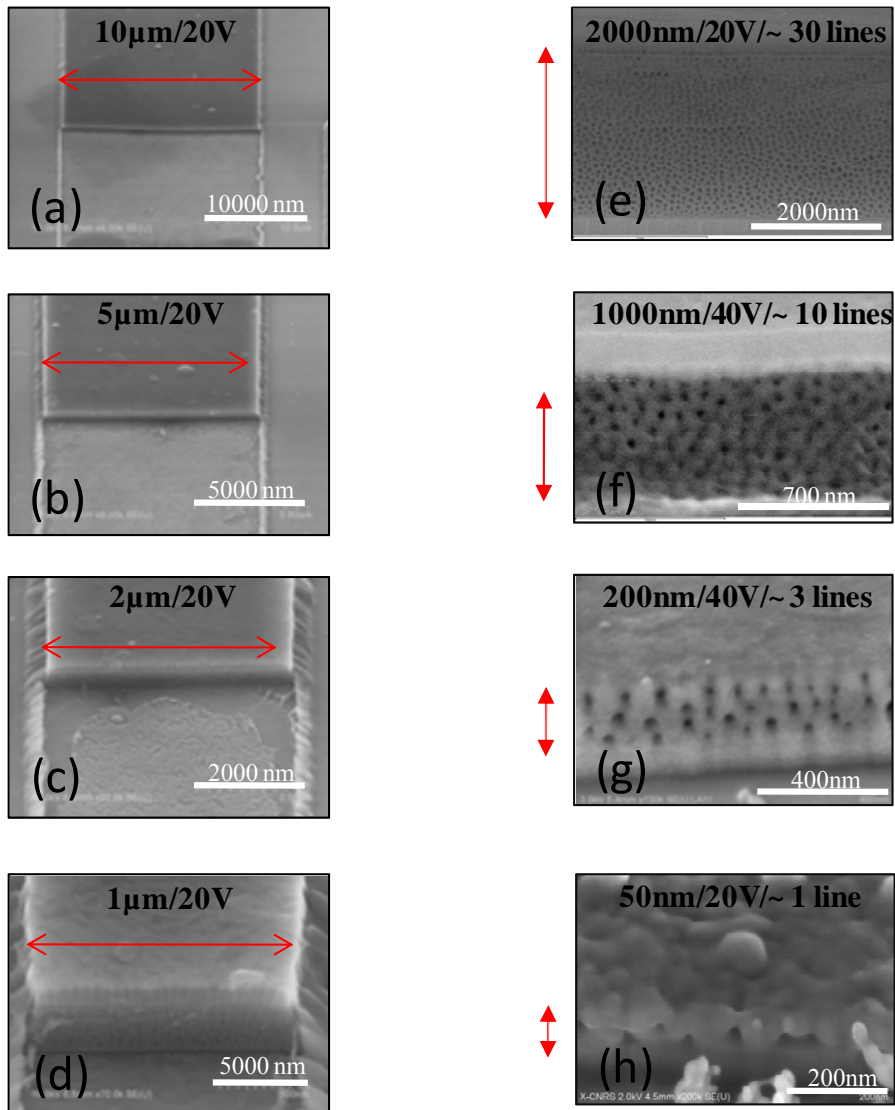
In this work we applied spatial constraint on the aluminum to control the pore density. This has been achieved by controlling the pore diameter and the interpore distance has been varied by changing the anodizing conditions<sup>168</sup> in parallel with varying the thickness of the aluminum and varying the widths of the aluminum stripes by standard lithography (check Annex I for details).

Table 3-3 and Figure 3-9 show that the size of the arrays can be controlled by controlling the thickness of the aluminum layer as well as the width of the aluminum stripe with respect to the cell size obtained at each applied voltage. So we have chosen the acid as well as its temperature and we have used different Al thickness from 2  $\mu\text{m}$  to 50 nm, while applying the appropriate voltage for each anodization. With the 2  $\mu\text{m}$  aluminum thickness, we obtained about 30 lines of pores by controlling the anodization voltage at 20 V. The number of lines in the pore array can be decreased by keeping the thickness constant and increasing the voltage. For example, when the aluminum thickness is about 1 $\mu\text{m}$ , the size of the pore arrays is 10 lines, for 40 V (Figure 3-10(f)). But it can be changed by changing the anodization voltage. For a low Al thickness, say about 200 nm and below, it is difficult to see the pores after the second anodization, since the alumina wall is far away from the SiO<sub>2</sub> edge, following dissolution of the anodic

oxide after the first anodization step. Hence we used RIE to etch the  $\text{SiO}_2$  cap and were able to observe the pore arrays. The thickness of the aluminum used for the one dimensional array (Figure 3-10(h)) is about 50 nm, and the pore diameter is about 20 nm. This is the smallest one dimensional alumina pore array reported up to now. Actually, starting with a 50 nm Al thickness should lead to 2 rows of 20 nm diameter pores. The peculiar boundary conditions due to the lateral and confined oxidation conditions probably modify the anticipated equilibrium for the pore organization. For this study, we did not calculate the porosity, since the inter pore distance varied between the pores. This is probably due to the boundary situation, as just quoted, and also to the limited anodization time. Actually, according to the general theory of pore formation in PAA structures, pores originate at random positions at the beginning of the anodization and when the anodization time increases the order and the depth of the pored increase.



**Figure 3-9:** Schematic of Spatial constrained anodization (a) to (d) Width control; (e) to (h) thickness control



**Figure 3-10:** Spatial constrained anodization (a) to (d) Width control; (e) to (h) thickness control

**Table 3-3:** Variation of the number of pore rows by changing the aluminum thickness and the anodization voltages<sup>a</sup>

<b>sample</b>	<b>Acid</b>	<b>Anodization Voltage (Volts)</b>	<b>Aluminum thickness (nm)</b>	<b>Number of rows</b>
<b>e</b>	Oxalic	20	~2000	~30
<b>f</b>	Oxalic	40	~1000	~10
<b>g</b>	Oxalic	40	~200	~3
<b>h</b>	Oxalic	20	~50	~1

<sup>a</sup> see the corresponding pictures on Figure 3-10

### 3.4.1. MECHANISM OF THE LATERAL PORE GROWTH

The volume expansion during alumina growth generates large compressive stresses in the films. On the planar substrates and planar faces (except at the four edges) of rectangular substrates, the compressive stress generated due to volume expansion during alumina growth is uniform on the whole substrate, because of unrestricted lateral geometry of the planar substrates along the x direction. Having along, y-direction the space is constrained by the thickness of the aluminium.

The general solution is to utilize a mechanically stable encapsulation that withstands the stress during anodization and counteracts the pore formation stress to lead to good pore ordering and directed growth. This gives a better ordering even in the case of only single step anodization.

Where in the case of the vertical anodization, the ordered pores can be obtained by two step anodization.

To compensate for the reduced spatial volume available for alumina growth, we propose that there must be a restructuring nanopore growth mechanism such that some pores grow with the anodization process, whereas others either have stopped growing due to the termination of the pores or have merged with adjacent pores.

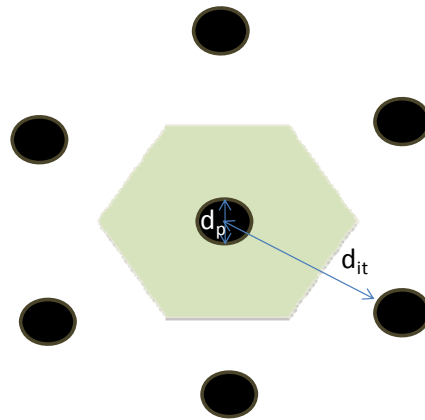


**Figure 3-11:** Diagram of pores in 2D hexagonal ordering

We consider a “cell”, consisting of a pore and its surrounding oxide – nominally the oxide that could be created by processes from that particular pore.

In the case of open vertical anodization the space available is quite infinite. Randone *et al.*<sup>144</sup>, have discussed the possibility that the initial etch sites are much more dispersed leading to fewer pore initiations. They have assumed that once a pore starts to grow, other pores arrange themselves hexagonally around the initial one forming polycrystallites with hexagonal symmetry (shown in Figure 3-11). The cell geometry and the interpore distance will be dependent upon the applied potential

$$d_{it} = \kappa U$$

$$K \approx 2.5 \text{ nm / V}$$

Say  $U = 40 \text{ V}$ ,  $d_{it} = 100 \text{ nm}$  then the pores organized themselves by maintain 100nm in between them.

But when the space is constrained i.e., available area for the starting aluminum is less,

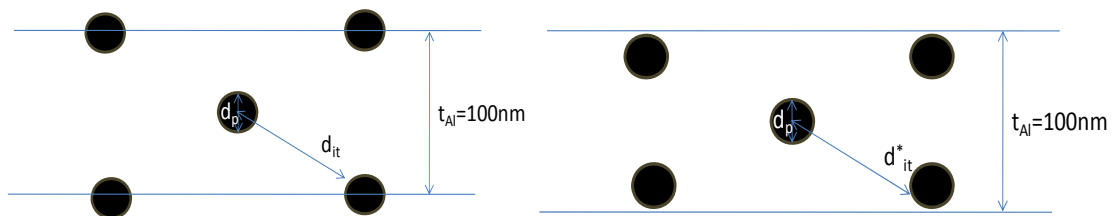


**Figure 3-12:** Modified 2D ordering mechanism due to spatial constrained effect

(e.g in the case shown in Figure 3-12) then the initial etch sites can only be possible within the 100nm aluminum, but laterally can be infinitely large. Due to this restriction in space, the pore initiation along the perpendicular direction was forced to decrease and pores started developing at  $d_{it}^*$  which is smaller than  $d_{it}$ . In some cases semicircular pores has been also found. This is found only when the thickness of the aluminum is very small.

Figure 3-13 shows the SEM images of the one dimensional arrays for two different thicknesses of 100nm and 50nm, where the  $t_{Al}$ ,  $r$ ,  $d_{it}$ ,  $P_i$ ,  $t_b$  are the aluminum thickness, pore radius, inter pore distance, pore length (depth) and barrier layer thickness respectively.

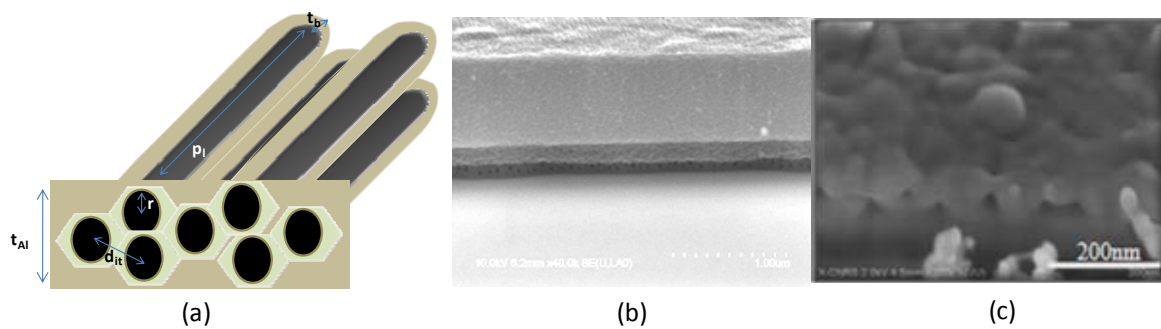


**Figure 3-13:** (a) Schematics of one dimensional array formation, SEM images of one dimensional array for two different thicknesses, (a) 100nm and (b) 50nm.

### 3.4.2. PORE DENSITY CONTROL

Pore density can be varied by deciding the thickness of the aluminum before starting the anodization process. Figure 3-14 shows later PAA structures with different anodization conditions, where the inter pore distance ( $d_{it}$ ) as well as the pore diameter ( $\Phi$ ) can be changed. All the anodization was done by using oxalic acid at  $0^\circ\text{C}$ , but the anodization voltage was varied from 20 V to 40V. Due to the change in the anodization voltage, the interpore distance has been changed, but for Figure 3-14(b) the interpore distance was changed by a chemical pore widening step (done after the anodization)

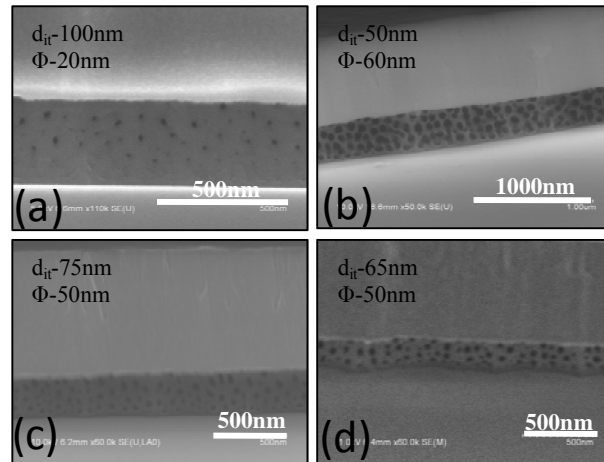


Figure 3-14: Pore variation by controlling anodization conditions

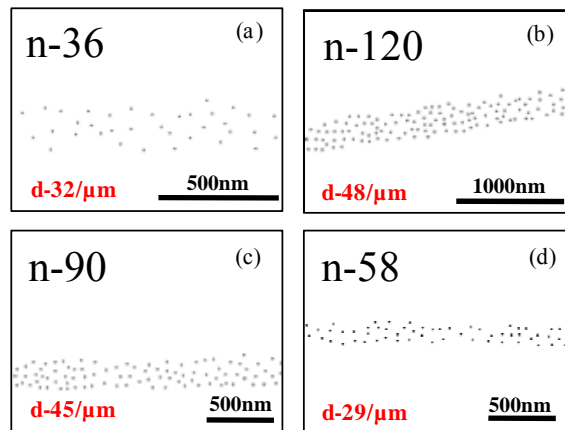
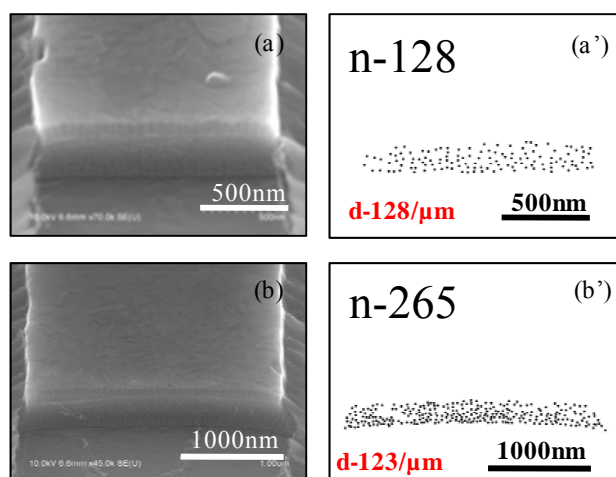


Figure 3-15: Pore density calculation for different anodization conditions

Figure 3-15 is the modified image of Figure 3-14. This was done by using the Image J software. By using the particle analysis option the number of positions of the pores are counted. The dark dots shown in the Figure 3-15 are the location of the pores which matches exactly with the real image shown in Figure 3-14. The number of pores varies from 36 to 120 for almost the same type of sample, just by varying the anodization conditions shown in the inset of the Figure 3-14. Using the appropriate scales the pore density is calculated and transferred to a linear pore density (no. of pore / unit length).



**Figure 3-16:** Pore density control by changing the width of the aluminum stripe on the left side and the respective calculation is found (a') and (b') on the right side

The density control also can be achieved by varying the width of the aluminum stripe as shown in Figure 3-16. The mask we designed has 6 different widths, which gives 6 different widths of aluminum after lithography. Here we have given examples for the two smallest ones ( $2\mu\text{m}$ ,  $1\mu\text{m}$ ), where we can see the pores as well the width of the stripe. For the other larger widths it is difficult to see the pores as well as the width of the stripe on the same picture. Since all the stripes have a common contact, the anodization conditions will be the same for all stripes. So the linear pore density was found to be the same, with a small change due to the process. For a specific condition we obtained about 128 pores per micron, which in gives an indirect density of the nano objects. This value is found to be very high then compared to previous values reported.

### 3.5. CONCLUSION:

This lateral PAA template gives a very good control over the pore density, which indirectly gives the density of the nano objects. So we claim this approach is the best way to organize nano objects like CNTs and SiNWs in a very controlled fashion.



**Chapter 4: CNT and SiNW GROWTH inside  
the lateral porous alumina templates**



---

## 4: CNT AND SiNW GROWTH INSIDE THE LATERAL POROUS ALUMINA TEMPLATES

*This chapter deals with the catalyst deposition and the growth mechanism inside the lateral porous alumina templates. Finally we demonstrate the growth of CNTs and SiNWs inside these lateral porous alumina templates.*

### 4.1: INTRODUCTION

In the early 1990s membrane based nano materials synthesis called “template synthesis” was highly studied by the Charles Martin group. This method entails synthesizing the desired material within the pores of a nanoporous membrane. They started using a PAA template (vertical) for the nano material fabrication, especially in order to prepare tubules and fibrils composed of electronically conductive polymers<sup>169,170</sup>, metals<sup>171,172</sup>, semiconductors<sup>173</sup>, and other materials. They have shown that nanostructures with extraordinarily small diameters can be prepared. In addition, because the pores had monodispersed diameters, analogous monodispersed nanostructures were obtained. Finally, synthesized tubular or fibrillar nanostructures within the pores are freed from the template and can be collected by them.

In 1995 Kyotani *et al* formed ultra fine carbon tubes<sup>174</sup> for the first time by thermal decomposition of propylene in the uniform straight channels of a PAA (vertical) film; they were followed up by Parthasarathy *et al*<sup>175</sup>; who grew graphitized nanotubules by high temperature treatment of polyacrylonitrile (PAN) tubules formed within the pores of an alumina template.

For the case of SiNW growth inside a PAA template (vertical), very little work has been published. Initially polycrystalline SiNWs was grown in PAA templates without any catalyst<sup>176</sup>. In 2002 the Redwing group demonstrated the first growth of crystalline SiNW in vertical PAA templates<sup>177</sup> and further they studied NW diameter control with these PAA templates<sup>178</sup>. Recently by using modified PAA templates, epitaxial growth of Si (100) NWs<sup>179,180,181</sup> has been demonstrated.

In the above mentioned situation, the pore array and hence the array of template-grown CNTs and SiNWs are perpendicular to the surface of the substrate, which complicates (from a topographic point of view) the organization of electrical contacts, as far as three terminal devices are concerned. In integrated circuit fabrication processes, a planar type configuration is preferred for transistor-type devices.

CVD is considered to be best growth technique to control the physical and chemical properties of the CNTs as well as SiNWs. Generally VLS is found to be the growth mechanism in the CVD growth process both for CNTs and SiNWs. A proper choice of catalyst is an important step, since there are several possible catalysts already reported in the literature as shown in Figure 4-1, where the catalysts for the SiNWs and CNTs are marked. It is also found that there are some catalysts which are common for the growth of both CNTs and SiNW. Mostly the catalysts are found among the transition metals, which can be deposited inside the nanopores by using an electrochemical process.

By taking into account the advantages of the template based approach, especially lateral templates, and the CVD based growth, we developed CNT and SiNW growth inside lateral templates for planar type device applications. Growth inside lateral PAA templates by using CVD was not seen in the literature, so we consider ourselves as pioneers in this method. But still there is lot of room for a detailed study on growth of lateral porous alumina templates and the growth of nano-objects inside these templates.

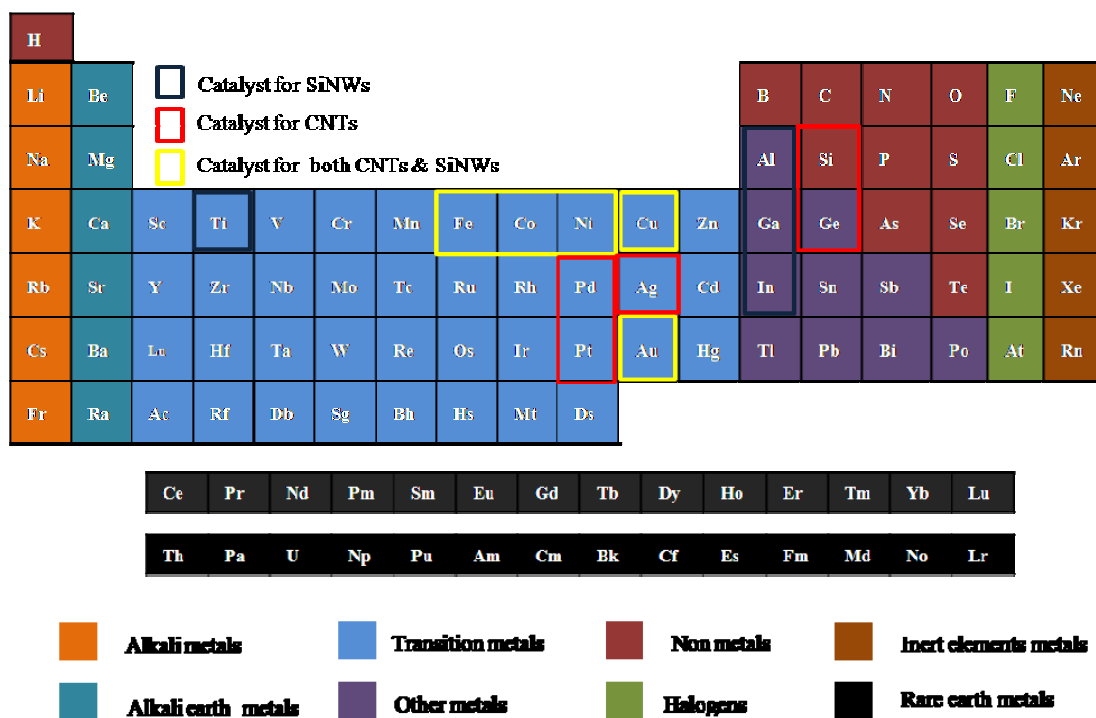


Figure 4-1: Catalyst map in the periodic table

## 4.2: CATALYST FOR THE CNT GROWTH

It has been established that the transition metal catalysts (~e.g., Fe, Co, Ni, or their alloys) play a key role in the growth of high quality, long CNTs. The catalyst particles, which are typically between 1 and 50 nm in diameter, can be on a substrate<sup>64</sup> or can “float” in a gas<sup>182</sup>. The role of these particles in the growth mechanism is described in the widely accepted VLS model<sup>183,48</sup>, which was first proposed to explain the growth of carbon nanofibers in 1972<sup>184</sup>. According to this model, carbon that is evaporated from graphite or decomposed from carbon-rich gases (~e.g., CO, C<sub>6</sub>H<sub>6</sub>, and C<sub>2</sub>H<sub>2</sub>) dissolves into the liquid metal clusters, and when the metal-carbide clusters are supersaturated in carbon, carbon islands precipitate on the cluster surface and nucleate as CNTs. Although the VLS model provides a simple explanation that captures the essence of CNT growth, it does not include atomistic details such as the mechanism of graphitic cap nucleation on the cluster surface, how the open end of the nanotube is maintained during CNT growth, how defects that may form in the CNT structure are healed, and what determines the diameter and chirality of the CNT.

But later a group of scientists from France and Belgium suggested a common growth mechanism based on a VLS model with quantum-molecular-dynamics simulations supporting a root growth mechanism where carbon atoms are incorporated into the tube base by a diffusion-segregation process<sup>185</sup>.

Recently, however, gold, silver, and copper have been reported to produce CNTs<sup>186,187,188</sup>. This implies that hydrocarbon-molecule decomposition and graphite formation ability are not essential and leads to a new interpretation of the role of catalyst particle in CNT growth, (i.e.) only a nanoscale curvature would be necessary to grow CNTs if carbon atoms are supplied to the nanocurvature. The Homma group gave further experimental evidence, supporting the above hypotheses by showing CNT formation on semiconductor nanoparticles of SiC, Ge, and Si, with which no catalytic functions were expected. The grown CNTs with these semiconducting nanoparticles are SWCNTs or double-walled (DWCNTs), with a diameter of 5 nm or smaller<sup>189</sup>. So the choice for the catalyst becomes wider.

### 4.2.1: CATALYST PARTICLE SIZE

Several studies have been conducted to determine the dependence of the CNT diameter on the catalyst particle size. Even in the first publication by Dai *et al*<sup>190</sup> about CVD growth, a close correlation between the SWCNT diameter and the catalyst particle was noticed. Later, the CNT diameter dependence with the catalyst particle size has been largely investigated<sup>191,192</sup>. For instance, iron nanoparticles with average

number diameters of 3, 9 and 13 nm, yielded CNTs with wall diameters of 3, 7 and 12 nm respectively as reported by Cheung *et al.* The CNTs produced with the smallest catalyst particles ( $\leq 1$  nm) were primarily SWCNTs with few DWCNTs. With larger catalyst particles, the number of DWCNTs and thin MWCNTs increased in the growth product. This finding has been the motivation for decreasing the catalyst particle size close to the 1–2 nm scale in order to produce the most desirable CNT product, i.e. SWCNTs.

Determining the particle size distribution before heating, in order to get the synthesis conditions gives only a rough estimate of catalyst particle size during the SWCNT nucleation and growth. Evolution of size distribution of the metal particles during the CNT synthesis is inevitable due to the increased temperature required to accelerate the decomposition of the carbon precursor molecules on the catalyst surface. When metal particles are heated, several different phenomena occur. Catalyst particles may collide and aggregate due to surface diffusion. Subsequent sintering of particles has been observed to increase the average particle size (e.g. by Alvarez *et al.*<sup>193</sup>). Simultaneous evaporation of particles reduces the number concentration and modifies the size distribution even further. In our template based growth approach, catalyst diffusion is completely blocked by the PAA structure and by adjusting the pore diameter by anodization conditions, the catalyst diameter can be adjusted in a controlled manner.

### 4.2.2: CHEMICAL COMPOSITION OF THE CATALYST

*In situ* measurements addressing the changes in chemical composition of the catalyst can elucidate the mechanisms taking place during CNT growth<sup>194</sup>. The basic conclusion is that, when starting from an oxide catalyst, reduction of the metal oxide takes place during decomposition of the carbon precursor compound. As a result, a metallic particle forms through intermediate oxide states. Upon carbon dissolution, a metal– carbon solid solution or metal carbide is formed. Subsequent segregation results in the formation of graphitic carbon and metal particles. Table 4-1 shows the physical and chemical properties of the various metals with the carbon. The properties of the iron, cobalt and the nickel are found to be nearly the same, especially the carbon diffusion coefficient in these metals. From this it is clear that these three metals are the better choice for the catalyst.

**Table 4-1:** Physical and chemical properties of selected transition metals with the carbon

<b>Macroscopic property</b>	<b>Iron</b>	<b>Cobalt</b>	<b>Nickel</b>	<b>Palladium</b>	<b>Copper</b>	<b>Molybdenum</b>
<b>Surface tension at 20°C (Nm<sup>-1</sup>)</b>	1.95	2.1	1.86	2.1	1.75	2.2
<b>Equilibrium vapour pressure (at t= 1216°C) (Pa)</b>	5.5 x 10 <sup>-3</sup>	4.7 x 10 <sup>-3</sup>	4.0 x 10 <sup>-3</sup>	2.1 x 10 <sup>-3</sup>	7.1 x 10 <sup>-3</sup>	7.6 x 10 <sup>-3</sup>
<b>Carbon solubility (at%) at T<sub>melt</sub></b>	20.2	13.9	10.7	~ 5	2x10 <sup>-4</sup>	Upto 60-70%
<b>Carbon diffusion coefficient in metal(m<sup>2</sup>s<sup>-1</sup>) (at t=1000°C)</b>	1.5 x 10 <sup>-11</sup>	1 x 10 <sup>-11</sup>	2 x 10 <sup>-11</sup>	6 x 10 <sup>-11</sup>	NA	NA

NA= data not available

It is also found that Fe, Co, and Ni, commonly used to catalyze SWNT growth, have larger adhesion strengths to SWNTs than Cu, Pd, and Au and are therefore likely to be more efficient for supporting growth<sup>195</sup>. Between the first three, Fe and Co have almost the same adhesion energy and greater than that of the Ni adhesion energy with the carbon atom<sup>196</sup>.

### 4.3: CATALYSTS FOR SiNW GROWTH

Catalyst assisted 1D crystal growth by VLS<sup>48,197,198</sup> is a widely demonstrated method for growing semiconductor nanowires. Nevertheless, a complete understanding and control of all the mechanisms

governing precise and reproducible whisker growth with defined characteristics is still lacking. Until now, the vast majority of the work reported in literature mention Au as the metal catalyst, which appears to be a sort of universal choice for growing the most diverse types of semiconductor nanowhiskers (e.g. Si, SiGe<sup>199</sup>, Ge<sup>200</sup> and III-V compounds<sup>201</sup>). In the case of III-V and II-VI compound semiconductors, nanowire growth at moderated temperatures has been demonstrated from a metal catalyst that is also one of the compound elements<sup>202</sup>. A few sporadic studies have assessed the feasibility for VLS growth of Si nanowhiskers mediated by Ga<sup>203</sup>, Cu<sup>204</sup>, and Vapour-Solid-Solid (VSS) growth with Al<sup>205</sup> and Ti<sup>206</sup>. All these studies reported a lower efficiency when compared to Au catalyzed VLS growth. Early growth trials using In catalysts with CVD technique were not successful. But it was demonstrated recently by using PECVD on an ITO substrate<sup>207</sup>.

Ultimately the eligibility of a given metal catalyst is the thermodynamic behaviour of the metal-Semiconductor alloy, together with the kinetic factors affecting the activation of the catalyst particle for VLS. The VLS growth of nanowires by CVD can be broken down into several steps: precursor gas transport to the catalyst particle, gas dissociation at the particle site, sticking and diffusion in the liquid alloy of Si with the metal particle, super saturation and (1D) precipitation of the Si crystal. Au nanoparticles play a key catalyst role in almost all of the above mentioned steps of VLS growth by CVD. In particular, Au is also an efficient chemical catalyst for silane dehydrogenation/dissociation<sup>208</sup>. This property is common to a few metals<sup>209</sup>, however it is not strictly necessary for VLS growth. Nanowire growth always competes with a parasitic deposition of amorphous, a-Si. In this case the requirements for a selective Si deposition become stringent, and a prompt activation of the catalyst nanoparticle for VLS growth is crucial.

#### 4.4: PAA TEMPLATES FOR NANOMATERIALS FABRICATION

In general, the use of the PAA templates for nanomaterials fabrication can be carried out in two ways

1. The anodic film with a remaining aluminum substrate can be used directly for the electrodeposition of metals
2. It can be separated from the aluminum base and further processed into a freestanding membrane with open pores at the top and bottom of the membrane.

Liang *et al*<sup>210</sup> have reported details of the most widespread methods of nanoarrays fabrication employing PAA template.

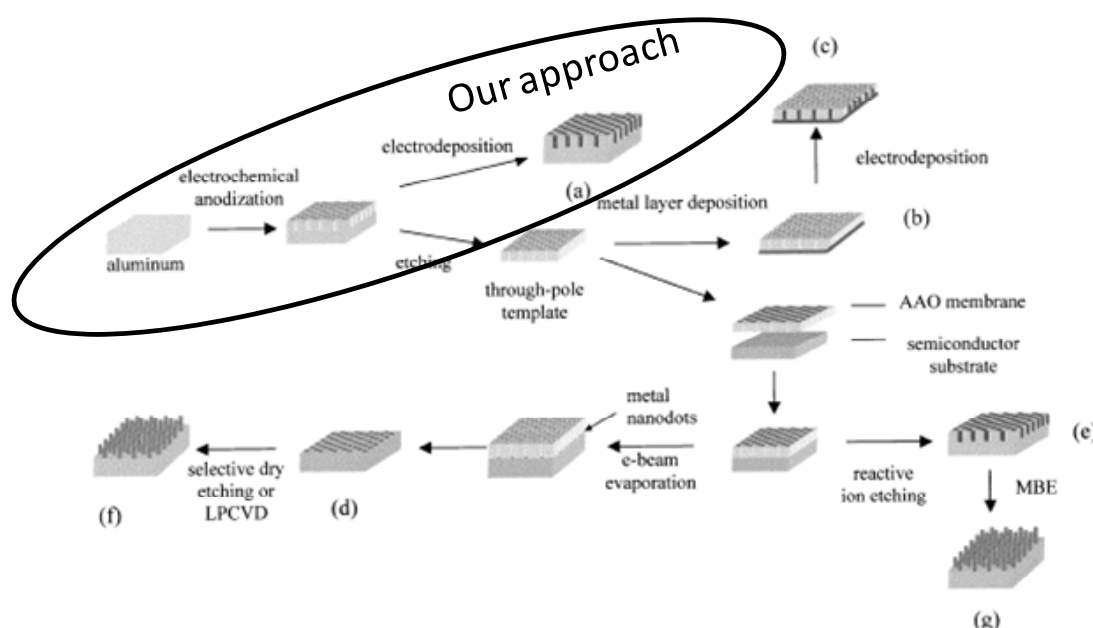


**Figure 4-2:** Schematic of the fabrication of lateral two-dimensional superlattice structures: (a) Metal nanowire arrays electrodeposited in AAO (Anodic Alumina Oxide = PAA) template. (b) Through-pole AAO template with metal film deposited on one surface. (c) Metal nanowire arrays electrodeposited in through-pole AAO template. (d) A metal nanodot array deposited on semiconductor substrate. (e) A substrate with nanopore array. (f) An ordered semiconductor nanopillar/nanodot array. (g) A heterostructure quantum dot array by MBE on prepatterned substrate (Liang *et al.*<sup>210</sup>)

By using the PAA membranes as templates, a number of approaches for fabricating a variety of nanosuperstructures have been developed<sup>107,211,212,213,214,215,216,217,218,219,220,221,169,222</sup>. The process flow diagram in Figure 4-2 illustrates some of the possible ways of creating nanostructured arrays.

- Deposition in PAA with intact barrier layer(a)
- Deposition in open pore template (b) and (c)
- Template-assisted evaporation or etch alternatives
  - “positive” transfer - (d) and (f)
  - “negative” transfer - (e) and (g)

We have chosen the “electrodeposition in intact barrier approach” for our process.

In general, ac electrodeposition is found to be a more appropriate method to fill the PAA templates. But in reality it is a complicated process, as evidenced by the reported variation in the quality of pore-filling (the percentage of pores with material deposited inside and the variation in the amount of material deposited in

each pore) as a function of deposition conditions, including electrolyte concentration, composition, and temperature, and upon deposition voltage, frequency, waveform (sine, square, and triangle), pulse polarity, and sequence. Moreover, the optimal deposition conditions appear to depend on the metal or deposited compound. This observed complexity is not surprising; it comes from the chemical and structural nature of the porous structure.

After anodization, the PAA structure ends with  $\text{Al}_2\text{O}_3$  at the bottom of the pore; this is called the barrier layer. The observed slight variation in the barrier layer thickness from one pore to the next one is mainly due to local defects/impurities in the Al material. Thus, the resistance during electrodeposition could vary depending on the pores, which influences the deposition behavior, since electrodeposition preferably occurs in those pores exhibiting a thinner (*i.e.*, a less resistive) barrier layer<sup>223,224</sup>. There are several ways to penetrate or to thin or to remove this barrier layer<sup>225,226,227,228</sup>. We came up with a precisely controlled “voltage decrease method” at the end of the anodization process for thinning down the barrier layer<sup>229</sup>. It also stabilizes the variation of the barrier layer thickness over the sample to obtain a uniform thickness. Figure 4-3 shows the detailed picture of the pore structure in the vertical PAA template with and without barrier layer after the thinning process. Uniform catalyst deposition can be seen at the bottom of the pore after the thinning process. This was exactly adapted to the lateral PAA templates.

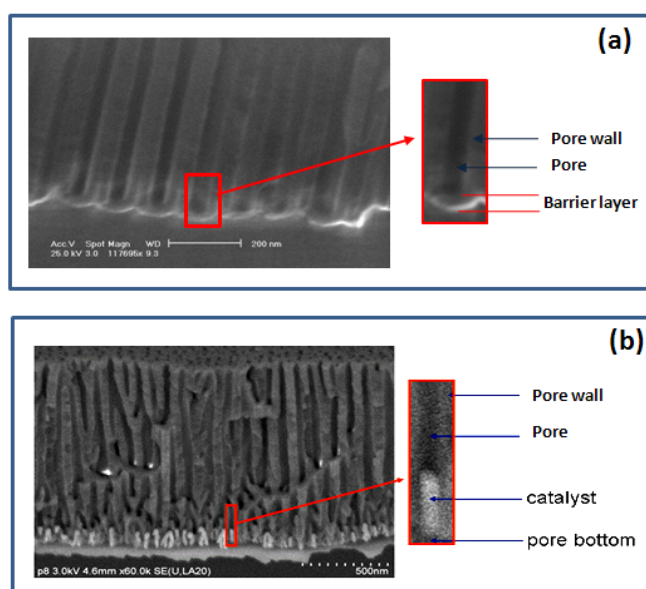


**Figure 4-3:** (a) shows the pore structure with barrier layer at the bottom of the pore, (b) shows the pore structure without barrier layer (or very thin barrier layer) at the bottom of the pore with the catalyst after electrodeposition

The catalyst particles were then electrodeposited at the bottom of the pores, using 0.5M copper sulfate ( $\text{CuSO}_4$ ) for SiNW growth and cobalt sulfate ( $\text{CoSO}_4$ ) for CNT growth. The sulfate solutions were buffered with boric acid ( $\text{H}_3\text{BO}_3$ ) and the pH was around 3.8. Cobalt or Copper particles were electrochemically deposited at the bottom of the pores using  $14V_{\text{RMS}}$  at 100 Hz for 30 s in an electrolyte consisting 240 g/L of  $\text{CoSO}_4 \cdot 7\text{H}_2\text{O}$  (or  $\text{CuSO}_4 \cdot 7\text{H}_2\text{O}$ ), with 40 g/L of  $\text{H}_3\text{BO}_3$ . The electrical configuration used in these experiments is same as that of the anodization, except the electrolyte (see the figure 1 of chapter 3).

### 4.5: GROWTH OF CNT AND SiNW INSIDE PAA TEMPLATE

#### 4.5.1: MECHANISM OF CNT & NW GROWTH INSIDE PAA TEMPLATE

Synthesis of CNTs/NWs in a PAA template is considered to be a complex process which involves the competitive catalytic carbon deposition between the catalyst particles electrodeposited at the bottom of the pores and the PAA template itself. It is known that crystalline  $\gamma$  or  $\gamma'$ - $\text{Al}_2\text{O}_3$ <sup>107,230</sup> and chemically prepared  $\gamma$ - $\text{Al}_2\text{O}_3$ <sup>231,232</sup> exert significantly higher dehydrative catalytic activity. In our case, although the metal catalyst is much more active for  $\text{C}_2\text{H}_2$  decomposition, PAA also exhibits some catalytic activity. In the presence of catalyst particles at the bottom of the pores, however, the coexistence of amorphous carbon deposits and well-graphitized MWNTs was observed. It shows that the catalyst particles exhibit predominant catalytic activity and initiate CNT growth to form short MWNTs at the initial stage of the reaction, but they are deactivated by the deposition of carbon on the active sites as the reaction proceeds. The physical mechanism of CNT growth by the catalytic decomposition of gas species has been postulated as either base or tip growth. The strength of the metal-support interaction can play an important role in determining the type of growth.

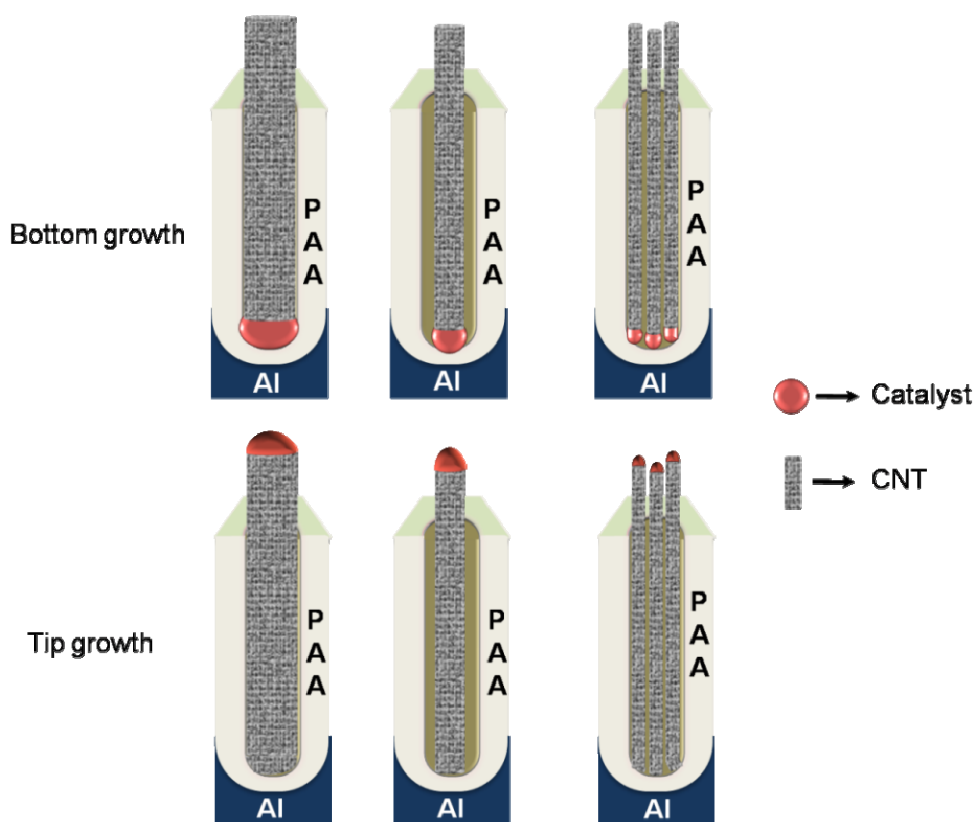


**Figure 4-4:** Bottom growth and Tip growth mechanism for CNT growth in PAA

At this stage an explanation of the CNT growth mechanism within the PAA templates must remain speculative; however, this situation is complicated by the catalytic alumina. Determining the exact nature of the growth process will require further detailed quantitative study. We have shown the two possible modes of growth in Figure 4-4 in different situation of the catalyst at the bottom of the pore. It is obvious that the bottom growth process will be difficult, due to the problem of diffusion of the gas once the CNT growth initiated, which leaves no space for the gases.

In the case of hydrocarbon (source gas) decomposition without  $H_2$ , carbon deposits faithfully follow the geometry of a PAA template. Therefore, it will be possible to make particular shapes of open tip carbon tubes, such as branched<sup>233</sup>, Y-junctioned<sup>223</sup>, and linearly joined carbon tubes<sup>234</sup>. It should be noted that carbon tubes formed by this method have poor crystallinity unless the temperature is sufficiently high. On the contrary, when  $H_2$  is added in the reacting gas mixture,  $H_2$  is believed to have a “cleaning effect” which keeps the active sites of catalysts devoid of encapsulating carbon that would deactivate them<sup>235</sup>.

Therefore, it enables the catalyst particles to promote the  $C_2H_2$  decomposition throughout the growth process and to form CNTs whose length extends to several  $\mu m$ .

Two different configurations of catalyst in PAA templates and corresponding CNT growth are schematically depicted in Figure 4-5(a) and (d). Metal catalyst fills the entire space of a pore bottom (shown in Figure 4-5(a)); i.e the diameter of a catalyst particle is the same as the pore. In this case, the morphology and crystallinity of CNTs depend strongly on the competition of two competing mechanisms: 1) catalytic carbon deposition on the metal catalyst particles and 2) on the PAA template itself. The carbon deposit on the pore wall can easily block the growth of a CNT from the bottom, ending frequently with dead CNT (Figure 4-5(b)). Figure 4-5(d) shows the situation when the size of a metal catalyst is much smaller than the diameter of a pore. In this case the carbon deposition on the pore wall does not block the growth of CNTs from the metal catalyst particles. Hydrogen at the growth temperature etches the amorphous carbon deposition (a-C) on the pore surface, resulting in overgrown CNTs (Figure 4-5(c) and (f)).

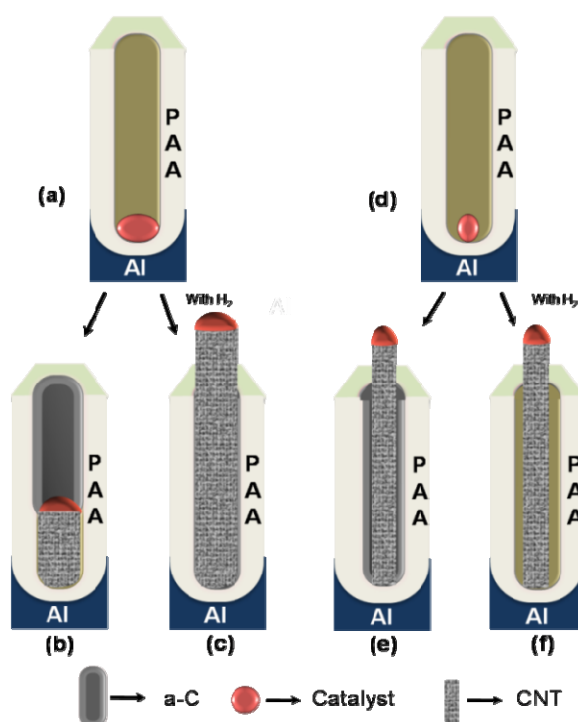


**Figure 4-5:** Schematic of CNT growth in PAA Template: (a) with catalyst which has filled the entire pore diameter at the bottom and (d) with catalyst which has a smaller diameter than that of PAA template, (b) and (e) growth without  $H_2$ ; (c) and (f) shows the role of  $H_2$  during the growth.

With the knowledge and a very good control of the electrodeposition process it is possible to achieve catalyst of smaller size than that of the pore bottom even with the larger pores (Figure 4-5d). This can be applied to obtain nano objects with small diameter, like SWCNTs and SiNWs as well.

The above mentioned growth mechanism can be applied to the SiNW case also, but in the case of the SiNW growth mode, it always leads to tip based growth.

### 4.6: CNT/SiNW GROWTH INSIDE LATERAL PAA TEMPLATE

#### 4.6.1: GROWTH TECHNIQUE

We used a modified CVD reactor for this study; Figure 4-6 shows the schematics of the modified CVD system. A hot tungsten filament was placed 150 mm upstream of the sample holder, in order to pre-decompose the gas before it reaches the substrate. The filament was thermally isolated by a boron nitride cylinder, and it was operated at  $\sim 1800$  °C. The temperature was measured with an optical pyrometer. Since the substrate heating (including the possible effect of the tungsten filament) was automatically adjusted by a thermocouple situated at the same position as the substrate, the temperature was correctly controlled at the desired value during the growth. The samples were first placed at the end of the quartz tube holder, which is almost at room temperature, and rapidly pushed in the center region of the quartz tube using a stainless steel rod, once the temperature has been stabilized at the desired value and once the H $\cdot$  had been activated by switching-on the corresponding tungsten filament (this was done only for the SiNW growth). But for the CNT growth, the hot filament was always in the off mode. The gas (SiH $_4$  or C $_2$ H $_2$ ) is introduced via the inlet shown on the right.

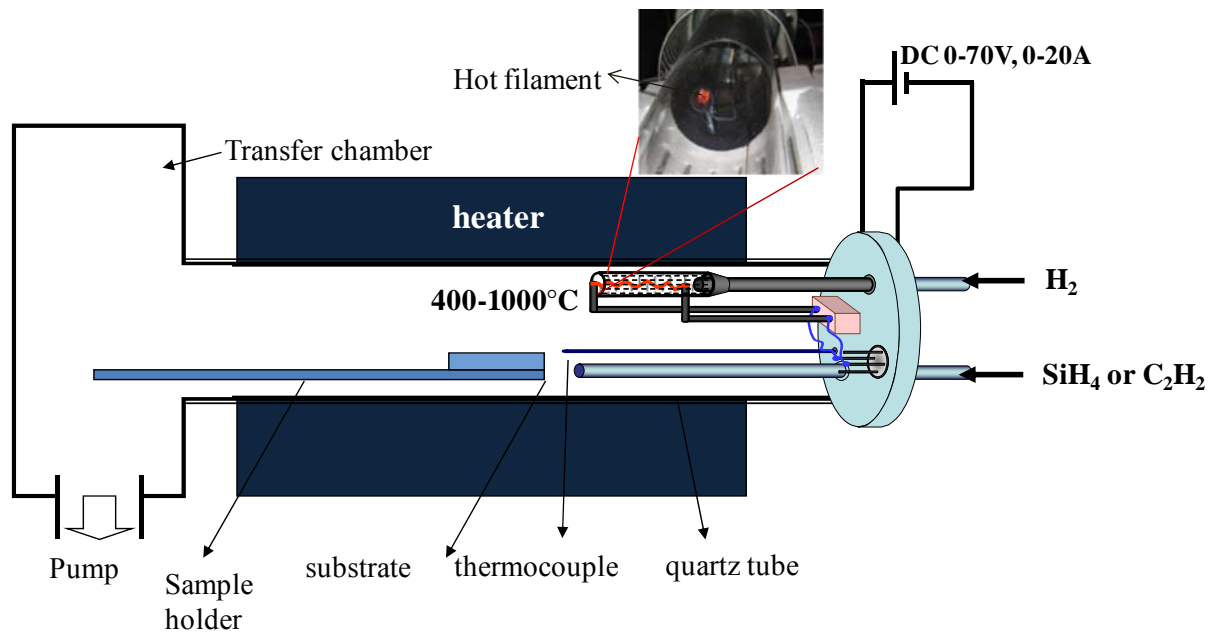


**Figure 4-6 :** Chemical vapour deposition reactor

Process steps for growth inside the PAA are shown in Figure 4-7. After the preparation of the membrane and the electrodeposition of the catalysts, the samples were loaded in a CVD reactor and heated under a  $H_2$  atmosphere (15 mbar) for 15 min, in order to stabilize the membranes and the catalyst particles.

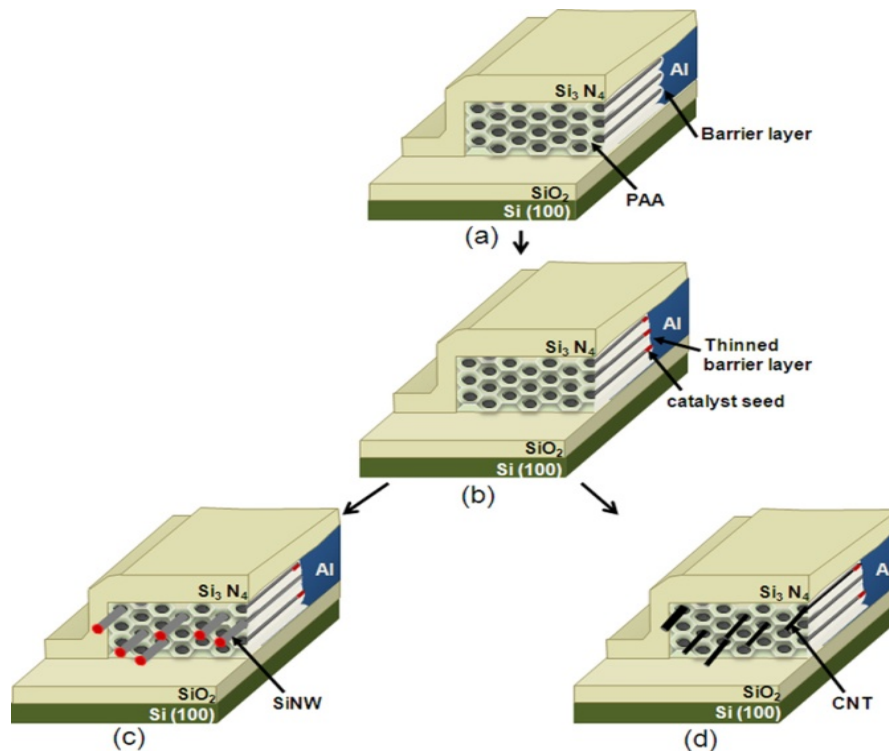


**Figure 4-7:** Growth principle of CNTs and SiNWs in lateral porous alumina templates (a) Lateral porous alumina template with the barrier layer (b) Electrodeposited catalyst seeds at the bottom of the pores, after thinning the barrier layer (c) SiNW growth with copper catalysts (tip growth) (d) CNT growth with cobalt catalysts (root /tip growth)

#### 4.6.2: SiNW

Si NW growth (shown in

Table 4-3) was done by using the conditions shown in the Table 4-2. These conditions are optimized earlier on the plane substrate and just the best condition was chosen for this study. However, in order to avoid parasitic deposition of amorphous or ill-crystallized Si on the PAA itself, atomic hydrogen ( $H\cdot$ ) is used. This  $H\cdot$  can be generated by passing molecular hydrogen gas through the hot tungsten filament in the reactor and it provides high etching rates for the a-Si with a high selectivity against metal and oxides<sup>236</sup>. The typical growth time was set to 10 min. The effect of the  $H\cdot$  is shown in

Table 4-3, where the pores are completely clogged (sample 1) when the hot filament is off during the growth and pores are not clogged (sample 2) when the filament is on.

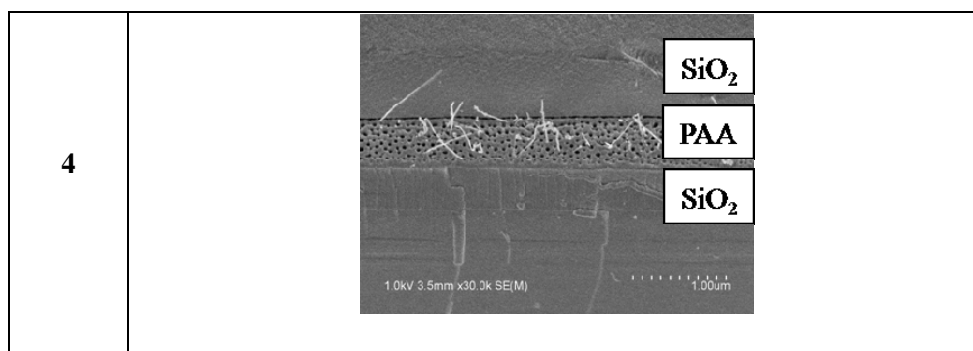
Table 4-2 : Conditions for the SiNW growth

1	Electrodeposition	<u>Voltage</u>	<u>frequency</u>	<u>Time</u>		
	(Cu)	6V	100 Hz	30 s		
	Growth	<u>Temperature</u>	<u>Gas</u>	<u>Working pressure</u>	<u>Time</u>	<u>Filament power</u>
		550°C	SiH <sub>4</sub> -2.5 sccm, H <sub>2</sub> -97.5 sccm	10 mbar	10 min	0W
2	Electrodeposition	<u>Voltage</u>	<u>frequency</u>	<u>Time</u>		
		6V	100 Hz	30 s		
	Growth	<u>Temperature</u>	<u>Gas</u>	<u>Working pressure</u>	<u>Time</u>	<u>Filament power</u>
		550°C	SiH <sub>4</sub> -2.5 sccm, H <sub>2</sub> -97.5 sccm	10 mbar	10 min	150W
3	Electrodeposition	<u>Voltage</u>	<u>frequency</u>	<u>Time</u>		
		6V	100 Hz	90 s		
	Growth	<u>Temperature</u>	<u>Gas</u>	<u>Working pressure</u>	<u>Time</u>	<u>Filament power</u>
		550°C	SiH <sub>4</sub> -2.5 sccm, H <sub>2</sub> -97.5 sccm	10 mbar	10 min	150W
4	Electrodeposition	<u>Voltage</u>	<u>frequency</u>	<u>Time</u>		
		6V	100 Hz	15 s		

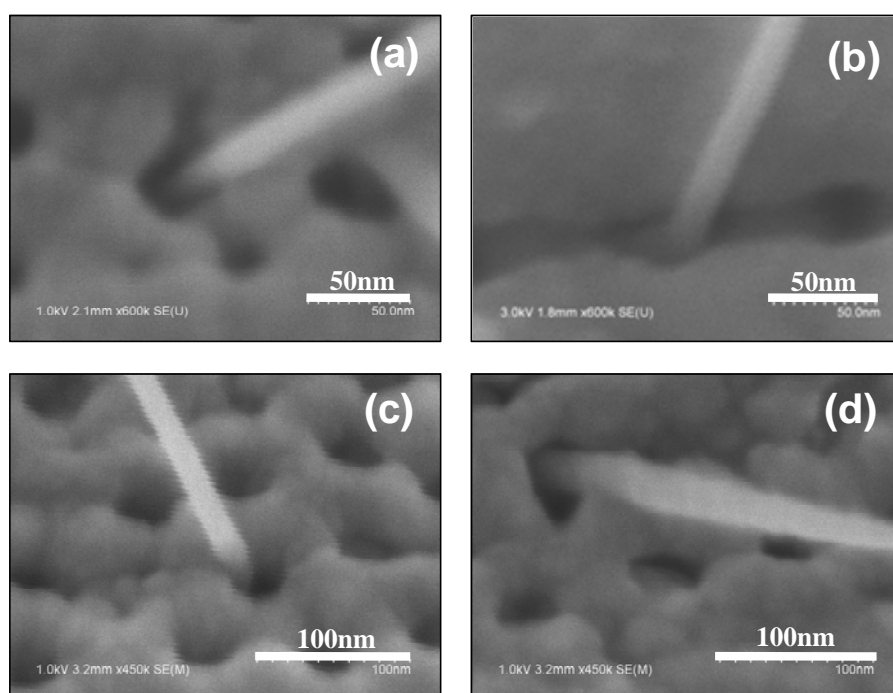
Growth	<u>Temperature</u>	<u>Gas</u>	<u>Working pressure</u>	<u>Time</u>	<u>Filament power</u>
	550°C	SiH <sub>4</sub> -2.5 sccm, H <sub>2</sub> -97.5 sccm	10 mbar	10 min	150W

Table 4-3: SiNW growth inside lateral PAA templates

Sample	
1	
2	
3	



The red arrow indicates clogged pores, blue arrow indicates partially filled or empty pores and the brown arrows indicate pores with SiNW. For samples 3 and 4 the variation in the density of the wire for different electrodeposition conditions is clearly seen. In the case of sample 3 the catalyst deposition was done for a prolonged time, so the density of the SiNWs was really high. But for sample 4 the catalyst deposition was done for a very short time which gives a lesser density of NWs. We understood from these two conditions that the catalyst filling in the pore also plays a crucial role in the NWs density.



**Figure 4-8:** SiNW growth in different conditions shows the one NW per pore

It is found that almost in all cases one pore contains just one NW (Figure 4-8). This may be due to the fact that catalyst is not broken. The diameter of the SiNW is found to be uniform in all the cases and it is slightly less than that of the pore diameter (i.e.  $\sim 20\text{nm}$ ).

### 4.6.3: CNT

For the growth of CNTs, we use the conditions shown in the Table 4-4. Here,  $\text{H}_2\text{O}$  is used instead of  $\text{H}_2$  for removing amorphous carbon<sup>237,238</sup>. Water vapor is found to etch away any carbon precipitate covering the metal catalyst, based primarily on the chemical reaction  $\text{C}(\text{solid}) + \text{H}_2\text{O}(\text{gas}) \rightarrow \text{CO}(\text{gas}) + \text{H}_2(\text{gas})$ , thus maintaining the catalytic activity. This oxidative etching is strongly dependent on the CVD temperature, and the balance between the etching and carbon precipitation is important for effective nanotube growth.

The typical growth time was 15 min. Table 4-5 clearly shows some CNTs emerging from the pores. It is well known that the VLS-type mechanism produces CNTs exhibiting diameters strongly correlated with the size of catalyst particles<sup>239,240</sup>. Hence, the CNTs emerging from the pores are certainly not single walled, because the electrodeposited Co catalysts (whose diameters are shaped by those of the pores) exhibit large diameters.

In some case, the catalyst is deposited for a prolonged time and when the growth is performed on these samples we noticed over growth of CNT (sample 4 and 5). This high density clearly shows that the catalyst completely filled the pore and even came out of the pore. But it also clearly shows the confinement of the CNTs only near the pore region. Table 4-5 shows that for CNTs grown inside the lateral PAA templates, the tube diameter is less than that of the pore size. This was already discussed in the case (d) for the growth mechanism shown in Figure 4-5, where the catalyst particle size is less than the pore diameter, there is only very few cases where the CNT diameters are approximately equal to the pore diameter. The size of the nanoparticle cluster is determined by the substrate roughness and reaction parameters, such as the gas flow rate and the temperature gradient. In our case, the  $\text{Al}_2\text{O}_3$  provides high roughness which makes the nanoparticle island smaller or the catalyst diffuses through the  $\text{Al}_2\text{O}_3$  to the aluminum at the back side. It is well known fact that diameter of the MWCNT is proportional to the size of the catalyst island.

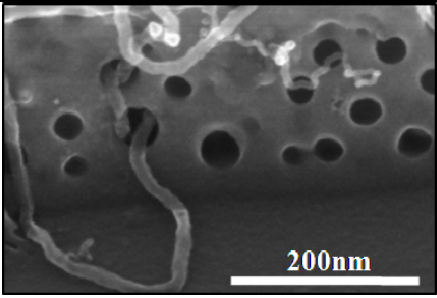
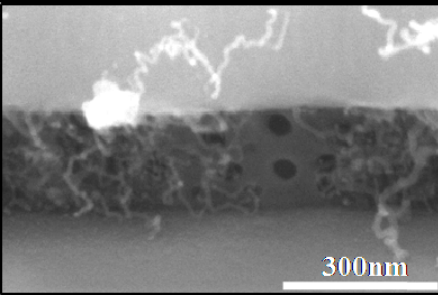
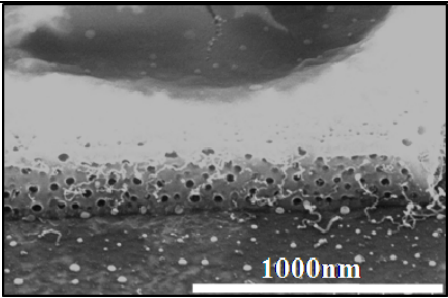
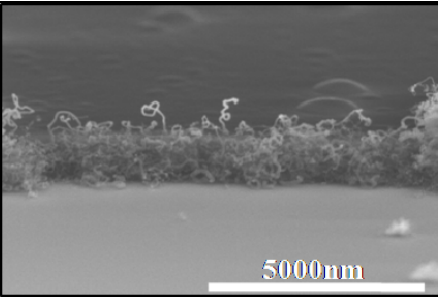
Table 4-4: Growth conditions for the CNT growth

1	Electrodeposition	<u>Voltage</u>	<u>frequency</u>	<u>Time</u>	
	(Co)	6V	100 Hz	30 s	
	Growth	<u>Temperature</u>	<u>Gas</u>	<u>Working pressure</u>	<u>Time</u>
		620°C	C <sub>2</sub> H <sub>2</sub> -30 sccm, H <sub>2</sub> O -10 sccm	10 mbar	15 min
2	Electrodeposition	<u>Voltage</u>	<u>frequency</u>	<u>Time</u>	
		6V	100 Hz	30 s	
	Growth	<u>Temperature</u>	<u>Gas</u>	<u>Working pressure</u>	<u>Time</u>
		620°C	C <sub>2</sub> H <sub>2</sub> -30 sccm, H <sub>2</sub> O -10 sccm	10 mbar	15 min
3	Electrodeposition	<u>Voltage</u>	<u>frequency</u>	<u>Time</u>	
		6V	100 Hz	15 s	
	Growth	<u>Temperature</u>	<u>Gas</u>	<u>Working pressure</u>	<u>Time</u>
		620°C	C <sub>2</sub> H <sub>2</sub> -30 sccm, H <sub>2</sub> O -10 sccm	10 mbar	15 min
4	Electrodeposition	<u>Voltage</u>	<u>frequency</u>	<u>Time</u>	
		6V	100 Hz	60 s	
	Growth	<u>Temperature</u>	<u>Gas</u>	<u>Working pressure</u>	<u>Time</u>
		620°C	C <sub>2</sub> H <sub>2</sub> -30 sccm, H <sub>2</sub> O -10 sccm	10 mbar	15 min
5	Electrodeposition	<u>Voltage</u>	<u>frequency</u>	<u>Time</u>	
		6V	100 Hz	90 s	
	Growth	<u>Temperature</u>	<u>Gas</u>	<u>Working pressure</u>	<u>Time</u>

		620°C	C <sub>2</sub> H <sub>2</sub> -30 sccm, H <sub>2</sub> O -10 sccm	10 mbar	15 min
--	--	-------	---	---------	--------

Because of the 10 and 15 min growth times, CNTs and SiNWs have grown longer than the width of the membrane, protruding out of it. For the CNT growth, we have used H<sub>2</sub>O in order to keep the catalyst surface active and increase the growth time of the CNT. Without water vapor the growth would be stopped by catalyst poisoning or clustering. So controlling the CNT growth inside the nano pores is found to be a complicated process and in the future, more studies are needed.

**Table 4-5: CNT growth inside lateral PAA templates**

Sample		sample	
1		2	
3		4	

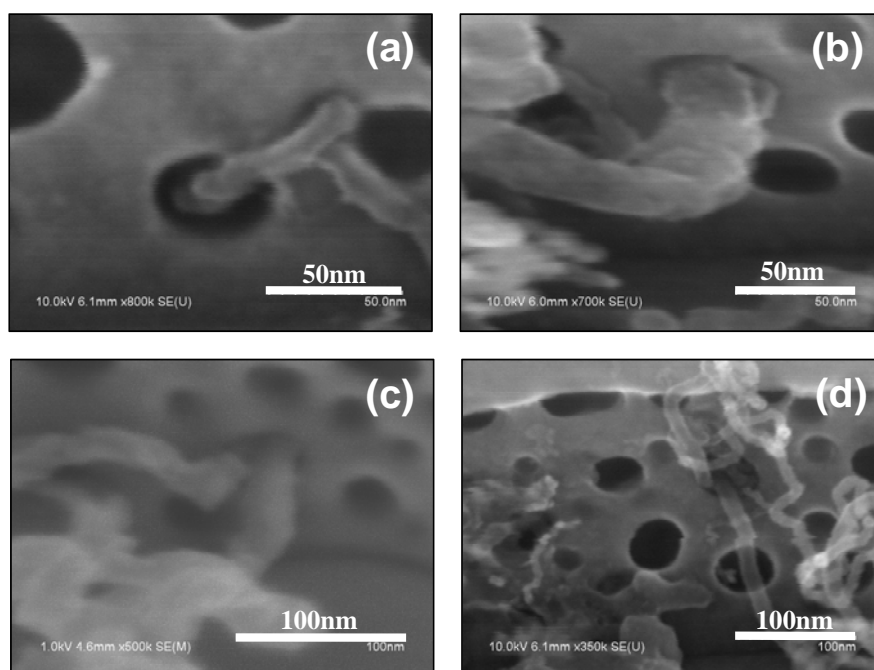
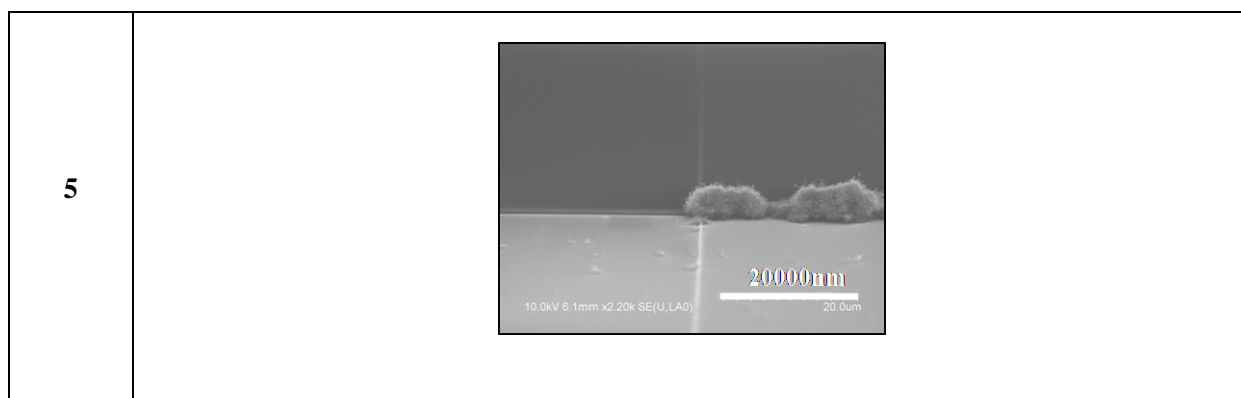


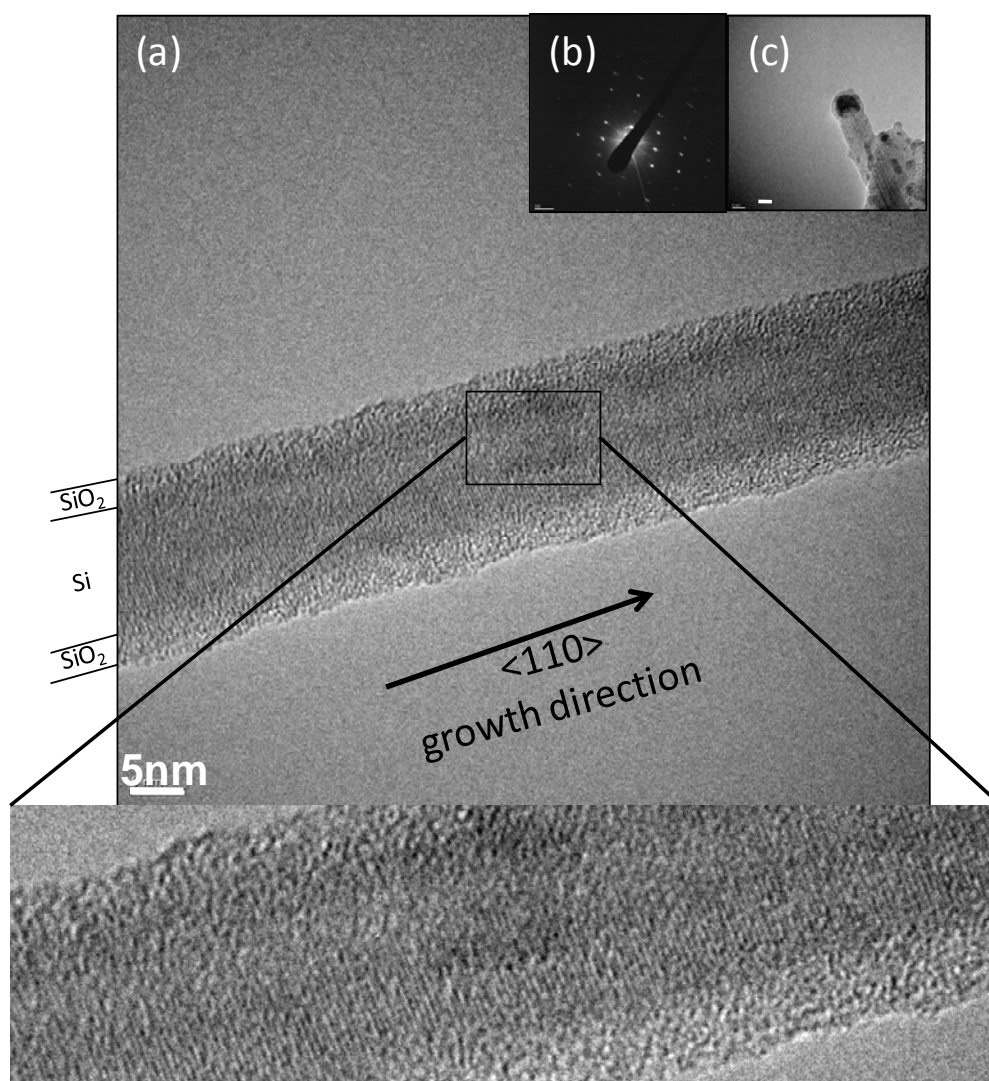
**Figure 4-9:** Different number of CNTs per pore (a) one CNT per pore - smaller than the diameter of the pore, (d) one CNT- equivalent to the diameter of the pore, (c) two CNTs per pore, (b) five CNTs per pore

As discussed in the mechanism of the CNT growth, a different number of tubes in one pore is found in some cases (shown in Figure 4-9), due to the splitting of the catalyst. And also the growth rate of the CNT is very high and the catalyst sites are well activated after the H<sub>2</sub>O treatment. So CNT growth occurs immediately in all possible catalyst sites, and the CNT diameter varies from 10nm to 40nm.

### 4.6.1. HRTEM CHARACTERIZATION

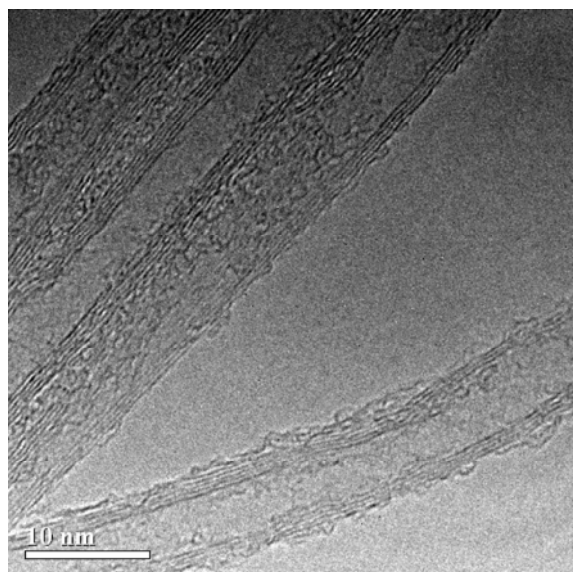
In order to characterize the NWs and CNTs grown in lateral templates, we have performed some high resolution transmission electron microscopy (HRTEM) observations. The samples for HRTEM observations were prepared by scratching the SiNW and CNT grown PAA templates directly on the TEM grids.

Figure 4-10 clearly shows the single crystal SiNW of 12-15 nm diameters with no defects with 2-3 nm of naturally grown amorphous SiO<sub>2</sub> on the outermost surface. Inset (b) shows the diffraction images of the magnified region and the inset (c) shows the catalyst at the top (white bar represents the scale of 5nm). Structural characterization of a large number of samples shows that the NWs exhibit a narrow diameter distribution and that the NWs grow primarily along the <110> direction.



**Figure 4-10:** HRTEM image showing a silicon nanowire grown in lateral PAA template. The magnification shows crystalline lattice planes of the nanowire, (b) shows the diffraction images of the magnified region and (c) shows the catalyst at the top (white bar represents the scale of 5nm).

Figure 4-11 clearly shows that CNTs grown in lateral PAA templates are multiwall CNTs with well graphitized walls. But lots of structural defects are noticed, even in SEM images. This may be due to the growth temperature which is low and the growth rate which is quite high.



**Figure 4-11:** HRTEM image showing carbon nanotubes grown in a lateral PAA template. It is clearly seen that they are multiwall CNTs with well graphitized walls

In general the quality of the lateral PAA grown SiNW are better than that of the CNTs. SiNW are always found to be straight in every pore even after they come out of the pore.

#### 4.7: CONCLUSION

In conclusion, we have seen that the differences in the growth between the CNTs and the NWs are strongly due to the growth rate and the catalyst activation. Also from the catalysts behavior with the respective gases which are completely different for the CNTs and SiNW.

SiNW shows very positive results, with a good crystallinity and a uniform diameter. But still improvement is needed to increase the density over a wide area.

The upper limit of the diameter for both CNTs and SiNW are limited by the pore diameter of the PAA structure, which can be controlled easily by the electrochemical process. Here the confinement is obtained by the PAA structure itself, which can provide access to the individual CNT or NW. This is not possible by any other reported approaches. We also came up with possible solutions to provide good control on the diameter by two different approaches (details are given in annex II).

## **Chapter 5: Conclusion and outlook**



## 5: CONCLUSION AND OUTLOOK

We have addressed the problem of the organization of the CNTs / NWs and suggested the advantages of the PAA template based approach, and proposed the novel lateral PAA template based approach.

Further details of the porous anodic alumina system are discussed and we have shown the control over the pore diameter both in self and non self ordered regimes.

The fabrication and the different ways to control the pore structure of the lateral PAA templates have been studied. We have also shown the effect of the confinement by patterning aluminum lines, both at micro and nanoscale. These confinement effect leads to organization of 1-D arrays of nanopores. Finally the mechanism of the spatially constrained anodization process has been discussed.

The catalyst choices have been explored for both CNTs and the SiNWs and the problem of electrodeposition were discussed to fill the templates efficiently. Later the growth mechanism inside the porous alumina was discussed and finally we have demonstrated the CVD grown CNTs and SiNWs in these lateral PAA templates. We claim that with this method, it is possible to place individual tubes or wires with a high density.

Overall we have developed a new fabrication methodology for fabricating lateral PAA templates and also investigated the mechanism of the pore formation. By using this approach we demonstrated the feasibility of growing nanostructures such as CNTs and SiNWs in lateral PAA templates. These lateral membranes filled with CNTs or SiNWs can be further processed just like any thin film by using the classical microelectronic tools (lithography etc...) in order to fabricate electronic devices with a controlled density of SiNWs or CNTs and with a precise end-to-end registration. If the pore diameter is decreased down to  $\sim 5$  nm, potential linear densities of 100 NWs or CNTs/ $\mu\text{m}$  can be obtained, and even more if the nano-objects are stacked in 3-D.

Even if the proposed method is the combination of well understood technologies, still there is lot of room for improvement and further understanding is necessary before any further applications can be made.

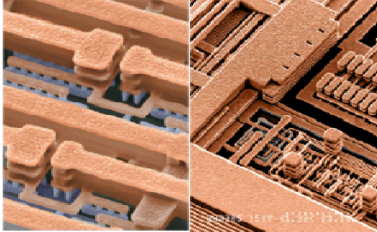
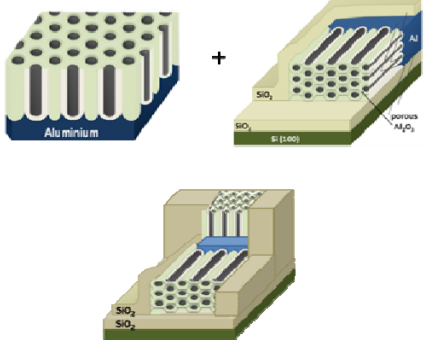
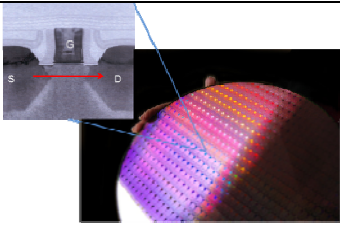
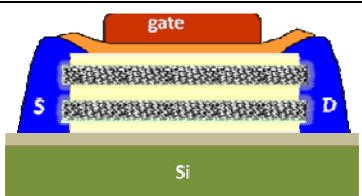
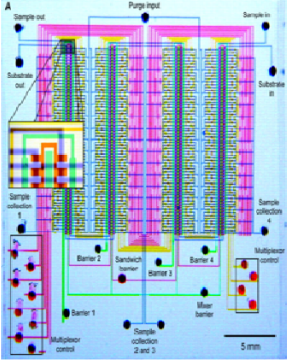
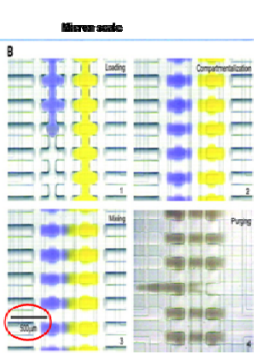
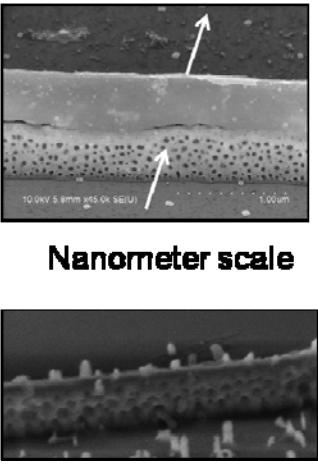
### OUT LOOK

This successful growth of well ordered pores in the plane can be transformed easily to the wafer scale and it enables incorporation of a variety of nanomaterials into conventional semiconductor fabrication processes. Thus this method is one of the important steps for exploring applications in nanotechnology utilizing porous alumina.

Table 5-1 shows the possible applications, which are considered as being important problems in the field of electronics and biophysics.

1. Interconnection: By filling or growing the combined system of vertical and lateral templates can be used for interconnects. Because this PAA structures can give the 1D, 2D and 3D nanochannels, which can be used for the future interconnections.
2. Planar type devices: Further improving the growth of NW or CNT inside these lateral PAA and by additional lithography steps and connections pad can give field effect transistors or sensors.
3. Nanofluidics: Reducing the existing microfluidics to the nanoscale gives the ability to control fluids in channels of such small dimensions. This will leads to advances in basic research and technological innovations in biology, chemistry, engineering, and physics. This can give new materials, new fabrication methods, cooling of electronic devices, multiphase flows in labs-on-a-chip, and improve the understanding of the basic processes in individual biological cells.

**Table 5-1:** Possible applications using the lateral porous alumina templates

<p>Interconnections</p>	 <p>IBM's three-level copper interconnect technology</p> <p>IBM's six-level copper interconnect technology</p>	 <p>Aluminum</p> <p>Si (100)</p> <p>porous Al<sub>2</sub>O<sub>3</sub></p> <p>SiO<sub>2</sub></p> <p>SiO<sub>2</sub></p>
<p>Planar type devices</p>		 <p>gate</p> <p>S</p> <p>D</p> <p>Si</p>
<p>Nanofluidics</p>	 <p>Sample inlet</p> <p>Purge inlet</p> <p>Sample in</p> <p>Substrate II</p> <p>Substrate I</p> <p>Sample collection 1</p> <p>Sample collection 4</p> <p>Barrier 1</p> <p>Barrier 2</p> <p>Barrier 3</p> <p>Barrier 4</p> <p>Mixer barrier</p> <p>Multiplex control</p> <p>Sample collection 2 and 3</p> <p>5 μm</p>  <p>Microfluidic</p> <p>Loading</p> <p>Compensation</p> <p>Mixing</p> <p>Pumping</p>	 <p>10 kV 5.0mm x50k SE(U)</p> <p>1.00 μm</p> <p><b>Nanometer scale</b></p>



## Annex I: Technological steps for The Lateral CNT/ SiNW-FET Fabrication



## ANNEX I: TECHNOLOGICAL STEPS FOR THE LATERAL CNT/ SiNW-FET FABRICATION

### 1. THERMAL OXIDE WAFER

Silicon wafers with the following configuration are bought for this process.

**Table 1:** Commercial wafer from Si MAT

<b>Type</b>	Float Zone
<b>Resisitvty</b>	>10000 ohmcm
<b>Diameter</b>	100 mm
<b>Thickness</b>	525 +/- 10 $\mu$ m
<b>Polished</b>	Single side
<b>Orientation</b>	<100>
<b>Type</b>	N/Phos
<b>Thermal Oxide</b>	500nm(both sides)

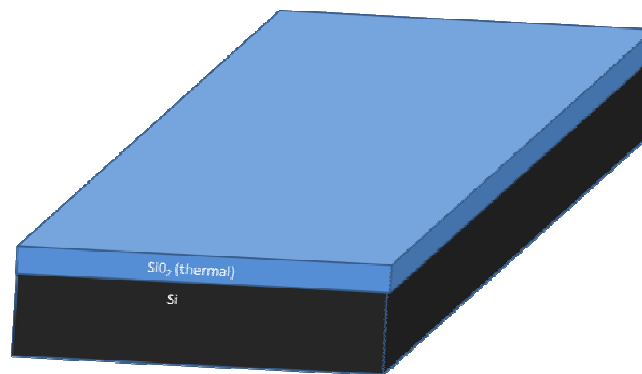


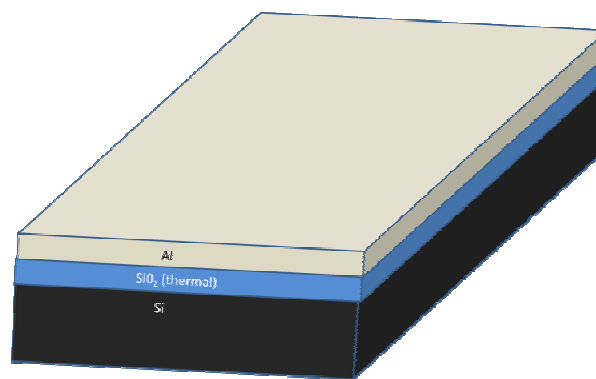
**Figure A-1-1:** Thermal oxide on Silicon wafer

## 2. ALUMINUM DEPOSITION

We used e-beam evaporation for depositing Aluminum thin films (semi-automatic Plassys MEB 550 S)

I- 0.40 A; deposition rate - 0.5 nm /sec.

The overall uniformity is good on 4 inch diameter with only very small differences (~5 nm) found at the edges of the wafer.



(a)

**Figure A-1-2** :, Aluminum on SiO<sub>2</sub> / Si wafer

## 3. PHOTOLITHOGRAPHY – I

Just after the aluminum evaporation, photolithography is done. For that we used Shipley photoresist (PR) S1813, before depositing PR, the aluminum surface is functionalized with the silane based chemical reagent-1,1,1,3,3,3-Hexamethyldisilazane (CH<sub>3</sub>)<sub>3</sub>Si-NH-Si(CH<sub>3</sub>)<sub>3</sub>, usually called as HMDS, that is found to be good adhesion promoter with PR.

A few ml of HMDS were dropped on the center of the wafer and were spin coated for a few seconds.

From the standard spin speed graph for the S1800 series, we chose 3000 rpm to get a thickness of around 1.3 micron, which is good enough to protect the aluminum during etching.

Just after PR spin coating, soft baking is done at 115 °C for 90 seconds. The next step is the mask alignment and exposure. For this we used an EVG 620 aligner. The mask was designed by LASI 7; see Figure A-1-3 for more details.

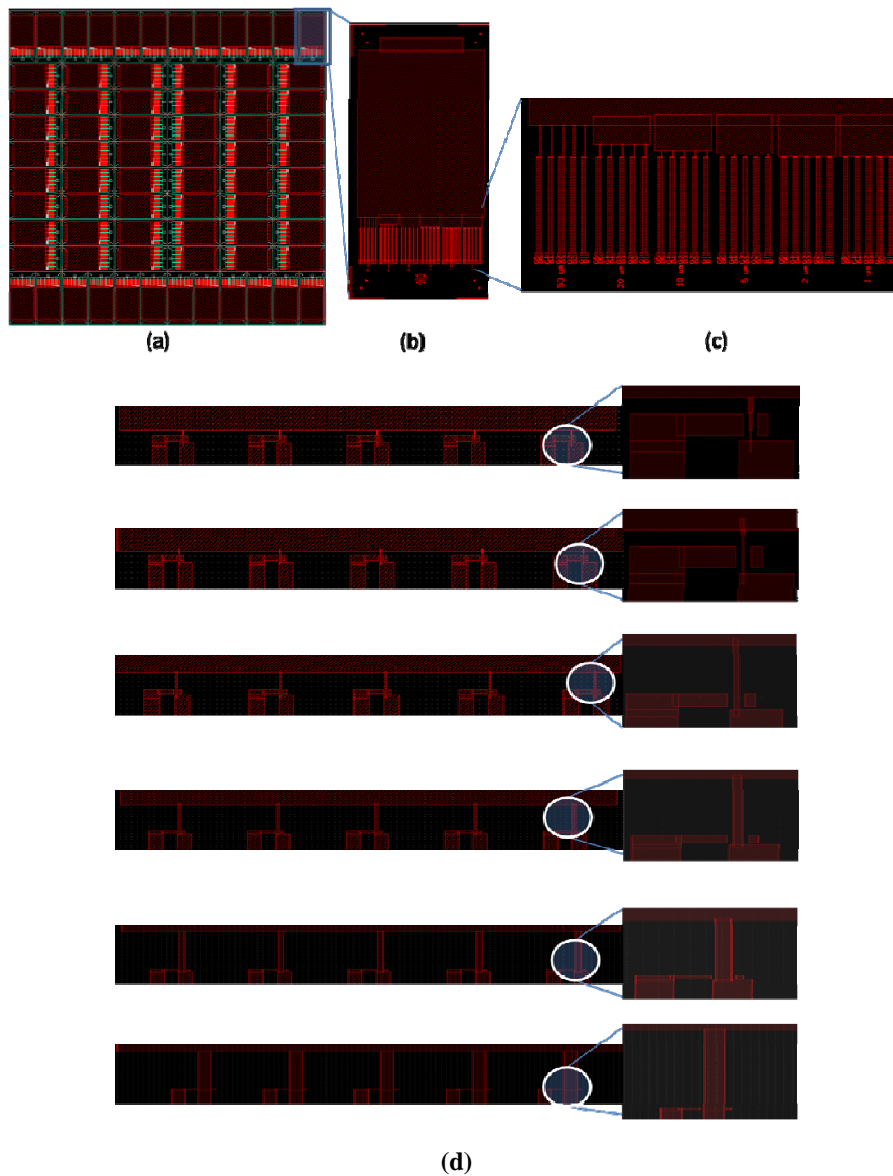


**Figure A-1-3: Mask I**

Figure A-1-3 (a) represents the entire mask layout of Mask I, you can see 72 individual cells. Each cell has 6 different stripe widths (Figure A-1-3 (b)), each strip of the same width has 5 stripes (see Figure A-1-3(c) & (d)).

Each cell has six different parts with different widths ( $1\mu\text{m}$ ,  $2\mu\text{m}$ ,  $5\mu\text{m}$ ,  $10\mu\text{m}$ ,  $20\mu\text{m}$ ,  $50\mu\text{m}$ ). Each part has five stripes of same width. One cell has 30 stripes ; in total the entire wafer has 2160 stripes. The

stripes marked green in the Figure A-1-4 are used for the contact to fabricate devices out this structure, but these stripes are not used in these process steps.

Alignment was done with this mask (I) and the wafer with spin coated photoresist on it was exposed with this mask at  $25 \text{ mJ/cm}^2$  (which was already optimized for this photoresist).

After exposure, the wafer was developed by using 351 developer for 25 seconds. Then the remaining aluminum was etched by commercial aluminum etchant from Transcene. After removing the photoresist completely, the sample looks as shown in Figure A-1-4.

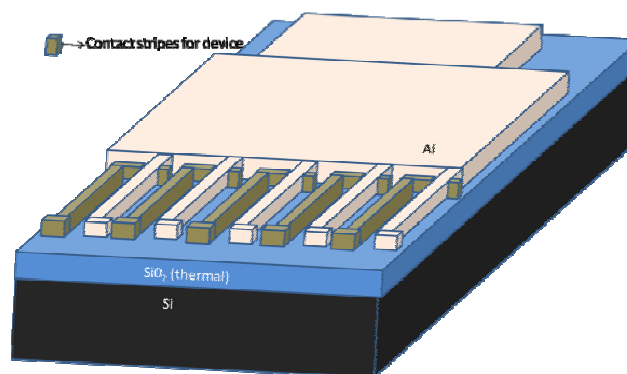


**Figure A-1-4** : Aluminum stripes after the first lithography

#### 4.ENCAPSULATION

Encapsulation of the aluminium was done by depositing  $\text{SiO}_2$  on these aluminium stripes. For this we used PECVD –RF (Surface Technology Systems). The following conditions are used for depositing  $\text{SiO}_2$  films. This step is done to protect the three faces of the aluminum before the anodization step. The adhesion of  $\text{SiO}_2$  with aluminum is found to be good

**Table 2:**  $\text{SiO}_2$  Deposition Conditions

<b>Gas flow</b>	<b><math>\text{SiH}_4</math> – 400 sccm</b> <b><math>\text{N}_2\text{O}</math> – 1420 sccm</b>
<b>Power</b>	20W
<b>Frequency</b>	RF 13.6 MHz
<b>Substrate temperature</b>	300°C

<b>Working pressure</b>	800mT
<b>Deposition time</b>	14.8 min
<b>Thickness</b>	500nm

The uniformity is also found to be good all over the substrate. Finally the entire wafer will be covered by SiO<sub>2</sub> as shown in the FigureA-1-5.

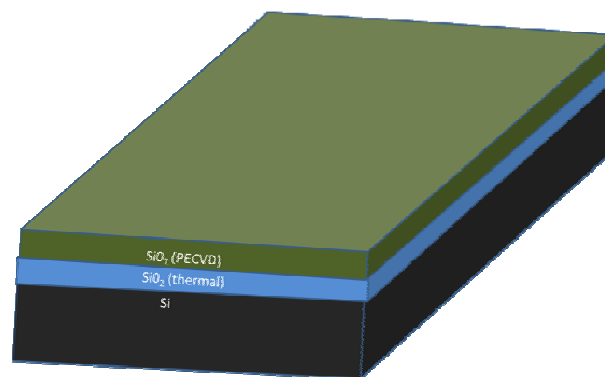


**Figure A-1-5:** Encapsulation of Aluminum stripes with SiO<sub>2</sub>

## 5. PHOTOLITHOGRAPHY – II

The second lithography is done to allow the encapsulation for the anodization. The same process is used for photoresist coating and soft baking as in step-1. For exposure we used mask (II)

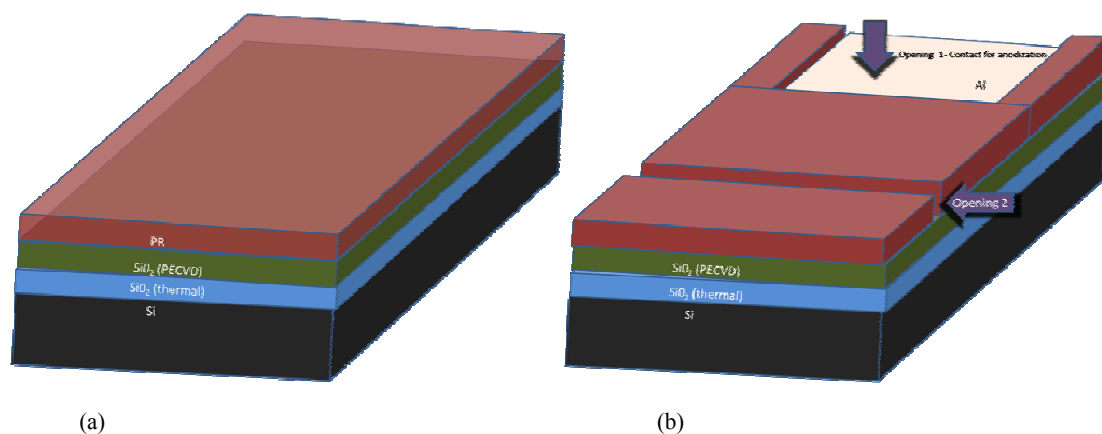


**Figure A-1-6:** Photolithography II - (a) before exposure (b) after exposure and development

## 6. REACTIVE ION ETCHING

After the opening of the PR in two different locations, as shown in Figure A-1-6, the exposed  $\text{SiO}_2$  was etched by reactive ion etching (Surface Technology Systems). Since aluminium was found below the  $\text{SiO}_2$ , we used an oxygen free environment during the etching.  $\text{CF}_4$  and  $\text{CHF}_3$  are chosen for this process as an etching gas. Etching was done using the following conditions to obtain straight opening. To know the end point of  $\text{SiO}_2$  etching a laser interferometric camera and endpoint detector was used.

**Table 3:** Conditions for etching  $\text{SiO}_2$

<b>Gas flow</b>	<b><math>\text{CF}_4</math> – 12 sccm</b> <b><math>\text{CHF}_3</math>- 50 sccm</b>
<b>Power</b>	200W
<b>Frequency</b>	RF 13.6 MHz
<b>Substrate temperature</b>	300°C
<b>Working pressure</b>	20mT
<b>Etching time</b>	16 min
<b>Thickness</b>	500nm
<b>Chamber peak to peak Voltage</b>	1260 V
<b>Chamber bias voltage</b>	370 V

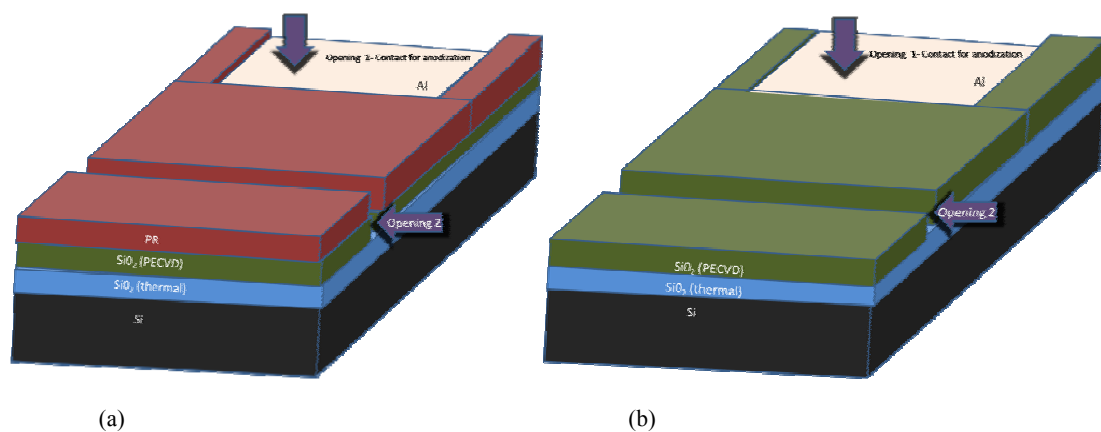


**Figure A-1-7:** After RIE (a) with PR (b) without PR

After this process the PR become hard, so it can be only removed by prolonged acetone etching and in a ultrasonic enviornment for short time.

## 7. ELECTROCHEMICAL PROCESS

Electropolishing and anodization was done with the conditions described in chapter 3.

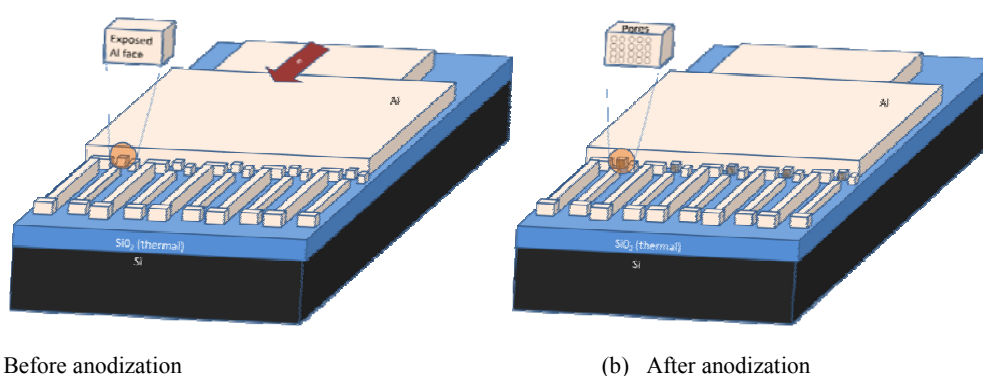


**Figure A-1-8:** (a) shows the structure without SiO<sub>2</sub> for better understanding . The arrow indicates the electric field direction during anodization. Only the exposed aluminum face will be anodized. (b) shows the pore arrays after anodization, where the pores are developed laterally.

Figure A-1-8 (a) shows the real sample prepared from the clean room before anodization and (b) shows after anodization, just the capping layer is not shown for better undering.

### *ELECTRODEPOSITION*

The metal catalyst particles (Co for CNT and Cu for SiNW) were then electrodeposited at the bottom of the pores, using either a solution of cobalt sulfate (CoSO<sub>4</sub>) or copper sulfate (CuSO<sub>4</sub>) buffered with boric acid (H<sub>3</sub>BO<sub>4</sub>) leading to a pH around 3.8, as electrolytes. Here, the electrodeposition configuration is a classical 3-electrode type, where the sample is set as the working electrode, a graphite bar acts as a counter electrode and a standard reference electrode (Ag/AgCl -3MKCl) is employed. We used a pulsed electrodeposition mode and the best conditions were reached in the case of a pulse of -4V applied during 1ms, followed by a plateau of 99ms at the beginning open circuit potential value. Typically, this cycle is repeated 200 times.

## 8. CNT GROWTH

After the preparation of the membrane and the electrodeposition of the catalyst particles inside the pores, the samples were loaded in a CVD reactor and heated to the growth temperature under a  $10^{-6}$  mbar pressure. Once the growth temperature reached, the samples were first annealed under a  $H_2$  atmosphere (15 mbar) for 15 min, in order to stabilize the membranes.

Growth conditions for the CNT and SiNW are discussed in chapter 3. In Figure A-1-9 is an example of the sample after the growth for the CNT case.

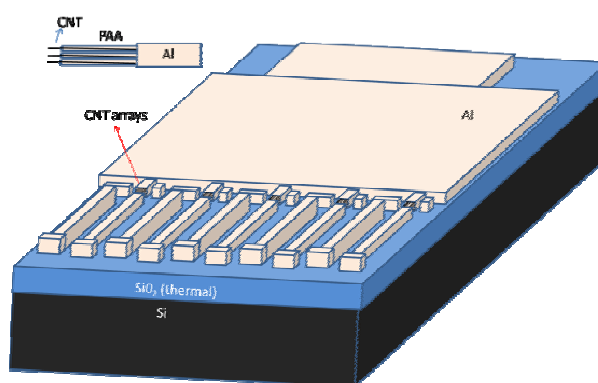


**Figure A-1-9:** CNT growth inside PAA templates

## 9. ANNEALING(FUTURE WORK)

This step is done to increase the quality of the alumina, after etching the aluminum pads, by  $HgCl_2$ .

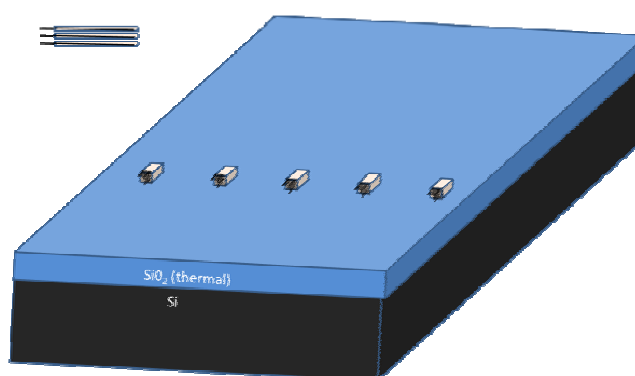


**Figure A-1-10:** PAA/CNT after etching aluminum

## 10. S/D AND GATE ELECTRODE DEPOSITION(FUTUER WORK)

This was done in two alternate lithography steps with Mask III and Mask IV

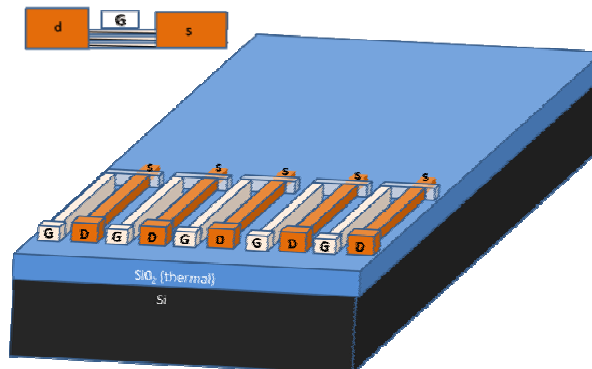
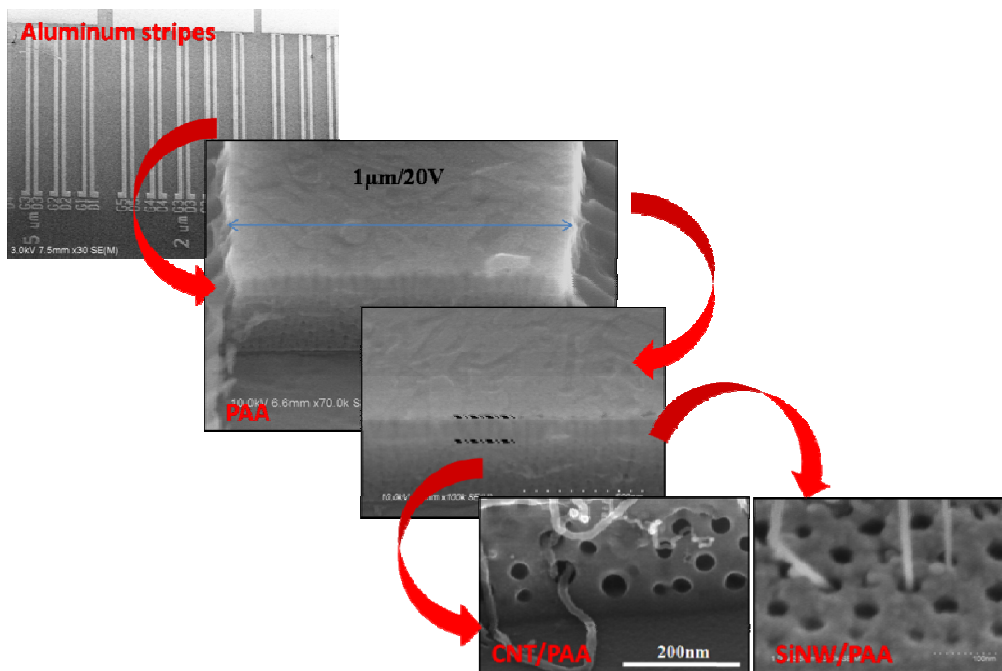


Figure A-1-11: Final FET structure

## CONCLUSION

The flow chart for technological process is CMOS compatible and it has been verified in every step of the process.

The following pictures are demonstrating the evolution of the development work for CNT/NW-FET templates from pore formation to catalyst filling in nano holes and CNT/NW growth.





## **Annex II: Alternate technology adaptation**



---

## ANNEX II: ALTERNATE TECHNOLOGY ADAPTATION

From the conclusion of the chapter 4, it is well understood that it is important to have a small quantity of catalyst at the pore bottom to obtain SWCNT or SiNW with less diameter (<10nm). Even though a well controlled electrodeposition can do that job, we have explored the other possible ways to achieve this goal. Dielectrophoresis of protein is found to be one of the best ways to fill the nano pores.

### DIELECTROPHORESIS OF PROTEIN

Having less metal is the objective of our study; this applies even to the most forms of life in our planet. Every form of life needs a less amount of metal, too much of it is harmful. Especially iron (Fe) is found in certain living systems. To solve this problem nature came up with the solution and a cage protein named ferritin evolved in the course of life on earth million years ago.

Fe found within this protein is ranging from a single atom to the macroscopic crystals of various ferric oxides in certain organisms. The protein functions to keep a reserve supply of this essential metal in a soluble, non-toxic and usable form inside the cytoplasm of eukaryotic and prokaryotic cells. Unless biological iron is bound to ferritin, other proteins, or certain organics, the oxygen-rich atmosphere rapidly results in the formation of insoluble iron oxides (rust)<sup>241</sup>.

In our case, Fe is found to be the best catalyst to obtain SWCNTs, but it is very difficult to deposit it by electrodeposition method, because it oxidizes immediately in the solution form. So we have taken the solution given by nature and decided to use this ferritin as a catalyst for the SWCNTs growth.

Ferritin has a spherical hollow shell composed of 24 polypeptide subunits and has the ability to isolate and store iron as hydrated iron oxide in the internal cavity<sup>242</sup>. The inner and outer diameters of the protein shell are about 7 nm and 12 nm respectively. The molecular weight of one subunit is 18.5kDa and the whole molecule is about 450 kDa in case of horse spleen ferritin. The empty cell is called as apoferritin. The inner cavity of apoferritin was used as a restricted chemical reaction chamber to synthesize homogeneous inorganic Nano Particles (NPs)<sup>243,244,245,246</sup>. First discrete SWCNTs from discrete nanoparticles are reported only by using this ferritin protein. Also it has been shown that the core of ferritin can be emptied to afford apoferritin, and subsequently, a controllable number of Fe (III) atoms can be put back into the core<sup>247</sup>. By taking into account the advantage of this catalyst system, we have

planned to fill our lateral PAA templates with this ferritin to get a complete control on the nanoparticle size, in order to give rise to highly monodispersed SWCNTs.

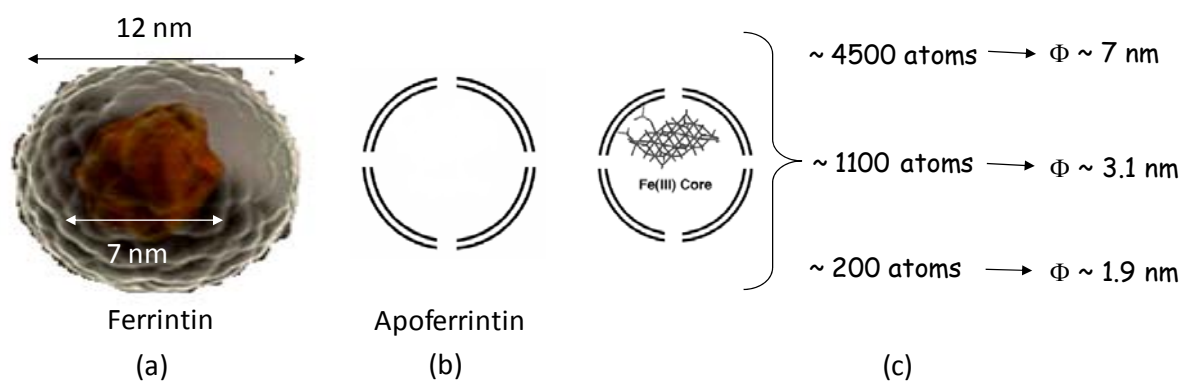


**Figure A-2-1:** (a) shows the diagram of ferritin molecule, where the inner core was filled with iron atoms with the diameter of 7nm and the outer protein shell diameter is found to be 12nm, (b) schematics of the apoferritin and the different filling ratios with their respective diameter of Fe shown in (c)

## EXPERIMENTS

We have used the Apoferritin (from horse spleen) from Sigma-Aldrich. In order to study different number of the atoms following experiments was carried out;

- 1) 10 mg (0.022 mM) apoferritin was added to 50 ml MES\* (0.05 M, pH 7.0 by NaOH or KOH).
- 2) The solution was stirred at room temperature.
- 3) 35 ml of 0.025 M ammonium iron sulfate (40 Fe/apoferritin loading) was added dropwise.
- 4) Me<sub>3</sub>NO (0.025 M, 35 ml) was added to fully oxidize Fe (II) to Fe(III)
- 5) 3) and 4) were repeated 5 times at 15 min intervals to achieve a theoretical loading of ~200 Fe(III)/ferritin.
- 6) Stirring was done overnight at room temp.
- 7) The resultant solution was dialyzed overnight against distilled water at 4 °C and centrifuged at 16000 g for 15 min to remove the aggregates.
- 8) The solution was stored at 4°C when not in use.

\* MES: 2-(N-Morpholino)-ethanesulfonic acid

Me<sub>3</sub>NO: trimethylamine-N-oxide

Before the filling process inside the lateral PAA templates by dielectrophoresis, we studied the growth conditions on the plane substrate. For this the final ferritin contained solution was spin coated on (3-Aminopropyl)Triethoxysilane -APTES coated SiO<sub>2</sub> substrate. Then calcination was done at 450°C in air to remove the protein shell immediately followed by reduction at 700°C for 10 min with H<sub>2</sub>/N<sub>2</sub> & CNT growth at 700 °C for 10 min with C<sub>2</sub>H<sub>2</sub>/N<sub>2</sub> in the thermal CVD reactor. Figure A-2-2 shows the results for the different concentration of Fe atoms.

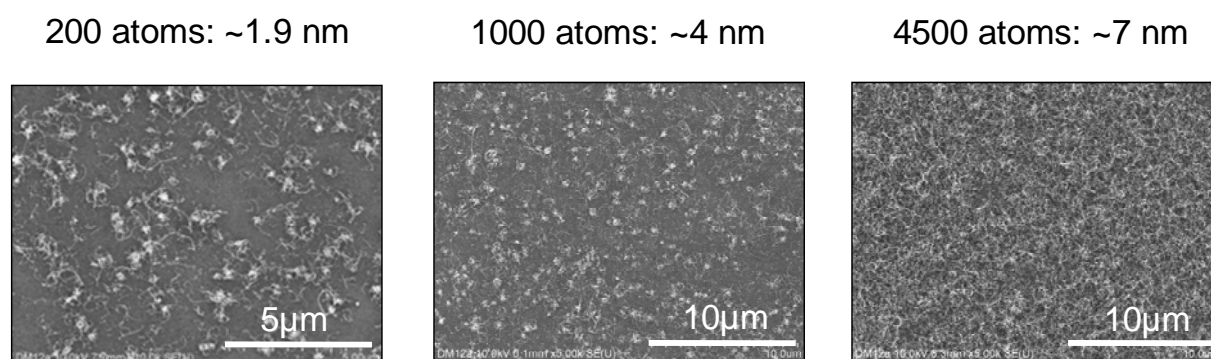


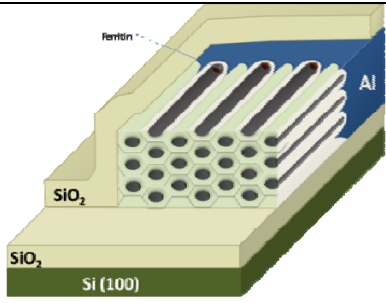
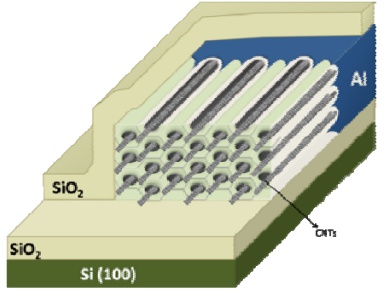
**Figure A-2-2:** SEM images of the CNT growth with different concentration of Fe atoms filled inside apoferritin

The result shows the CNTs growth with different concentration of Fe atoms filled inside the apoferritin, it's clearly seen that there are some aggregation. This may be due to the aggregation of the catalyst during the reduction process. This can be solved in the template based approach. By this experiment, we just tested the feasibility of CNT growth by using ferritin in our growth conditions.

In order to fill the protein inside the PAA template, we have chosen dielectrophoresis technique (DEP). This technique is a well established technique used in the field of biology. By this technique it is possible to drive ferritin inside the PAA pores.

**Table A-2-1:** Process steps of the ferritin filling technique

Steps	Process
1	Ferritin preparation
2	Dielectrophoresis

	
3	Calcination
4	CNT growth(catalyst was not shown, since the mechanism of CNT growth is not clear) 

Initially trials of the growth inside the lateral PAA templates shown no growth, this may be due to the problem in the diffusion of the ferritin inside the nanopores. It is also noted that, cationized ferritin (positively charged) are available commercially, this charged ferritin can be easily driven inside the nanopores during the dielectrophoresis.

This process can be adapted for the SiNW growth, just by changing the salt during apoferritin filling. For example Cu based salt can be used for SiNW, instead of Fe based salt, which was used for SWCNT.

# LIST OF PUBLICATIONS

## Journals

1. Controlled Growth of Carbon Nanotubes and Silicon Nanowires in lateral porous alumina templates.

**M. Gowtham**, L. Eude, B. Marquardt, A.Q.L. Quang, C.S. Cojocaru, P.Legagneux, B.S.Kim and D.Pribat (submitted)

2. Controlled fabrication of patterned lateral porous alumina membranes

**M.Gowtham**, L.Eude, C.S. Cojocaru, B.Marquardt, H.J.Jeong, P.Legagneux and D.Pribat.

Nanotechnology, Vol 19, p035303,2008

3. Atomic hydrogen driven size control of catalytic nanoparticles for single-walled carbon nanotubes growth

Hee Jin Jeong, Laurent Eude, **Manoharan Gowtham**, Bernd Marquardt, Sung Hun Lim, Shaima Enouz, Costel Sorin Cojocaru, Didier Pribat, Kyung Ah Park and Young Hee Lee

Nano, Vol. 3, No. 3, 145, 2008

4. Density control of electrodeposited Ni nanoparticles/nanowires inside Porous Anodic Alumina Templates by an Exponential Anodization Voltage Decrease

B. Marquardt, L. Eude, **M. Gowtham**, G. Cho, H. J. Jeong, M. Châtelet, C. S. Cojocaru, D. Pribat, and B. S. Kim

Nanotechnology, Vol 19, 405607, 2008

5. Carbon nanotubes and semiconductor nanowires for active-matrix backplanes

Pribat D, Cojocaru C S, **Gowtham M**, Eude L, Bondavalli P, Legagneux P.

J. Soc. Inf. Display., 15, 595, 2007

## International Conferences and Proceedings

1. Confined and controlled growth of Silicon nanowire for planar type devices

**Gowtham Manoharan**, Laurent Eude, Bernd Marquardt, Anh Quoc Le Quang, Costel sorin Cojocaru, Pierre Legagneux, Didier Pribat

Oral presentation, November 19-21, JNTE 08, Toulouse, France

2. Applications of porous anodic alumina membranes in the field of displays

D. Pribat, C. Cojocaru, **M. Gowtham**, B. Marquardt, L. Eude, and B.S. Kim

November 11-13, The 4th International Crystal Valley Conference & Exhibition 2008 (CVCE2008), , 2008 Asan, KOREA

3. Novel approach to align carbon nanotubes for planar type devices

D. Pribat, **M. Gowtham**, C. Cojocaru, B. Marquardt, and A. Q. L. Quang

Proc. SPIE, Vol. 7037, 70370N (2008)

4. Fabrication of Patterned Lateral Templates with Different Arrays in Device Oriented Approach

**M.Gowtham**, L. Eude, C. Cojocar, P. Didier.

2007 November, MRS Fall Meeting, Boston, USA

**5.** Alumina membranes as etching mask

B. Marquardt, S. Xavier, G. Cho, L. Eude, **M. Gowtham**, C. Cojocar and D. Privat.

Trends in Nanotechnology (TNT), 2007 September, San Sebastian, Spain.

**6.** Novel approach to align carbon nanotubes for the integrated circuit engineering

**M.Gowtham**, L.Eude, H.Jeong, C.S.Cojocaru and D.Priat.

Cargèse International summer school on NanoSciencesTech, 2006 July, Cargèse, France.

## REFERENCES

- <sup>1</sup>This saying appears in the dialogue *Republic*, by the ancient Greek philosopher Plato written in approximately 360 BC
- <sup>2</sup>NW for ultimate CMOS, P. Coronel, ST microelectronics, Semiconductor Nanowires Summer school 2008, Roscoff
- <sup>3</sup>G. E. Moore, *Electronics*, **38**, 8(1965)
- <sup>4</sup>Executive summary - ITRS conference 2007
- <sup>5</sup>S. E. Thompson *et al*, *IEEE Electron Device Lett.*, **25**, 191(2004)
- <sup>6</sup>S. Datta *et al*, *Int. Electron Devices Meeting Tech. Dig.*, 653(2003)
- <sup>7</sup>R. Chau *et al*, *Extended Abstract Int. Gate Insulator Workshop*, Tokyo, Japan, 124(2003)
- <sup>8</sup>R. Chau *et al*, *Physica E*, **19**, 1(2003)
- <sup>9</sup>A. Javey *et al*, *Nat. Mater.*, **1**, 241(2002)
- <sup>10</sup>A. Javey, Q. Wang, W. Kim, H. Dai, *Int. Electron Devices Meeting Tech. Dig.*, 741(2003)
- <sup>11</sup>A. Javey, Q. Wang, A. Ural, Y. Li, H. Dai, *Nano Lett.*, **2**, 929(2002)
- <sup>12</sup>L. J. Lauhon, M. S. Gudiksen, D. Wang, C. M. Lieber, *Nature*, **420**, 57(2002)
- <sup>13</sup>Y. Cui, Z. Zhong, D. Wang, W. U. Wang, C. M. Lieber, *Nano Lett.*, **3**, 149(2003)
- <sup>14</sup>Y. Cui, X. Duan, J. Hu, C. M. Lieber, *J. Phys. Chem. B.*, **104**, 5213(2000)
- <sup>15</sup>R. Chau, S. Datta, M. Doczy, B. Doyle, B. Jin, J. Kavalieros, A. Majumdar, M. Metz, M. Radosavljevic, *IEEE Transactions On Nanotechnology*, **4**, 153(2005)
- <sup>16</sup>T. V. Hughes, C. R. Chambers, *US Patent*, 405480(1889)
- <sup>17</sup>P. Schutzenberger, L. Schutzenberger, *C R Acad Sci Paris*, **111**, 774(1890)
- <sup>18</sup>C. Pelabon, H. Pelabon, *C R Acad Sci Paris*, **137**, 706(1903)
- <sup>19</sup>L. V. Radushkevich, V. M. Lukyanovich, *Zurn Fisic Chim.*, **26**,88(1952)
- <sup>20</sup>M. Monthieux, V. L. Kuznetsov, *Carbon*, **44**, 1621(2006)
- <sup>21</sup>A. Oberlin, M. Endo, T. Koyama, *J. Cryst. Growth.*, **32**, 335(1976)
- <sup>22</sup>S. Iijima, *Nature*, **354**, 56(1991)
- <sup>23</sup>R. Saito, M. Fujita, G. Dresselhaus, M. S. Dresselhaus, *Phys. Rev.B.*, **46**,1804(1992)
- <sup>24</sup>R. Saito, M. Fujita, G. Dresselhaus, M. S. Dresselhaus, *Appl. Phys. Lett.*, **60**, 2204(1992)
- <sup>25</sup>N. Hamada, S. Sawada, A. Oshiyama, *Phys. Rev. Lett.* **68**, 1579(1992)
- <sup>26</sup>R. Saito, M. Fujita, G. Dresselhaus, M. S. Dresselhaus, *Phys. Rev. B.*, **46**, 1804(1992)
- <sup>27</sup>J. W. G. Wildoer, L. C. Venema, A. G. Rinzler, R. E. Smalley, C. Dekker, *Nature*, **391**, 59(1998)

- 
- <sup>28</sup>T. W. Odom, J. L. Huang, P. Kim, C. M. Lieber, *Nature*, **391**, 62(1998)
- <sup>29</sup>W. A. De Heer, A. Chatelain, D. Ugarte, *Science* **270**, 1179(1995)
- <sup>30</sup>H. Dai, E. W. Wong, C. M. Lieber, *Science* **272**, 523(1996)
- <sup>31</sup>A. Thess, R. Lee, P. Nikolaev, H. Dai, P. Petit, *Science*, **273**, 483(1996)
- <sup>32</sup>C. Zhou, J. Kong, E. Yenilmez, H. Dai, *Science*, **290**, 1552(2000)
- <sup>33</sup>J. Kong, H. Dai, *J. Phys. Chem.*, **105**, 2890(2001)
- <sup>34</sup>A. Bachtold, P. Hadley, T. Nakanishi, C. Dekker, *Science*, **294**, 1317(2001)
- <sup>35</sup>V. Derycke, R. Martel, J. Appenzeller, Ph. Avouris, *Nano. Lett.*, **1**, 453(2001)
- <sup>36</sup>X. Liu, C. Lee, C. Zhou, J. Han, *Appl. Phys. Lett.*, **79**, 3329(2001)
- <sup>37</sup>G. E. Gadd, M. Blackford, S. Moricca, N. Webb, P. J. Evans, *Science*, **277**, 933(1997)
- <sup>38</sup>H. Dai, J. H. Hafner, A. G. Rinzler, D. T. Colbert, R. E. Smalley, *Nature*, **384**, 147(1996)
- <sup>39</sup>A. Rinzler, J. H. Hafner, P. Nikolaev, L. Lou, S. G. Kim, *Science*, **269**, 1550(1995)
- <sup>40</sup>K. B. K. Teo, E. Minoux, L. Hudanski, F. Peauger, J. P. Schnell, L. Gangloff, P. Legagneux, D. Dieumgard, G.A.J. Amaratunga, W.I. Milne, *Nature*, **437**, 968(2005)
- <sup>41</sup>C. Niu, E. K. Sichel, R. Hoch, D. Moy, H. Tennent, *Appl. Phys. Lett.*, **70**, 1480(1997)
- <sup>42</sup>Z. Yao, H. W.C. Postma, L. Balents, C. Dekker, *Nature*, **402**, 273(1996)
- <sup>43</sup>J. Kong, N. R. Franklin, C. W. Zhou, M. G. Chapline, S. Peng, *Science*, **287**, 622(2000)
- <sup>44</sup>N. Grobert, M. Terrones, P. H. Redlich, H. Terrones, R. Escudero, *Appl. Phys. Lett.*, **75**, 3363(1999)
- <sup>45</sup>T. Kuzumaki, K. Miyazawa, H. Ichinose, K. Ito, *J. Mater. Res.*, **13**, 2445(1998)
- <sup>46</sup>H. Dai, E. W. Wong, Y. Z. Lu, S. Fan, C. M. Lieber, *Nature*, **375**, 769(1995)
- <sup>47</sup>Y. Huang, X. Duan, Q. Wei, C. M. Lieber, *Science*, **291**, 630(2001)
- <sup>48</sup>R. S. Wagner, W. C. Ellis, *Appl. Phys. Lett.*, **4**, 89(1964)
- <sup>49</sup>J. E. Allen, E. R. Hemesath, D. E. Perea, J. L. Lensch-Falk, Z.Y. Li, F. Yin, M. H. Gass, P. Wang, A. L. Bleloch, R. E. Palmer, L. J. Lauhon, *Nature Nanotech.*, **3**, 168(2008)
- <sup>50</sup>A. M. Morales, C. M. Lieber, *Science*, **279**, 208(1998)
- <sup>51</sup>J. L. Liu, S. J. Cai, G. L. Jin, S. G. Thomas and K. L. Wang, *J. Cryst. Growth*, **200**, 106(1999)
- <sup>52</sup>K. Haraguchi, T. Katsuyama, K. Hiruma, K. Ogawa, *Appl. Phys. Lett.* **60**, 745(1992)
- <sup>53</sup>X. Duan, C. M. Lieber, *Adv. Mater.*, **12**, 298(2000)
- <sup>54</sup>Y. Cui, Z. H. Zhong, D. L. Wang, W. U. Wang, C. M. Lieber, *Nano Lett.*, **3**, 149(2003)
- <sup>55</sup>G. F. Zheng, W. Lu, S. Jin, C. M. Lieber, *Adv. Mater.*, **16**, 1890(2004)
- <sup>56</sup>J. Xiang, W. Lu, Y. J. Hu, Y. Wu, H. Yan, C. M. Lieber, *Nature*, **441**, 489(2006)
- <sup>57</sup>Y. Cui, Q. Q. Wei, H. K. Park, C. M. Lieber, *Science*, **293**, 1289(2001)

- <sup>58</sup>M. C. McAlpine, H. Ahmad, D. W. Wang, J. R. Heath, *Nat. Mater.*, **6**, 379(2007)
- <sup>59</sup>M. S. Gudixsen, L. J. Lauhon, J. Wang, D. C. Smith, C. M. Lieber, *Nature*, **415**, 617(2002)
- <sup>60</sup>Y. Huang, X. F. Duan, Y. Cui, C. M. Lieber, *Nano Lett.*, **2**, 101(2002)
- <sup>61</sup>X. F. Duan, Y. Huang, R. Agarwal, C. M. Lieber, *Nature*, **421**, 241(2003)
- <sup>62</sup>Y. Huang, X. F. Duan, C. M. Lieber, *Small*, **1**, 142(2005)
- <sup>63</sup>M. Terrones *et al*, *Nature*, **388**, 52(1997)
- <sup>64</sup>J. Kong, H. T. Soh, A. Cassell, C. F. Quate, H. Dai, *Nature*, **395**, 878(1998)
- <sup>65</sup>A. M. Cassell, N. R. Franklin, T. W. Tomblor, E. M. Chan, J. Han, H. Dai, *J. Am.Chem. Soc.*, **121**, 7975(1999)
- <sup>66</sup>B. Q. Wei, R. Vajtai, Z. J. Zhang, G. Ramanath, P. M. Ajayan, *J. Nanosci. Nanotech.*, **1**, 35(2001)
- <sup>67</sup>M. Burghard, G. Duesberg, G. Philipp, J. Muster, S. Roth, *Adv. Mater.*, **10**, 584(1998)
- <sup>68</sup>K. H. Choi, J. P. Bourgoïn, S. Auvray, D. Esteve , G. S. Duesberg, S. Roth , M. Burghard, *Surface Science*, **462**, 195(2000)
- <sup>69</sup>M. C. LeMieux, M. Roberts, S. Barman, Y. W. Jin, J. M. Kim, Z. Bao, *Science*, **321**, 101(2008)
- <sup>70</sup>E. Joselevich, C. M. Lieber, *Nano. Lett.*, **2**, 1137(2002)
- <sup>71</sup>Y. Zhang, A. Chang, J. Cao, Q. Wang, W. Kim, Y. Li, N. Morris, E. Yenilmez, J. Kong, H. Dai, *Appl. Phys. Lett.*, **79**, 3155(2001)
- <sup>72</sup>S. Huang, M. Woodson, R. Smalley, J. Liu, *Nano Lett.*, **4**, 1025(2004)
- <sup>73</sup>M. D. Lay, J. P. Novak, E. S. Snow, *Nano letters*, **4**, 603(2004)
- <sup>74</sup>H. Shimoda, S. J. Oh, H. Z. Geng, R. J. Walker, X. B Zhang, L. E. McNeil, O. Zhou, *Adv. Mater.*, **14**, 899(2002)
- <sup>75</sup>X. Li, L. Zhang, X. Wang, I. Shimoyama, X. Sun, W. S. Seo, H. Dai, *J. Am. Chem. Soc.*, **129**, 4890(2007)
- <sup>76</sup>M. Su, Y. Li, B. Maynor, A. Buldum, J. P. Lu, J. Liu, *J. Phys. Chem. B.*, **104**, 6505(2000)
- <sup>77</sup>A. Ismach, L. Segev, E. Wachtel, E. Joselevich, *Angew. Chem., Int.Ed.*, **43**, 6140(2004)
- <sup>78</sup>S. Han, X. Liu, C. Zhou, *J. Am. Chem. Soc.*, **127**, 5294(2005)
- <sup>79</sup>S. J. Kang, C. Kocabas, T. Ozel, M. Shim, N. Pimparkar, M. A. Alam, S. V. Rotkin, J. A. Rogers, *Nature Nanotech.*, **2**, 230(2007)
- <sup>80</sup>P. C. Collins, M. S. Arnold, P. Avouris, *Science*, **292**, 706(2001)
- <sup>81</sup>P. A. Smith, C. D. Nordquist, T. N. Jackson, T. S. Mayer, B. R. Martin, J. Mbindyo, T. E. Mallouk, *Appl. Phys. Lett.*, **77**, 1399(2000)
- <sup>82</sup>X. Duan, Y. Huang, Y. Cui, J. Wang, C. M. Lieber, *Nature*, **409**, 66(2001)

- 
- <sup>83</sup>B. Messer, J. Song, P. Yang, *J. Am. Chem. Soc.*, **122**, 10232(2000)
- <sup>84</sup>Y. Huang, X. Duan, Q. Wei, C. M. Lieber, *Science*, **291**, 630(2001)
- <sup>85</sup>D. Whang, S. Jin, Y. Wu, C. M. Lieber, *Nano Lett.*, **3**, 1255(2003)
- <sup>86</sup>F. Kim, S. Kwan, J. Akana, P. Yang, *J. Am. Chem. Soc.*, **123**, 4360(2001)
- <sup>87</sup>A. Tao, F. Kim, C. Hess, J. Goldberger, R. He, Y. Sun, Y. Xia, P. Yang, *Nano Lett.*, **3**, 1229(2003)
- <sup>88</sup>R. Agarwal, K. Ladavac, Y. Roichman, G. Yu, C. Lieber, D. Grier, *Opt. Express*, **13**, 8906(2005)
- <sup>89</sup>D. Wang, Y. L. Chang, Q. Wang, J. Cao, D. B. Farmer, R. G. Gordon, H. Dai, *J. Am. Chem. Soc.*, **126**, 11602(2004)
- <sup>90</sup>M. S. Islam, S. Sharma, T. I. Kamins, R. S. Williams, *Nanotechnology*, **15**, L5(2004)
- <sup>91</sup>Y. Shan, S. J. Fonash, *ACS Nano*, **2**, 429(2008)
- <sup>92</sup>S. M. Koo, M. D. Edelstein, Q. Li, C. A. Richter, E. M. Vogel, *Nanotechnology*, **16**, 1482(2005)
- <sup>93</sup>Z. Li, Y. Chen, X. Li, T. I. Kamins, K. Nauka, R. S. Williams, *Nano Lett.*, **4**, 245(2004)
- <sup>94</sup>A. Colli, A. Fasoli, S. Pisana, V. Fu, P. Beecher, W. I. Milne, A. C. Ferrari, *Nano Lett.*, **8**, 1358(2008)
- <sup>95</sup>E. Stern, *Nature*, **445**, 519(2007)
- <sup>96</sup>A. A. Talin, L. L. Hunter, F. Leonard, B. Rokad, *Appl. Phys. Lett.*, **89**, 153102(2006)
- <sup>97</sup>S. Tans, A. Verschueren, C. Dekker, *Nature*, **393**, 49(1998)
- <sup>98</sup>Y. Huang, X. Duan, Y. Cui, L. Lauhon, K. Kim, C.M. Lieber, *Science*, **294**, 1313(2001)
- <sup>99</sup>A. Bachtold, P. Hadley, T. Nakanishi, C. Dekker, *Science*, **294**, 1317(2001)
- <sup>100</sup>Z. Chen, J. Appenzeller, Y. M. Lin, J. S. Oakley, A. G. Rinzler, J. Tang, S. J. Wind, P. M. Solomon, P. Avouris, *Science*, **311**, 1735(2006)
- <sup>101</sup>R. S. Friedman, M. C. McAlpine, D. S. Ricketts, D. Ham, C. M. Lieber, *Nature*, **434**, 1085(2005)
- <sup>102</sup>J. Tonnuci, B. L. Justus, A. J. Campillo, C. E. Ford, *Science*, **258**, 783(1992)
- <sup>103</sup>T. W. Whitney, J. S. Jiang, P. C. Searson, C. L. Chien, *Science*, **261**,1316(1993)
- <sup>104</sup>F. Keller, M. S. Hunter, D. L. Robinson, *J. Electrochem. Soc.*, **100**,411(1953)
- <sup>105</sup>G. E. Thompson, R. C. Furnsax, G. C. Wood, J. A. Richardson, J. S. Gode, *Nature*, **272**,433(1978)
- <sup>106</sup>H. Masuda, K. Fukuda, *Science*, **268**, 1466(1995)
- <sup>107</sup>J. Li, C. Papadopoulos, J. M. Xu, M. Moskovits, *Appl. Phys.Lett.*, **75**, 367(1999)
- <sup>108</sup>S. H Jeong, O. J. Lee, K. H. Lee, *Chem. Mater.*,**14**, 1859(2002)
- <sup>109</sup>K. K. Lew, C. Reuther, A. H. Carim, J. M. Redwing, *J. Vac. Sci. Technol. B.*, **20**, 389(2002)
- <sup>110</sup>G. D.Bengough , J. M. Stuart, UK patent **23**(1923)
- <sup>111</sup>British Patent 290,901, C. H. Gower , R. Stafford, O'Brien and Partners; (1927)

- 
- <sup>112</sup>A. Brace: "Anodizing - It's Development, Status and Future Challenges", *Metal Finishing*, **100**, 59 (2002)
- <sup>113</sup>J. D. Edwards, E. Keller, *Trans. Electrochem. Soc.*, **79**, 135(1941)
- <sup>114</sup>J. P. O'Sullivan and G. C. Wood, *Proc. Roy. Soc. Lond. A*, **317**, 511(1970)
- <sup>115</sup>G. E. Thompson, Y. Xu, P. Skeldon, K. Shimizu, S. H. Han, G. C. Wood, *Philosophical Magazine B*, **55**, 651(1987)
- <sup>116</sup>K. Shimizu, K. Kobayashi, G. E. Thompson, G. C. Wood, *Phil. Mag.*, **66**, 643(1992)
- <sup>117</sup>M. Moskovits, J. M. Xu, US Patent number **5, 581,091**(1996)
- <sup>118</sup>D. Routkevitch, A. A. Tager, J. Haruyama, D. Almawlawi, M. Moskovits, J. M. Xu, *IEEE Transactions On Electron Devices*, **43**, 10 (1996)
- <sup>119</sup>J. W. Diggle, T. C. Downie, C. W. Goulding, *Chem. Rev.*, **69**, 365(1969)
- <sup>120</sup>S. Tajima, *Electrochim Acta*, **22**, 995(1977)
- <sup>121</sup>V. P. Parkhutik, V. I. Shershulsky, *J. Phys. D: Appl. Phys.*, **25**, 1258(1992)
- <sup>122</sup>D. A. Vermilyea, *J. Electrochem. Soc.*, **110**, 345(1963)
- <sup>123</sup>D. H. Bradhurst, J. S. L. Leach, *J. Electrochem. Soc.*, **113**, 1245(1966)
- <sup>124</sup>J. C. Nelson, R. A. Oriani, *Corrosion Sci.*, **34**, 307(1993)
- <sup>125</sup>J. D. Kim, S. I. Pyun, R. A. Oriani, *Electrochim. Acta.*, **40**, 1171(1995)
- <sup>126</sup>S. M. Moon, S. I. Pyun, *J. Electrochim. Acta.*, **43**, 3117(1998)
- <sup>127</sup>K. Nielsch, J. Choi, K. Schwirn, R. B. Wehrspohn, U. Gösele, *Nano Letters*, **2**, 677(2002)
- <sup>128</sup>A. P. Li, F. Muller, A. Birner, K. Nielsch, U. Gösele, *J. Appl. Phys.*, **84**, 6023(1998)
- <sup>129</sup>H. Masuda, H. Yamada, M. Satoh, H. Asoh, *Appl. Phys. Lett.*, **71**, 270(1997)
- <sup>130</sup>H. Masuda, F. Hasagawa, S. Ono, *J. Electrochem. Soc.*, **144**, L127(1997)
- <sup>131</sup>G. E. Thompson, Y. Xu, P. Skeldon, K. Shimizu, S. H. Han, G. C. Wood, *Phil. Mag. B*, **55**, 651(1987)
- <sup>132</sup>G. C. Wood, P. Skeldon, G. E. Thompson, K. Shimizu, *J. Electrochem. Soc.*, **143**, 74(1996)
- <sup>133</sup>K. Shimizu, K. Kobayashi, G. E. Thompson, G. C. Wood, *Phil. Mag. B*, **64**, 345(1991)
- <sup>134</sup>T. P. Hoar, N. F. Mott, *J. Phys. Chem. Solids.*, **9**, 97(1959)
- <sup>135</sup>V. P. Parkhutik, V. I. Shershulsky, *J. Phys. D: Appl. Phys.*, **25**, 1258(1992)
- <sup>136</sup>S. K. Thamida, H. C. Chang, *chaos*, **12**, 240(2002)
- <sup>137</sup>V. P. Parkhutik, *Corros. Sci.*, **26**, 295(1986)
- <sup>138</sup>V. P. Parkhutik, V. I. Shershulskii, *J. Phys. D: Appl. Phys.*, **19**, 623(1986)
- <sup>139</sup>O. Jessensky, F. Muller, U. Gosele, *Appl. Phys. Lett.*, **72**, 1173(1998)
- <sup>140</sup>S. Ono, M. Saito, M. Ishiguro, H. Asoh, *J. Electrochem. Soc.*, **151**, B473(2004)

- 
- <sup>141</sup>D. H. Bradhurst, J. S. L. Leach, *J. Electrochem. Soc.*, **113**, 1245(1966)
- <sup>142</sup>J. H. F. Lim, X. Jia, R. Jafferli, G. A. Davies, *Sep.Sci.Technology.*, **28**, 821(1993)
- <sup>143</sup>ANOPORE membranes is a trademark of Whatman International
- <sup>144</sup>J. Randon, P. P. Mardilovich, A. N. Govyadinov, R. Paterson, *J. Colloid. interf. Sci.*, **169**, 335(1995)
- <sup>145</sup>M. Konno, M. Shino, S. Sugawara, S. Saito, *J. Membr .Sci.*, **37**, 193(1988)
- <sup>146</sup>F. Li, L. Zhang, R. M. Metzger, *Chem. Mater.*, **10**, 2470(1998)
- <sup>147</sup>O. Jessensky, F. Muller, U.Gösele, *J. Electrochem. Soc.*, **145**, 3735(1998)
- <sup>148</sup>R. B. Wehrspohn, F. Ozanam, J. N. Chazalviel, *J. Electrochem. Soc.*,**145**, 2958(1998)
- <sup>149</sup>V. P. Parkhutik, V. I. Shershulsky, *J. Phys. D: Appl .Phys.*, **25**, 1258(1992)
- <sup>150</sup>T. Pavlovic, A. Ignatiev, *Thin solid Films*, **138**, 97(1986)
- <sup>151</sup>G. E. Thompson, G. C. Wood, *Nature*, **290**, 230(1981)
- <sup>152</sup>S. Ono, M. Saito, H. Asoh, *Electrochimica Acta*, **51**, 827(2005)
- <sup>153</sup>S. K. Hwang, S. H. Jeong, H. Y. Hwang, O. J. Lee, K. H. Lee, *Korean J. Chem. Eng.*, **19**, 467(2002)
- <sup>154</sup>Z. Fan, J. C. Ho, Z. A. Jacobson, R. Yerushalmi, R. L. Alley, H. Razavi, A. Javey, *Nano Lett.*, **8**, 20(2008)
- <sup>155</sup>H. Masuda, K. Nishio, N. Baba, *Appl. Phys. Lett.*, **63**, 3155(1993)
- <sup>156</sup>C. S. Cojocaru, J. M. Padovani, T. Wade, C. Mandoli, G. Jaskierowicz, J. E. Wegrove, A. F. Morral, D. Pribat, *Nano Lett.*, **4**, 675(2005)
- <sup>157</sup>H. G. Zhang, Z. Chen, T. Li, K. Saito, *J. Nanosci. Nanotech.*, **5**, 1745(2005)
- <sup>158</sup>X. Zhao *et al*, *J. Electrochem. Soc.*, **152**, B411(2005)
- <sup>159</sup>D. Pribat, C. S. Cojocaru, J. M. Padovani, T.Wade , C. Mandoli, G. Jaskierowicz, A. F. Morral, J. E. Wegrove, *Proceedings of SPIE Quantum Sensing and Nanophotonic Devices II.* **5732**, 58(2005)
- <sup>160</sup>R. Vidal, A. C. West, *J. Electrochem.Soc.*, **142**, 2682(1995)
- <sup>161</sup>D. Crouse, Y. H. Lo, A. E. Miller, M. Crouse, *Appl. Phys. Lett.*, **76**, 49(2000)
- <sup>162</sup>H. Masuda, K. Fukuda, *Science*, **268**, 1466(1995)
- <sup>163</sup>O. Jessensky, F. Muller, U. Gösele, *Appl. Phys. Lett.*, **72**, 9(1998)
- <sup>164</sup>K. Nielsch, J. Choi, K. Schwirn, R. B. Wehrspohn, U. Gösele, *Nano Letters*, **2**, 677(2002)
- <sup>165</sup>K. Schwirn, W. Lee, R. Hillebrand, M. Steinhart, K. Nielsch, U. Gösele, *ACS Nano*, **2**, 302(2008)
- <sup>166</sup>W. Lee, R. Ji, U. Gösele, K. Nielsch, *Nat. Mater.*, **5**, 741(2006)
- <sup>167</sup>W.Chen, J. S. Wu, X. H. Xia, *ACS Nano*, **2**, 959(2008)
- <sup>168</sup>M. Gowtham, L. Eude, C .S. Cojocaru, B. Marquardt, H. J. Jeong, P. Legagneux, K. K. Song, D. Pribat, *Nanotechnology*, **19**, 035303(2008)

- <sup>169</sup>L. S. Van Dyke, C. R. Martin, *Langmuir*, **6**, 1123(1990)
- <sup>170</sup>W. Liang, C. R. Martin, *J. Am. Chem. Soc.*, **112**, 9666(1990)
- <sup>171</sup>C. J. Brumlik, C. R. Martin, *J. Am. Chem. Soc.*, **113**, 3174(1991)
- <sup>172</sup>C. J. Brumlik, C. R. Martin, K. Tokuda, *Anal. Chem.*, **64**, 1201(1992)
- <sup>173</sup>J. D. Klein, R. D. I. Herrick, D. Palmer, M. J. Sailor, C. J. Brumlik, C. R. Martin. *Chem. Mater.*, **5**, 902(1993)
- <sup>174</sup>T. Kyotani, L. Tsai, A. Tomita, *Chem. Mater.*, **7**, 1427(1995)
- <sup>175</sup>R. V. Parthasarathy, K. L. N. Phani, C. R. Martin, *Adv Mater.*, **7**, 896(1995)
- <sup>176</sup>L. Mengke, W. Chengwei, L. Hulin, *Chinese Science Bulletin*, **46**, 1793(2001)
- <sup>177</sup>K. K. Lew, C. Reuther, A. H. Carim, J. M. Redwing, *J. Vac. Sci. Technol. B.*, **20**, 389(2002)
- <sup>178</sup>T. E. Bogart, S. Dey, K. K. Lew, S. E. Mohny, J. M. Redwing, *Adv Mater.*, **17**, 114(2005)
- <sup>179</sup>T. Shimizu, T. Xie, J. Nishikawa, S. Shingubara, S. Senz, U. Gösele, *Adv. Mater.*, **19**, 917(2007)
- <sup>180</sup>T. Shimizu, S. Senz, S. Shingubara, U. Gösele, *Appl. Phys. A.*, **87**, 607(2007)
- <sup>181</sup>T. Davida, D. Buttarda, M. D. Hertogc, P. Gentilea, T. Barond, P. Ferrete, J, L, Rouvièrec, *Superlattices and Microstructures*, **44**, 354(2008)
- <sup>182</sup>K. Bladh, L. K. L. Falk, F. Rohmund, *Appl. Phys. A: Mater. Sci. Process.*, **70**, 317(2000)
- <sup>183</sup>Y. Saito, *Carbon*, **33**, 979(1995)
- <sup>184</sup>R. T. K. Baker, M. A. Barber, P. S. Harris, F. S. Feates, R. J. Waite, *J. Catal.*, **26**, 51(1972)
- <sup>185</sup>J. Gavillet, A. Loiseau, C. Journet, F. Willaime, F. Ducastelle, J. C. Charlier, *Phys. Rev. Lett.*, **87**, 275504(2001)
- <sup>186</sup>D. Takagi, Y. Homma, H. Hibino, S. Suzuki, Y. Kobayashi, *Nano Lett.*, **6**, 2642(2006)
- <sup>187</sup>S. Bhaviripudi, E. Mile, S.A. Steiner, A. T. Zare, M. S. Dresselhaus, A. M. Belcher, J. Kong, *J. Am. Chem. Soc.*, **129**, 1516(2007)
- <sup>188</sup>W. W. Zhou, Z. Y. Han, J. Y. Wang, Y. Zhang, Z. Jin, X. Sun, Y. W. Zhang, C. H. Yan, Y. Li, *Nano Lett.*, **6**, 2987(2006)
- <sup>189</sup>D. Takagi, H. Hibino, S. Suzuki, Y. Kobayashi, Y. Homma, *Nano Lett.*, **7**, 2272(2007)
- <sup>190</sup>H. Dai, A. G. Rinzler, P. Nikolaev, A. Thess, D. T. Colbert, R. E. Smalley, *Chem. Phys. Lett.*, **260**, 471(1996)
- <sup>191</sup>C. L. Cheung, A. Kurtz, H. Park, C. M. Lieber, *J. Phys. Chem. B.*, **106**, 2429(2002)
- <sup>192</sup>Y. Li, W. Kim, Y. Zhang, M. Rolandi, D. Wang, H. Dai, *J. Phys. Chem. B.*, **105**, 11424(2001)
- <sup>193</sup>W. E. Alvarez, B. Kitiyanan, A. Borgna, D. E. Resasco, *Carbon*, **39**, 547(2001)

- <sup>194</sup>C. Emmenegger, J. M. Bonard, P. Mauron, P. Sudan, A. Lepora, B. Grobety, A. Zittel, L. Schlapbach, *Carbon*, **41**, 539(2003)
- <sup>195</sup>F. Ding, P. Larsson, J. A. Larsson, R. Ahuja, H. Duan, A. Rosén, K. Bolton, *Nano Lett.*, **8**, 463(2008)
- <sup>196</sup>P. Larsson, J. A. Larsson, R. Ahuja, F. Ding, B. I. Yakobson, H. Duan, A. Rosén, K. Bolton, *Physical Review B*, **75**, 115419(2007)
- <sup>197</sup>E. I. Givargizov, *J. Crystal Growth*, **31**, 20(1975)
- <sup>198</sup>G. A. Bootsma, H. J. Gassen, *J. Crystal Growth*, **10**, 223(1971)
- <sup>199</sup>C. Qi, R. G. Oncher, R. Solanki, J. Jordan, *Nanotechnology*, **18**, 075302(2007)
- <sup>200</sup>X. H. Sun, C. Didychuk, T. K. Sham, N. B. Wong, *Nanotechnology*, **17**, 2925(2006)
- <sup>201</sup>J. Johansson, L. S. Karlsson, C. P. T. Svensson, T. Martensson, B. A. Wacaser, K. Deppert, L. Samuelson, W. Seifert, *Nature Materials*, **5**, 574(2006)
- <sup>202</sup>Z. Y. Tang, N. A. Kotov, M. Giersig, *Science*, **297**, 237(2002)
- <sup>203</sup>M. K. Sunkara, S. Sharma, R. Miranda, G. Lian, E. C. Dickey, *Appl. Phys. Lett.*, **79**, 1546(2001)
- <sup>204</sup>B. Kalache, P. Roca i Cabarrocas, A. Fontcuberta i Morral, *J. J. Appl. Phys.*, **45**, L190(2006)
- <sup>205</sup>Y. Wang, V. Schmidt, S. Senz, U. Gosele, *Nature Nanotechnology*, **1**, 186(2006)
- <sup>206</sup>T. I. Kamins, R. S. Williams, D. P. Basile, T. Hesjedal, J. S. Harris, *J. Appl. Phys.*, **89**, 1008(2001)
- <sup>207</sup>P. J. Alet, L. Yu, G. Patriarche, S. Palacina, P. R. Cabarrocas, *J. Mater. Chem.*, **18**, 5187(2008)
- <sup>208</sup>D. W. Foster, A. J. Learn, T. I. Kamins, *J. Vac. Sci. Technol. B*, **4**, 1182(1986)
- <sup>209</sup>H. L. Duan, G. A. Zaharias, S. F. Bent, *Mat. Res. Soc. Symp. Proc.*, **715**, 21(2002)
- <sup>210</sup>J. Liang, H. Chik, J. Xu, *IEEE Journal Of Selected Topics In Quantum Electronics*, **8**, 998(2002)
- <sup>211</sup>J. Liang, H. Chik, A. Yin, J. M. Xu, *J. Appl. Phys.*, **91**, 2544(2002)
- <sup>212</sup>J. Li, C. Papadopoulos, J. M. Xu, *Nature*, **402**, 253(1999)
- <sup>213</sup>A. J. Yin, J. Li, W. Jian, A. J. Bennett, J. M. Xu, *Appl. Phys. Lett.*, **79**, 1039(2001)
- <sup>214</sup>W. Hu, D. Gong, Z. Chen, L. Yuan, K. Saito, C. A. Grimes, P. Kichambare, *Appl. Phys. Lett.*, **79**, 3083(2001)
- <sup>215</sup>S. Shingubara, O. Okino, Y. Murakami, H. Sakaue, T. Takahagi, *J. Vac. Sci. Technol. B.*, **19**, 1901(2001)
- <sup>216</sup>P. Hoyer, K. Nishio, H. Masuda, *Thin Solid Films*, **286**, 88(1996)
- <sup>217</sup>Y. Kanamori, K. Hane, H. Sai, H. Yugami, *Appl. Phys. Lett.*, **78**, 142(2001)
- <sup>218</sup>D. N. Davydov, P. A. Sattari, D. AlMawlawi, A. Osika, T. L. Haslett, *J. Appl. Phys.*, **86**, 3983(1999)
- <sup>219</sup>Y. C. Sui, D. R. Acosta, J. A. Gonzalez-Leon, A. Bermudez, J. Feuchtwanger, B. Z. Cui, J. O. Flores, J. M. Saniger, *J. Phys. Chem. B.*, **105**, 1523(2001)

- <sup>220</sup>J. S. Suh, J. S. Lee, H. Kim, *Synthetic Metals*, **123**, 381(2001)
- <sup>221</sup>S. Shingubara, O. Okino, Y. Sayama, H. Sakaue, T. Takahagi, *Solid-State Electron.*, **43**, 1143(1999)
- <sup>222</sup>C. R. Martin, *Science*, **266**, 1961(1994)
- <sup>223</sup>K. Nielsch, F. Müller, A. P. Li, U. Gösele, *Adv. Mat.*, **12**, 582(2000)
- <sup>224</sup>N. J. Gerein, J. A. Haber, *J. Phys. Chem. B.*, **109**, 17372(2005)
- <sup>225</sup>J. Choi, G. Sauer, K. Nielsch, R. B. Wherspohn, U. Gösele, *Chem. Mater.*, **15**, 776(2003)
- <sup>226</sup>M. S. Sander, A. L. Prieto, R. Gronsky, T. Sands, A. M. Stacy, *Adv. Mater.*, **14**, 665(2002)
- <sup>227</sup>A. D. Franklin, M. R. Maschmann, M. DaSilva, D. B. Janes, T. S. Fisher, T. D. Sands, *J. Vac. Sci. Technol. B.*, **25**, 343(2007)
- <sup>228</sup>J. Oh, C. V. Thompson, *Adv. Mater.*, **20**, 1368(2008)
- <sup>229</sup>B. Marquardt, L. Eude, M. Gowtham, G. S. Cho, H. J. Jeong, M. Châtelet, C. S. Cojocar, B. S. Kim, D. Pribat, *Nanotechnology*, **19**, 405607(2008)
- <sup>230</sup>G. E. Thompson, R. C. Furneaux, G. C. Wood, *Corros. Sci.*, **18**, 481(1978)
- <sup>231</sup>D. Hönicke, *Appl. Catal.*, **5**, 179(1983)
- <sup>232</sup>D. Hönicke, *Appl. Catal.*, **5**, 199(1983)
- <sup>233</sup>Y. C. Sui, D. R. Acosta, J. A. Gonzalez-Leon, A. Bermudez, J. Feuchtwanger, B. Z. Cui, *J. Phys. Chem. B.*, **105**, 1523(2001)
- <sup>234</sup>J. S. Lee, G. H. Gu, H. Kim, K. S. Jeong, J. Bae, J. S. Suh, *Chem. Mater.*, **13**, 2387(2001)
- <sup>235</sup>A. I. La Cava, C. A. Bernardo, D. L. Trimm, *Carbon*, **20**, 219(1982)
- <sup>236</sup>H. N. Wanka, M. B. Schubert, *J. Phys. D: Appl. Phys.*, **30**, L28(1997)
- <sup>237</sup>K. Hata, D. N. Futaba, K. Mizuno, T. Namai, M. Yumura, S. Iijima, *Science*, **306**, 1362(2004)
- <sup>238</sup>C. S. Cojocar, S. H. Lim, A. J. Guilley, N. L. Sech, S. Xavier, P. Legagneux, D. Pribat, *unpublished*
- <sup>239</sup>R. E. Smalley, Y. Li, V. C. Moore, K. Price, R. Colorado, H. K. Schmidt, R. H. Hauge, A. R. Barron, J. M. Tour, *J. Am. Chem. Soc.*, **128**, 15824(2006)
- <sup>240</sup>T. Yamada, T. Namai, K. Hata, D. N. Futaba, K. Mizuno, J. Fan, M. Yudasaka, M. Yumura, S. Iijima, *Nature Nanotech.*, **1**, 131(2006)
- <sup>241</sup>W. L. Massover, *Micron*, **24**, 389(1993)
- <sup>242</sup>P. M. Harrison, S. C. Andrews, P. J. Artymiuk, G. C. Ford, J. R. Guest, J. Hirzmann, D. M. Lawson, J. C. Livingstone, J. M. A. Smith, A. Treffry, S. J. Yewdall, *Advances in Inorg. Chem.*, **36**, 449(1991)
- <sup>243</sup>F. C. Meldrum, V. J. Wade, D. L. Nimmo, B. R. Heywood, S. Mann, *Nature*, **349**, 684(1991)
- <sup>244</sup>F. C. Meldrum, B. R. Heywood, S. Mann, *Science*, **257**, 522(1992)
- <sup>245</sup>T. Douglas, V. T. Stark, *Inorg. Chem.*, **39**, 1828(2000)

<sup>246</sup>I. Yamashita, J. Hayashi, M. Hara, *Chem. Lett.*, **33**, 1158(2004)

<sup>247</sup>Y. Li, W. Kim, Y. Zhang, M. Rolandi, D. Wang, H. Dai, *J. Phys. Chem. B.*, **105**, 11424(2001)